ANKARA YILDIRIM BEYAZIT UNIVERSITY

GRADUATE SCHOOL OF NATURAL AND APPLIED SCIENCES

DESIGN AND ANALYSIS OF A NEW VARIABLE INCIDENCE WING AND RUDDERVATOR MECHANISMS FOR UAVs

M.Sc. Thesis by

MUSTAFA MURAT

Department of Mechanical Engineering

January, 2022

ANKARA

DESIGN AND ANALYSIS OF A NEW VARIABLE INCIDENCE WING AND RUDDERVATOR MECHANISMS FOR UAVs

A Thesis Submitted to
the Graduate School of Natural and Applied Sciences of
Ankara Yıldırım Beyazıt University

In Partial Fulfilment of the Requirements for the Degree of Master of Science in Mechanical Engineering, Department of Mechanical Engineering

by

Mustafa MURAT

January, 2022

ANKARA

M.Sc THESIS EXAMINATION RESULT FORM

We have read the thesis entitled **"DESIGN AND ANALYSIS OF A NEW VARIABLE INCIDENCE WING AND RUDDERVATOR MECHANISMS FOR UAVs"** completed by **Mustafa MURAT** under supervision of **Prof. Dr. Fahrettin ÖZTÜRK** and we certify that in our opinion it is fully adequate, in scope and in quality, as a thesis for the degree of Master of Science.

Prof. Dr. Fahrettin Öztürk

Supervisor

Prof. Dr. Sadettin Orhan

Jury Member

Prof. Dr. Zafer Evis

Jury Member

Prof. Dr. Sadettin Orhan

Director

Graduate School of Natural and Applied Sciences

ETHICAL DECLARATION

I hereby declare that, in this thesis which has been prepared in accordance with the Thesis Writing Manual of Graduate School of Natural and Applied Sciences,

- All data, information and documents are obtained in the framework of academic and ethical rules,
- All information, documents and assessments are presented in accordance with scientific ethics and morals,
- All the materials that have been utilized are fully cited and referenced,
- No change has been made on the utilized materials,
- All the works presented are original,

and in any contrary case of above statements, I accept to renounce all my legal rights.

Date:19.01.2022 **Signature:**

Name & Surname: Mustafa MURAT

ACKNOWLEDGMENTS

Firstly, I would like to take this opportunity to thank my advisor, Prof. Dr. Fahrettin ÖZTÜRK, for his support, guidance, encouragement, and enthusiasm he showed throughout the project. It has been an honor and a pleasure for me to work with such an outstanding academician.

Secondly, I would like to acknowledge Turkish Aerospace, Inc. and its management for their support and encouragement.

Finally, great thanks to my beloved family, my father, my mother, and my wife for their everlasting support, patience, and prayers. I have always felt them by my side.

2022, 19 January **Mustafa MURAT**

DESIGN AND ANALYSIS OF A NEW VARIABLE INCIDENCE WING AND RUDDERVATOR MECHANISMS FOR UAVs

ABSTRACT

In this MSc thesis, a new wing and ruddervator mechanism is designed for take-off and landing of unmanned aerial vehicles (UAVs) from navy carriers with short or other types of runways. The incidence angle of UAV wings is gradually increased during take-off and landing to allow the wings to generate greater lift. These mechanisms are designed based on a "fail-safe design approach" as they are Category-A class structures of UAVs. Similarly, a variable incidence ruddervator system is designed to shorten the take-off distance of aircraft. To this end, it is aimed to shorten the take-off distance of UAV's by changing its flight mechanics via the use of special wing and ruddervator mechanisms.

In this scope, it is showed that a 1425 kg UAV configuration can take-off within 202 meters without using a catapult system. This result is validated by small scale ground tests. The proposed design is compared both numerically and experimentally. It is seen that the designed structure is applicable to UAVs.

Keywords: Unmanned aerial vehicle, variable incidence, short take-off, short landing, mechanism design.

İHA’LAR İÇİN YENİ BİR DEĞİŞKEN OTURMA AÇILI KANAT VE V KUYRUK MEKANİZMALARININ TASARIMI VE ANALİZİ

ÖZ

Bu yüksek lisans tezinde, kısa pisti veya diğer türlerdeki pistleri olan donanma gemilerinden İnsansız Hava Araçları’nın (İHA'nın) kalkış ve inişi için yeni bir kanat ve dümen mekanizmaları tasarlanmıştır. İHA'nın kanatların geliş açısı, kanatların oluşturduğu kaldırma kuvvetini arttırmak için kalkış ve iniş sırasında kademeli olarak artırılır. Bu mekanizmaların tasarımları, bu mekanizmalar İHA'ların Kategori-A sınıfı yapıları olduğu için “hata-güvenli tasarım anlayışı” içinde gerçekleştirilmektedir. Değişken oturma açılı dümen sistemi de tasarlanmıştır. Özel kanat ve dümen mekanizması tasarımları ile İHA'nın uçuş mekaniği özellikleri değiştirilerek uçağın kalkış mesafesinin kısaltılması amaçlanmaktadır.

Bu doğrultuda 1425 kg’ı geçmeyen bir İHA konfigürasyonu için 202 metreden katapultsuz kalkış yapılabileceği gösterilmiştir. Bu sonuç küçük ölçekli yer testleri ile de doğrulanmıştır. Önerilen yeni tasarım hem sayısal hem de deneysel olarak karşılaştırılmıştır. Tasarlanan yapının İHA’lar için uygulanabilir olduğu görülmüştür.

Anahtar Sözcükler: İnsansız hava aracı; değişken oturma açısı; kısa mesafeden kalkış; kısa mesafede duruş; mekanizma tasarımı.

CONTENTS

NOMENCLATURE

Roman Letter Symbols

L	Lift force, N
D	Drag force, N
Cl	Lift coefficient
Cd	Drag coefficient
Cp	Center of pressure
V	Velocity of incoming air, m/s
S	Projected area of the wing, m^2
V	Velocity of incoming air, m/s
Fs	Friction force, N
N	Acting force on main landing gear , N
c	The distance from the neutral axis to a point, m
I	Moment of inertia, $kg.m^2$
M	Moment, N.m
V	Internal shear force, N
Q	First moment of inertia, $kg.m^2$
t	Thickness, mm

Greek Letter Symbols

ρ	Density of fluid, kg/m^3
μ	Friction coefficient between tire and asphalt

Acronyms

UAV	Unmanned aerial vehicle
CFD	Computational fluid dynamics
FEM	Finite element model
$MALE$	Medium altitude long endurance
AC	Aerodynamic center
NP	Neutral point
CG	Center of gravity

LIST OF TABLES

LIST OF FIGURES

CHAPTER 1

INTRODUCTION

1.1 Importance of UAV's

Unmanned aerial vehicles (UAVs) are having a more significant role in today's modern armies. They have increasingly utilized, especially in the military field [1]. Indeed, UAVs have become the most powerful assets of modern militaries worldwide [2]. In addition to the military, these modern robots are used in various areas, such as in intelligence, city security, search and rescue operations, and fire detection in forests, and the need for them is rapidly increasing [3]. Although used in many different areas, these aircrafts are basically developed for military and intelligence purposes [4]. Armies have given growing attention to these advanced vehicles in the last decades, giving rise the development of new military tactics in the battlefield [5]. Today's battle plans do not disregard UAVs; on the contrary, the entire battle strategy is based on them [6]. There are many reasons for the indispensable of UAVs in the battle field. First, they do not carry pilots inside. Thus, no human life is at risk. This is extremely important because air forces of armies are based on pilots, and training of an air force pilot is both expensive and time-consuming for militaries [7]. Secondly, human life is more important than anything else. Countries do not want to lose their soldiers. They are ready to sacrifice pilotless aircraft for the sake of their countries. Obviously, UAVs will dominate jet fighter inventory of air forces in the future with the addition of artificial intelligence algorithms and the advancement in UAV technologies, which will gradually eliminate the human factor in combats. In addition, unmanned jet fighters are likely to be more dangerous than conventional 5^{th} generation manned jet fighters due to their maneuverability capability. Today jet fighters withstand +9g [8] and -3g loads. This is much different for unmanned jets. The aircraft does not carry human inside, and this changes all the design criteria such as g limits of the aircraft. There is the prospect of designing an unmanned fighter jet that can withstand 50 g

maneuvers and be operated like missiles. Thus, the importance and the role of unmanned aerial vehicles are likely to grow, shaping the future.

As UAV progresses, different necessities emerge. For example, carrier based unmanned aerial vehicles are designed differently. UAVs, which are already powerful robots for armies, are also used as carriers and gaining importance in terms of sea power [9]. X-47B which is presented in Figure 1.1 whose first flight operation was conducted on 4 February 2011 [11], is a good example of carrier based unmanned aerial vehicles that possess autonomous aerial refueling capability [10]. It has been used operationally for decades and is still undergoing a development process.

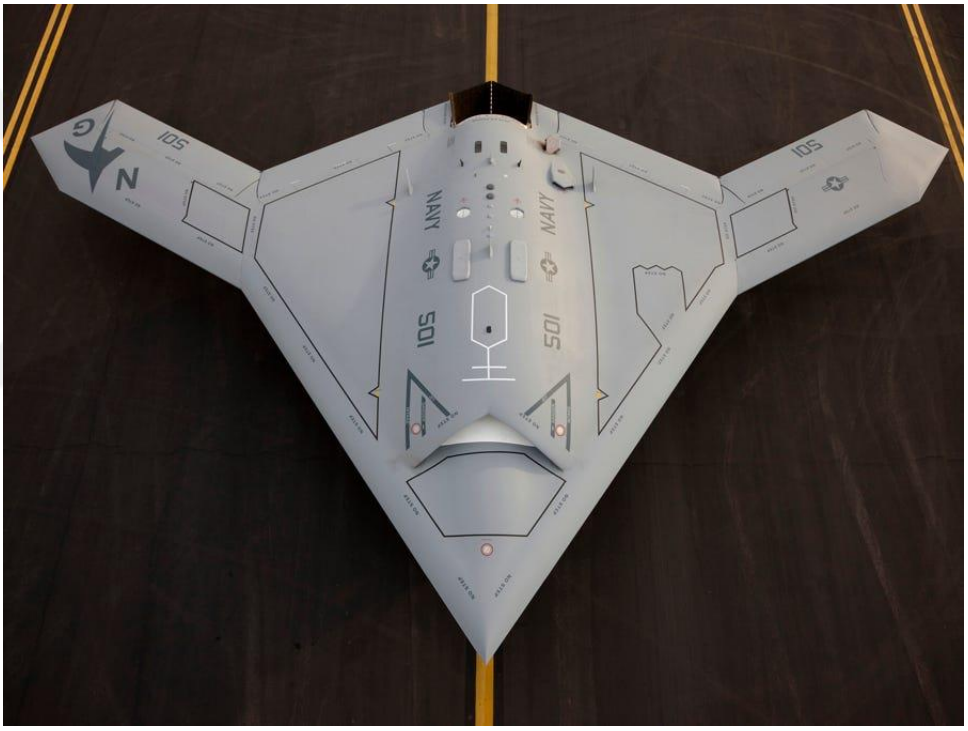

Figure 1.1 X-47B UAV [11]

UAVs having great advantages, Turkey aims to put TCG Anadolu amphibious assault ship into service in 2021 [12] and use it as UAV based carrier in the future [13] although, for the time being, it does not have catapult technology that allows aircrafts to gain speed in a short time. This necessitates basing either small UAVs or vertical take of UAVs into TCG Anadolu which makes this huge platform inefficient.

Figure 1.2 TCG Anadolu amphibious assault ship [12]

However, if a MALE class UAV with long endurance and high external payload capacity is located in TCG Anadolu which is presented in Figure 1.2 (such as ANKA MALE UAV which is showed in Figure 1.3), it will remarkably improve the effectiveness of this carrier. To base a MALE class UAV into TCG Anadolu, the UAV take-off within 230 meters runway [14] without catapult technology should be made possible.

Figure 1.3 ANKA MALE class UAV

Accordingly, this thesis proposes a unique design solution for take-off within short runway without using the catapult system. As a matter of fact, a wing mechanism that can increase and decrease incidence angle of the entire wing system is designed, one that could be used in any time-of-flight envelope. This mechanism is capable of increasing the angle of attack of wing without increasing the fuselage during take-off and landing. Consequently, lift coefficient (Cl) of wing is increased so that the UAV could be lifted off in a short runway. Aircraft's static stability is changing when the generated lift of the aircraft is increased by changing the angle of attack of the wing because the neutral point of aircraft gets closer to the aerodynamic center as the generated lift increases and the neutral point position gets far from the aerodynamic center. To keep the static stability of aircraft, it is essential to keep the position of neutral point which could satisfy the increase of the angle of attack of ruddervator mechanisms as the angle of attack of wing increases. Therefore, the present study has designed a unique fail-safe rotating mechanism for ruddervators also. To clarify the main features of the mechanism, some basic aerodynamic and flight mechanics terms are explained in the following section.

CHAPTER 2

SOME BASIC CONSEPTS OF AERODYNAMICS AND FLIGHT MECHANICS

2.1 Center of Pressure

Incoming air generates pressure on the wing of the aircraft. Pressurized aircraft wing produces forces of lift and drag on entire surface of the aircraft wing [15]. Here center of pressure is an imaginary point that the resultant net force on the wing is acting on [16].

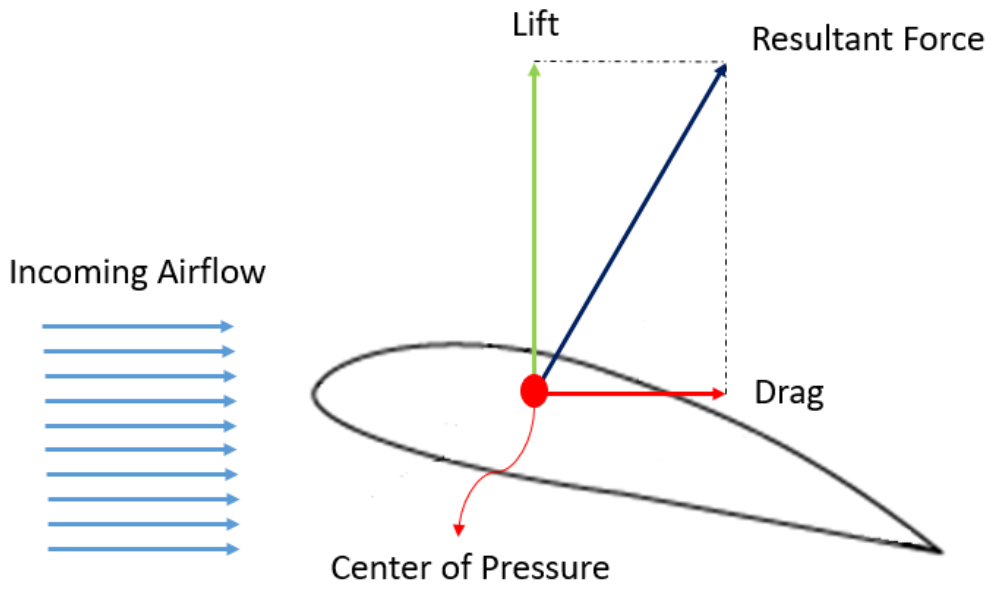

Figure 2.1 Center of pressure

Total lift produced and drag forces and location of the center of pressure change while the angle of attack of the wing changes. Center of pressure which is presented in Figure 2.1 (Cp) is no longer used in flight mechanics equations because the location of the center of pressure always changes as the angle of attack changes. If the center of

pressure is used in flight mechanics equations, the location of the center of pressure needs to be changed for all different angles of attack, which is implausible and time consuming. Instead of the center of pressure, which changes with the angle of attack of the aircraft, “Aerodynamic Center” is used in this study. The location of aerodynamic center does not change as the angle of attack of the wing changes.

2.2 Aerodynamic Center

As the angle of attack of a wing changes, the center of pressure location of the wing changes. For every wing, there is a special point where the total acting moment of acting resultant force is equal for all different angle of attacks. This point is called Aerodynamic Center (AC) of the wing [17]. As it is seen in Figure 2.2, as the angle of attack increases, the Cp location goes towards the leading edge of the wing while the total lift increases. While the angle of attack decreases, the Cp location goes towards the trailing edge side of the wing as the total lift decreases. This phenomenon allows the calculation of a special point where the total acting moment induced by the lift is equal. Instead of showing the acting lift in center of pressure, produced the lift and constant moment could be used in the AC, which is more logical because there is no need to change the location of aerodynamic center as the angle of attack of the aircraft changes.

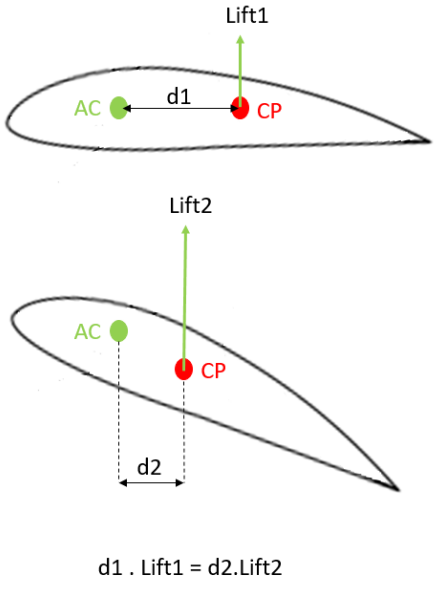

Figure 2.2 Aerodynamic center

2.3 Cl-Alpha Graph

The total produced lift is explained by Equation 2.1 in [18] is explained below:

$$L = 0.5 * \rho * V^2 * S * Cl \quad (2.1)$$

Here,

L: Total produced lift force (N)

ρ: Density of air (kg/m^3)

V: Velocity of incoming air (m/s)

S: Projected area of the wing (m^2)

Cl: Lift coefficient (unitless)

As the angle of attack increases, the Cl coefficient increases; consequently, the total lift increases. This fundamental relation is represented in the Cl-alpha graph below

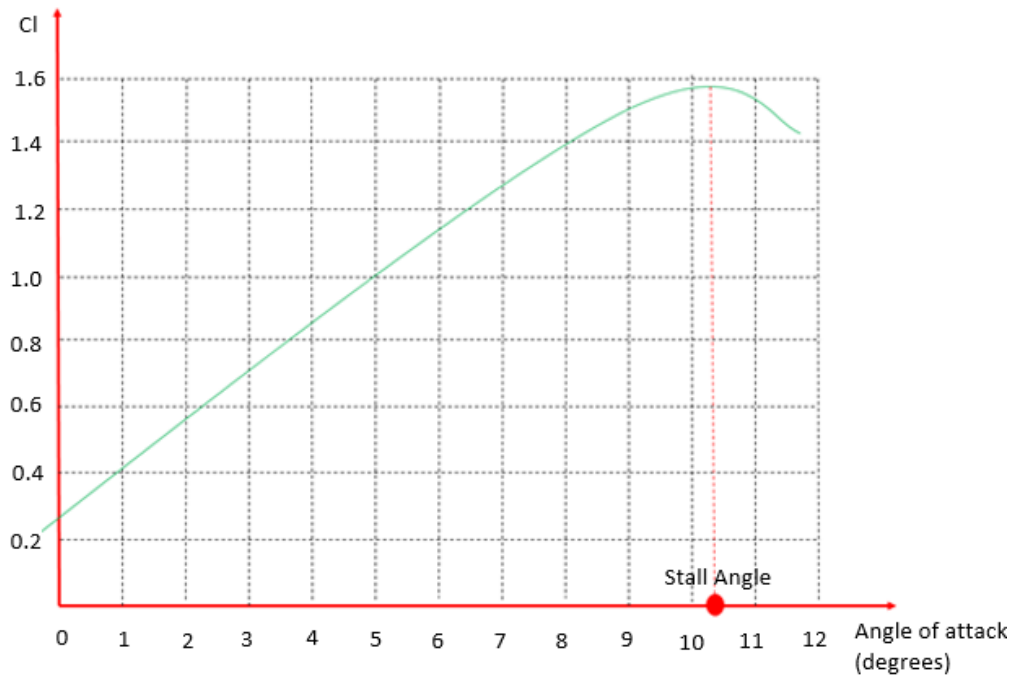

Figure 2.3 Cl-alpha graph

After a certain angle of attack, the Cl coefficient of wing decreases dramatically, forming the angle named as stall angle of wing. The stall point which is presented in Figure 2.3 must be taken into consideration in any aircraft design to ensure flight safety.

2.4 Cd-Alpha Graph

The total produced lift is explained by Equation 2.2 in [18] is explained below:

$$D = 0.5 * \rho * V^2 * S * Cd \quad (2.2)$$

D: Total produced drag force (N)

ρ: Density of air (kg/m^3)

V: Velocity of incoming air (m/s)

S: Projected area of the wing (m^2)

Cd: Lift coefficient (unitless)

As the angle of attack changes, the Cd coefficient changes. This relation is represented in the Cd-alpha graph below.

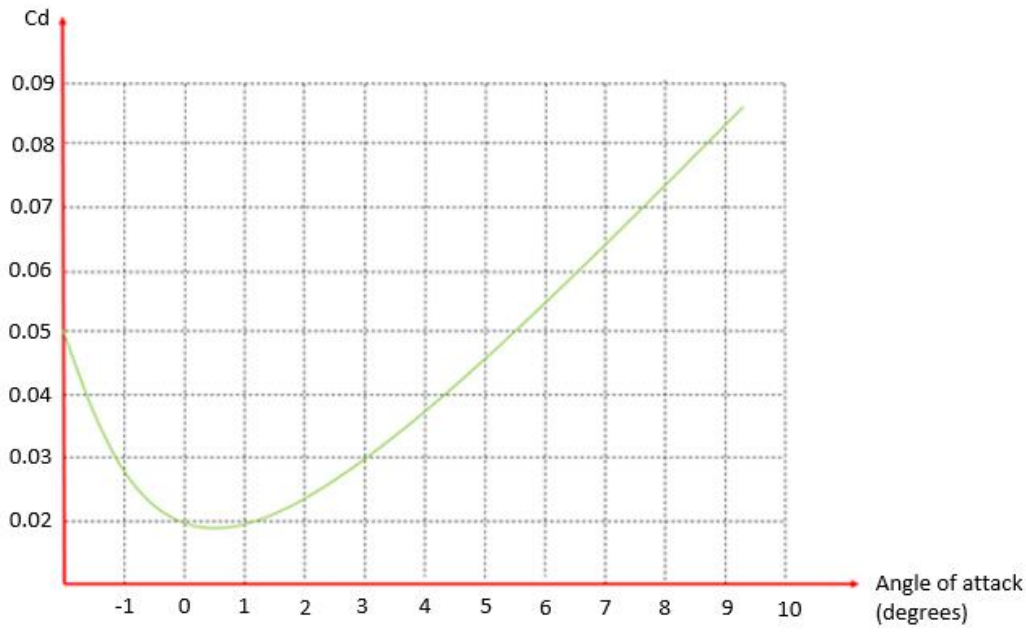

Figure 2.4 Cd alpha graph

As it can be seen from Figure 2.4, there is a minimum value of the Cd coefficient at nearly zero-degree angle of attack. The further it is from that point, the higher the total produced Cd.

2.5 Cl-Cd Graph

Cl-Cd graph is one of the most important graphs which is used in the design process of aircrafts. Designers generally want to get the maximum lift coefficient while keeping the drag coefficient at minimum for long endurance UAVs. A tangent line to the Cl-Cd curve which is displayed in Figure 2.5, which goes through origin, would represent the maximum Cl-Cd ratio. The angle between this line and Cd axis gives the angle of attack, which provides the maximum Cl/Cd ratio, the best operation point for maximum endurance.

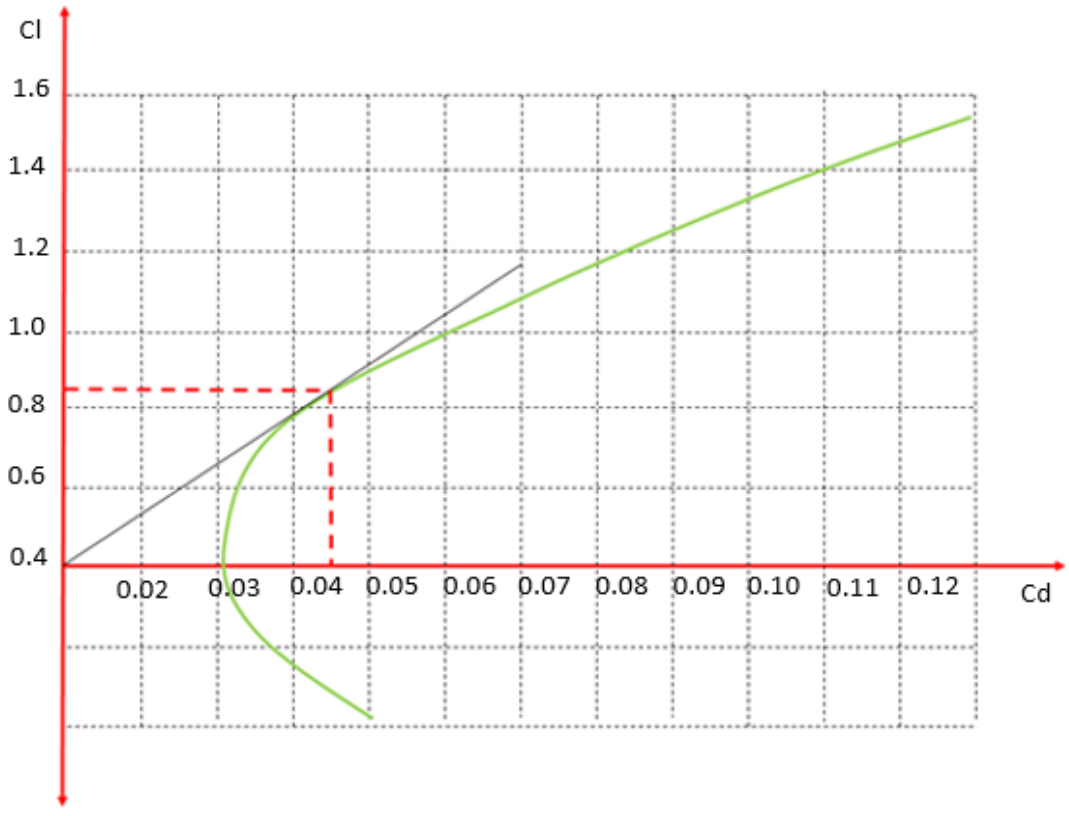

Figure 2.5 Cl-Cd graph

2.6 Neutral Point

Neutral point (NP) is a flight mechanics term, which is used to define the static stability of aircraft. It is the point where aerodynamic moments acting on the whole aircraft does not change as a result of a change in angle of attack of the aircraft [33]. Some of the aerodynamic forces acting on aircraft is presented in Figure 2.6.

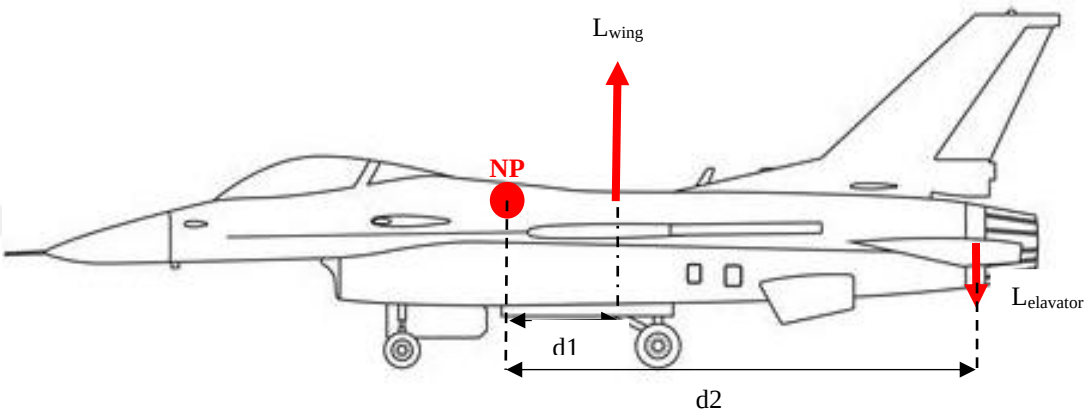

Figure 2.6 Neutral point position

2.7 Center of Gravity Position

The position of center of gravity (CG) that is presented in Figure 2.7, Figure 2.8, and Figure 2.9 is an important parameter for static stability of an aircraft. If the center of gravity is at the front of neutral point, then the aircraft is statically stable. If it is at the back of neutral point, then the aircraft becomes statically unstable. If the position of center of gravity is on the neutral point, then the aircraft has neutral stability [21].

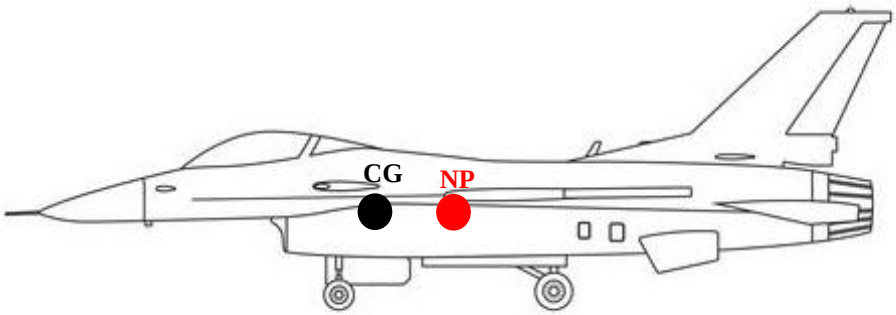

Figure 2.7 Statically stable configuration

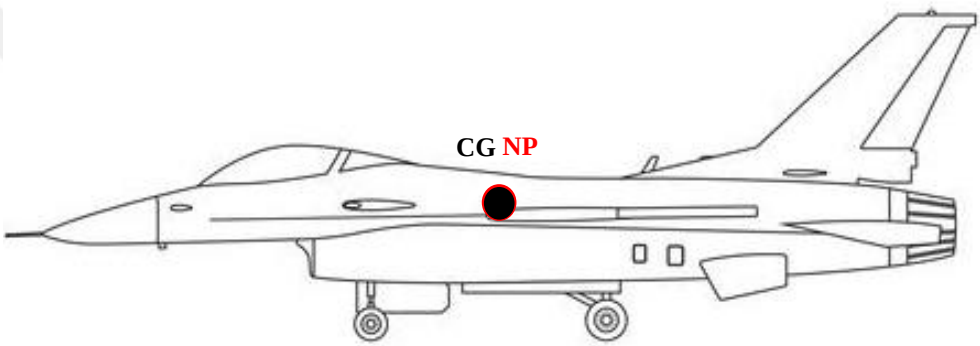

Figure 2.8 Statically neutral configuration

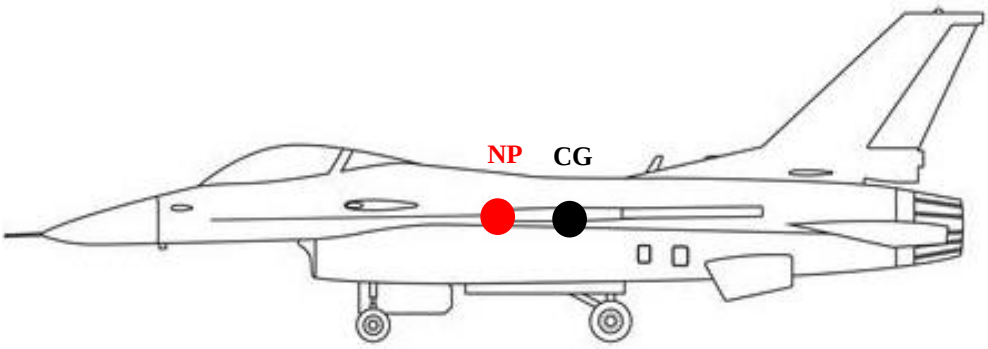

Figure 2.9 Statically unstable configuration

In the variable incidence wing design proposed in this study, as the angle of attack of wing is increased, so does the total produced lift. The study also considered the design of variable incidence ruddervator mechanism.

CHAPTER 3

PROPOSAL OF A NEW DESIGN CONCEPT

3.1 History of Variable Incidence Wing Concept

Variable incidence wing allows aircrafts to increase and decrease the angle of attack of wing only. Therefore, designers can increase and decrease the produced lift during take-off and landing. While adjusting the angle of attack of wing, the fuselage remains horizontal so that this maintains the minimum fuselage drag. The variable incidence wing patent, obtained in 1912, belongs to George Boginoff [19]. F-8 Crusader which is presented in Figure 3.1 is one of the variable incidence wing users. Its first flight was conducted on 25 March 1955. This aircraft was extensively used by US navy, with totally 1219 of them produced [20].

Figure 3.1 Variable incidence F-8 Crusader

In 1950s, landing on a carrier was still challenging. When the aircraft approached the carrier, the pilot would try to reduce the approaching speed of the aircraft to be able to stop in a small distance. Therefore, pilots would increase the angle of attack of aircraft

to decrease the approaching speed. Sometimes, the pilot even could not even see the runway due to extremely high angle of attack, which was a big problem for pilots. To combat this problem, F-8 Crusader designers decided to use variable incidence wing mechanisms, which enabled the pilot to increase the angle of attack of wing rather that of the whole aircraft. This worked perfectly, i.e. pilots did not need to increase the angle of attack of the whole aircraft; instead, they increased the angle of attack of wing only. Ultimately, the length of runway required shortened both for landing and take-off.

3.2 A New Design Proposal

This study offers variable incidence wing and ruddervator mechanisms for UAV's. It is targeted that a short take-off will be achieved by changing the angle of attack of wing from -15 degrees to +15 degrees. Here, the incidence angle of wing changes with respect to fuselage while the angle of attack of fuselage remains constant as it is represented in Figures 3.2 and 3.3, respectively. Such a variable incidence wing mechanism design can provide the following benefits:

- Greater produced lift of wing in case of need
- Achievement of the most efficient angle of attack that meets the maximum endurance and $(Cl/Cd)_{maks}$ ratio through a couple of flight tests
- Increase in the acting force on wheels. The maximum applicable brake force depends on the acting force on wheels. To increase the maximum applicable brake force, the acting force on wheels should be increased. Decreasing the angle of attack of wing would produce negative lift, and consequently the acting force on wheels could be increased.

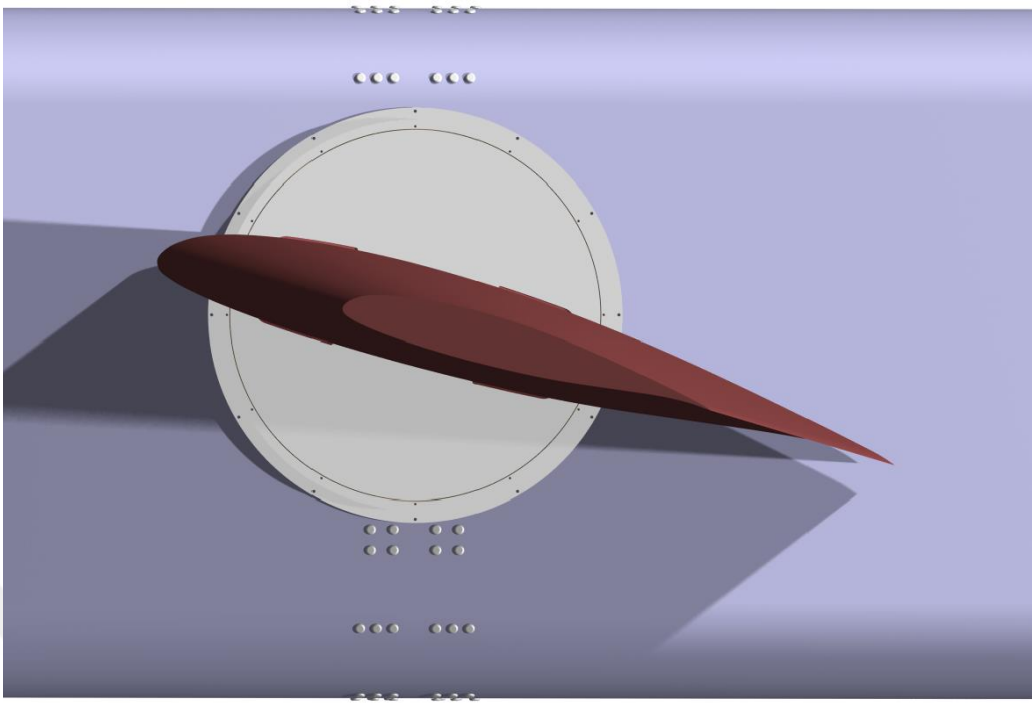

Figure 3.2 +15-degree incidence angle position of wing

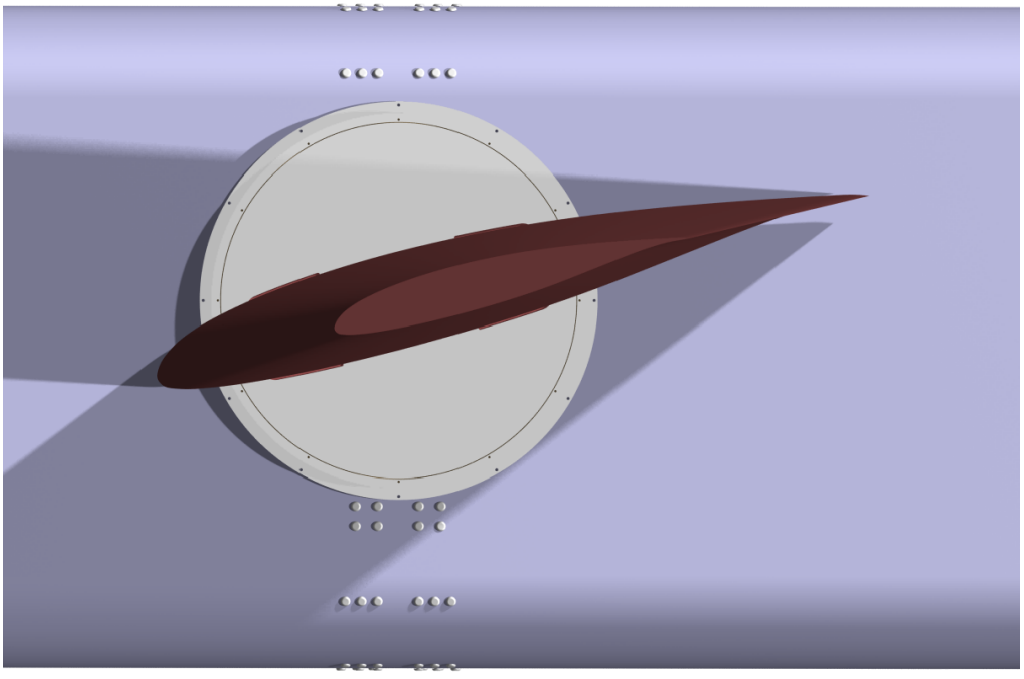

Figure 3.3 -15-degree incidence angle position of wing

A change in the incidence angle of wing changes the flight mechanics characteristics of aerial vehicles, the main ones being the lift and the drag. Designers aim to increase the lift force, so the angle of attack of wing is intended to be increased. Another affected parameter is the drag force. Increase in the angle of attack of wing can cause the greater drag force, thus more fuel consumption, but this is not a huge problem as long as the engine provides sufficient thrust. In extremely stable planes, elevators lose their effectiveness, while in extremely unstable planes, it is hard to control the plane. This moment changes in the angle of attack of ruddervator or elevator has become highly critical. Hence, in this thesis, the variable incidence ruddervator mechanism is proposed to be mandatory for the variable incidence wing mechanism as it is presented in Figure 3.4 and Figure 3.5, respectively.

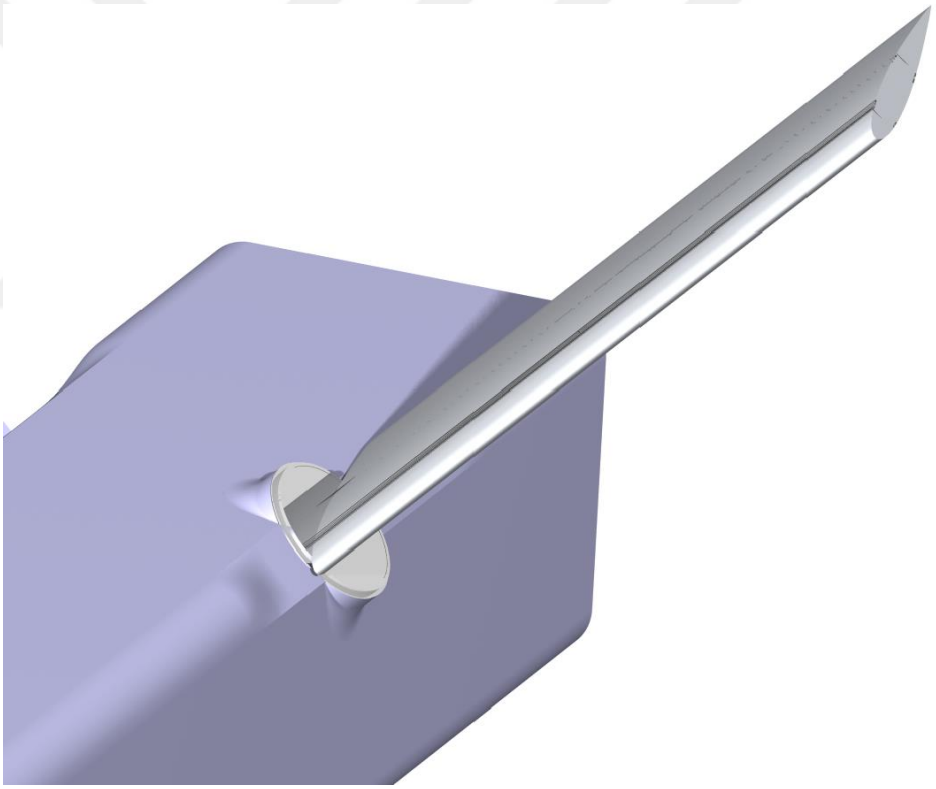

Figure 3.4 -15-degree incidence angle position of ruddervator

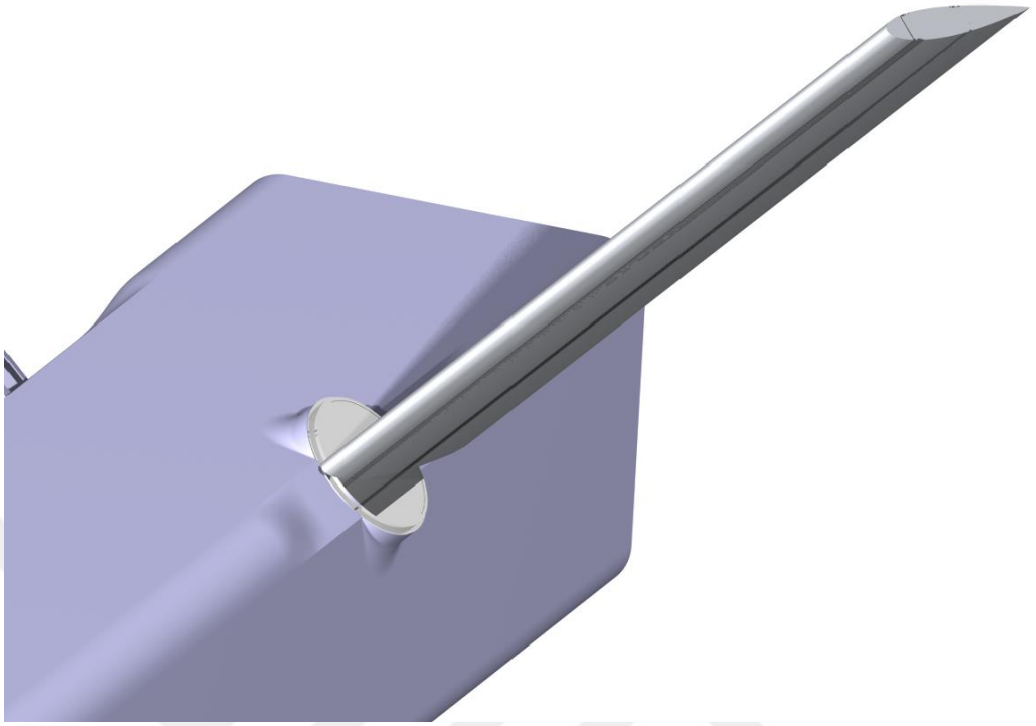

Figure 3.5 +15-degree incidence angle position of ruddervator

3.3 Design of Wing

A special wing and its mechanisms were designed within the scope of this study. These designs allow a 1425 kg aerial vehicle to take-off within a 200 m runway distance without using any accelerant catapult system. The projected area and dimensions of the designed wing are seen with its retracting center as shown in Figure 3.6.

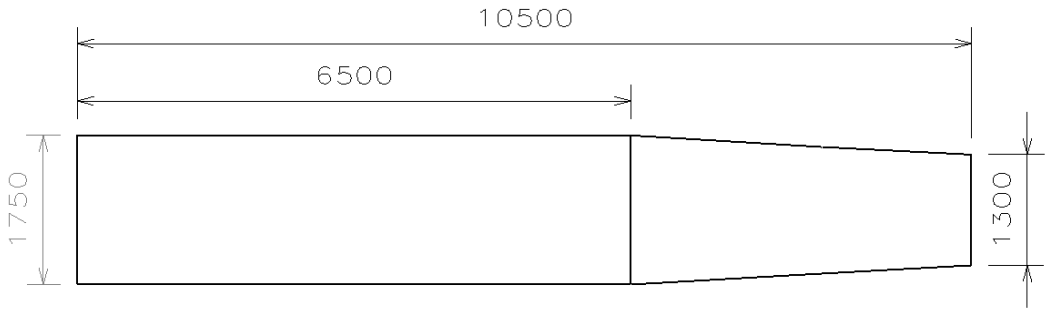

Figure 3.6 Wing dimensions

There is a retracting center at 6500 mm. Front and isometric views of the retracted wing are displayed in Figures 3.7 and 3.8, respectively.

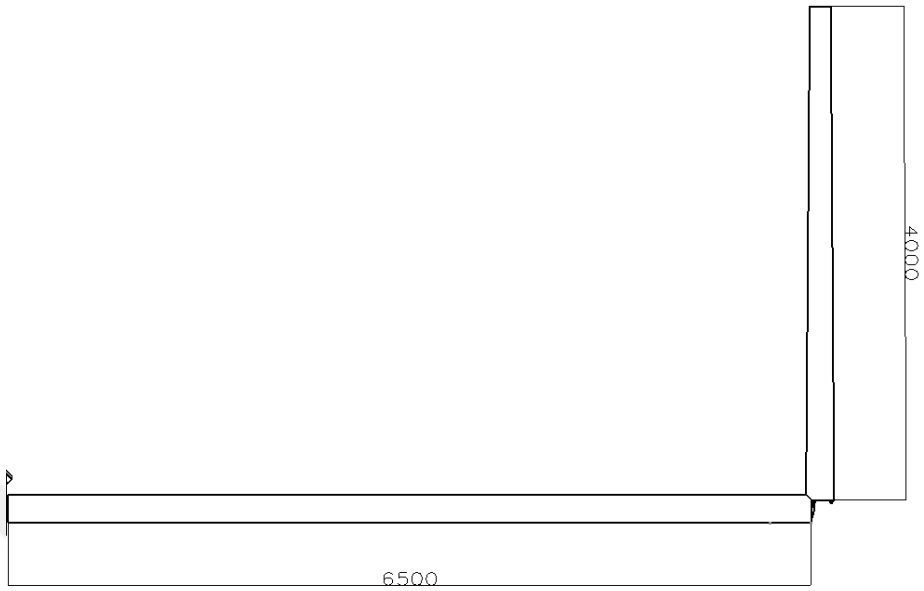

Figure 3.7 The retracted wing front view

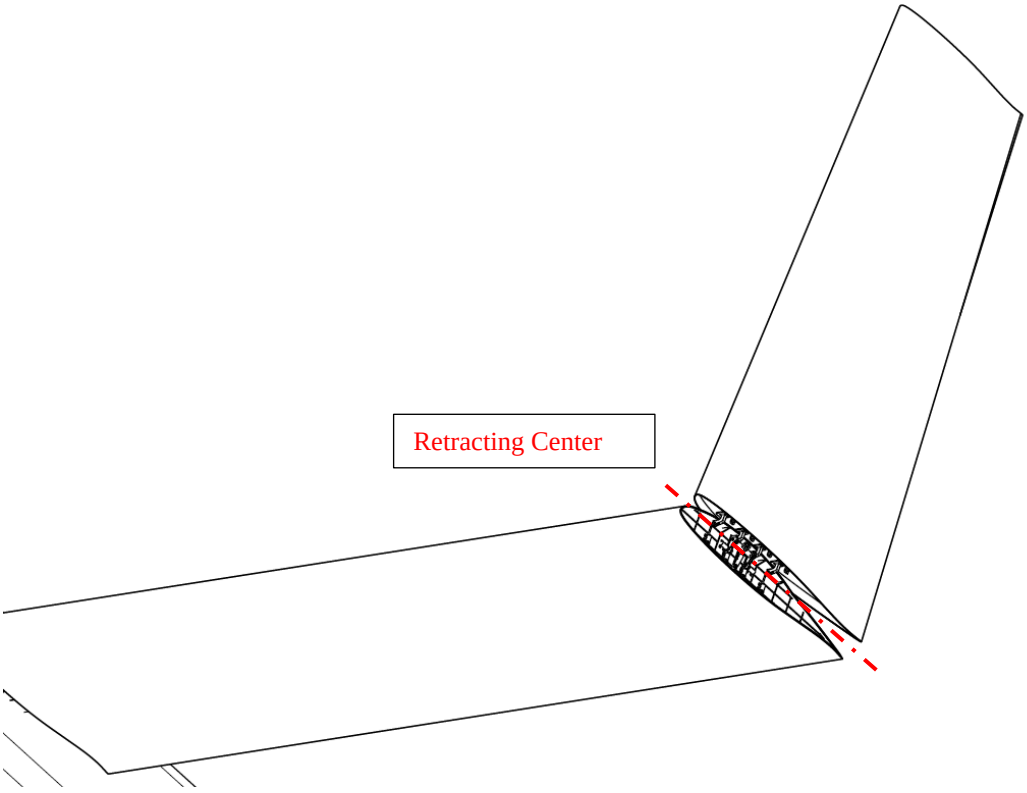

Figure 3.8 The retracted wing isometric view

There are two wing configurations: a retracted wing and an unretracted wing. The total produced lift for both configurations were calculated by using the XFLR5 software. The properties of the unretracted wing were calculated as following:

Wing projected area: 34.95 m^2

Aspect ratio: 12.618

Taper ratio: 1.346

The aerodynamic properties of the unretracted wing are shown in Table 3.1. Its Cl-alpha graph, which was also calculated by using the XFLR5 software, is presented in Figure 3.1. As the Cl-alpha graph was nearly linear, the first order curve fitting was applied to express it mathematically. The linear formulation in MATLAB Simulink was used. This linear 1st order equation is presented in Figure 3.9 as Cl = (0.089 * alpha) + 0.38

Table 3.1 Aerodynamic properties of the unretracted wing

alpha	Beta	Cl	CDi	CD	Cm	QInf	XCP
0	0.000	0.362608	0.003463	0.003463	-0.068506	642.068	0.5221
1.000	0.000	0.452683	0.005375	0.005375	-0.060551	574.649	0.4717
2.000	0.000	0.542539	0.007700	0.007700	-0.052604	524.909	0.4381
3.000	0.000	0.632127	0.010433	0.010433	-0.044676	486.292	0.4141
4.000	0.000	0.721399	0.013567	0.013567	-0.036777	455.210	0.3961
5.000	0.000	0.810305	0.017093	0.017093	-0.028914	429.512	0.3822
6.000	0.000	0.898799	0.021002	0.021002	-0.021100	407.820	0.3711
7.000	0.000	0.986834	0.025285	0.025285	-0.013341	389.205	0.3620
8.000	0.000	1.074362	0.029929	0.029929	-0.005650	373.013	0.3545
9.000	0.000	1.161338	0.034921	0.034921	0.001967	358.774	0.3481
10.000	0.000	1.247718	0.040249	0.040249	0.009498	346.132	0.3428
11.000	0.000	1.333458	0.045898	0.045898	0.016935	334.819	0.3382
12.000	0.000	1.418513	0.051850	0.051850	0.024269	324.626	0.3342
13.000	0.000	1.502842	0.058090	0.058090	0.031491	315.387	0.3307
14.000	0.000	1.586404	0.064601	0.064601	0.038593	306.968	0.3277
15.000	0.000	1.669159	0.071362	0.071362	0.045564	299.262	0.3250

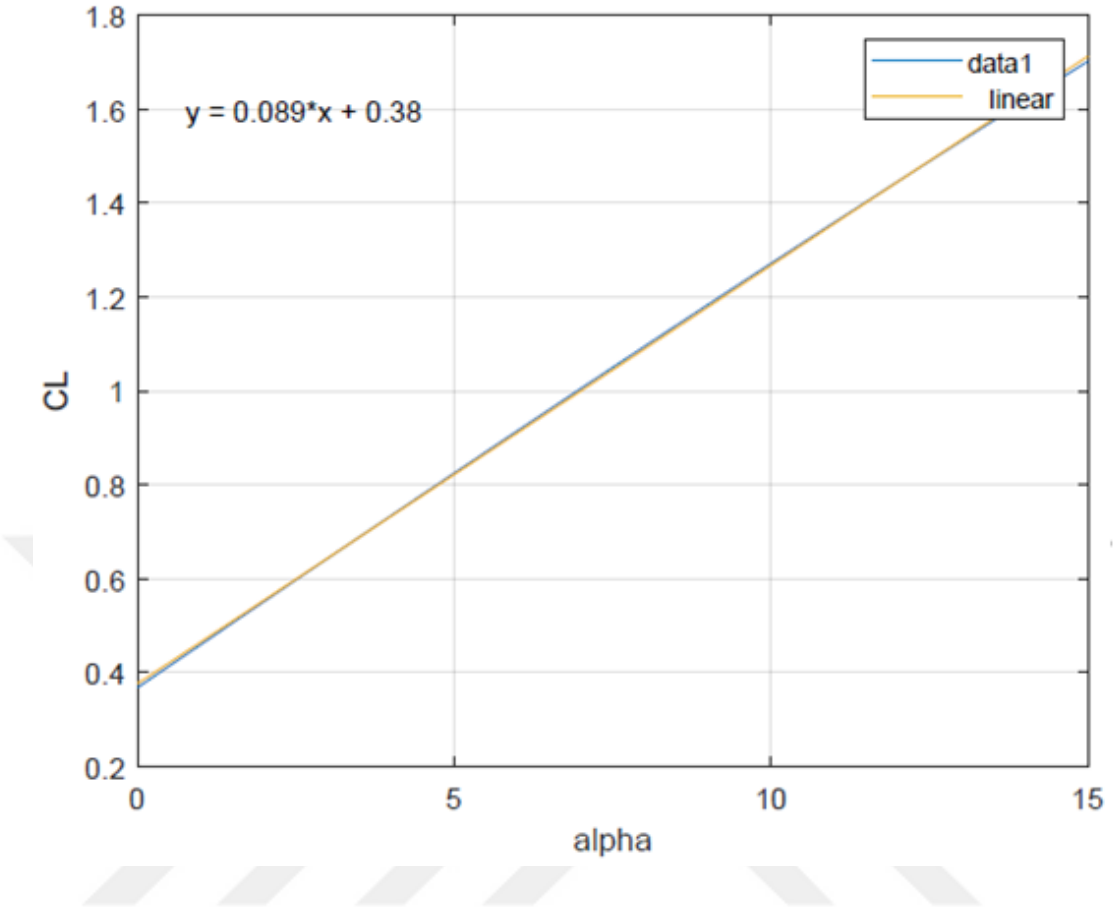

Figure 3.9 Cl-alpha graph of the unretracted wing

The aerodynamic properties of the retracted wing, which were calculated using the XFLR5 software, are shown in Table 3.2. Its Cl-alpha graph, which was calculated by using the XFLR5 software, is presented in Figure 3.10. As Cl-alpha graph was nearly linear, first order curve fitting was applied to express this graph mathematically, this linear formulation was used in MATLAB Simulink. The linear 1st order equation is presented in Figure 3.10 as Cl = (0.077 * alpha) + 0.33

The properties of the retracted wing were calculated as follows by using XFLR5 software:

Wing projected area: 22.75 m^2

Aspect ratio: 7.429

Taper ratio: 1

Table 3.2 Aerodynamic properties of the retracted wing

alpha	Beta	Cl	CDi	CD	Cm	QInf	XCP
0	0.000	0.325062	0.004687	0.010693	-0.178375	509.798	0.9602
1.000	0.000	0.364823	0.005876	0.011787	-0.188026	481.216	0.9016
2.000	0.000	0.404533	0.007199	0.012932	-0.197654	456.987	0.8546
3.000	0.000	0.483775	0.010242	0.015821	-0.216836	417.888	0.7838
4.000	0.000	0.562736	0.01381	0.019623	-0.235902	387.462	0.7331
5.000	0.000	0.641363	0.017894	0.024105	-0.254831	362.935	0.695
6.000	0.000	0.719607	0.022483	0.029173	-0.2736	342.637	0.6654
7.000	0.000	0.797416	0.027566	0.034853	-0.292188	325.491	0.6418
8.000	0.000	0.874741	0.033129	0.04091	-0.310567	310.772	0.6225
9.000	0.000	0.951533	0.039157	0.04755	-0.328721	297.968	0.6066
10.000	0.000	1.027	0.045633	0.054655	-0.346626	286.707	0.5931
11.000	0.000	1.103	0.05254	0.062443	-0.36427	276.712	0.5818
12.000	0.000	1.178	0.059859	0.070784	-0.38163	267.772	0.572
13.000	0.000	1.252	0.067569	0.079416	-0.398673	259.719	0.5635
14.000	0.000	1.325	0.075648	0.088469	-0.415387	252.425	0.5562
15.000	0.000	1.398	0.084073	0.097917	-0.431752	245.783	0.5498

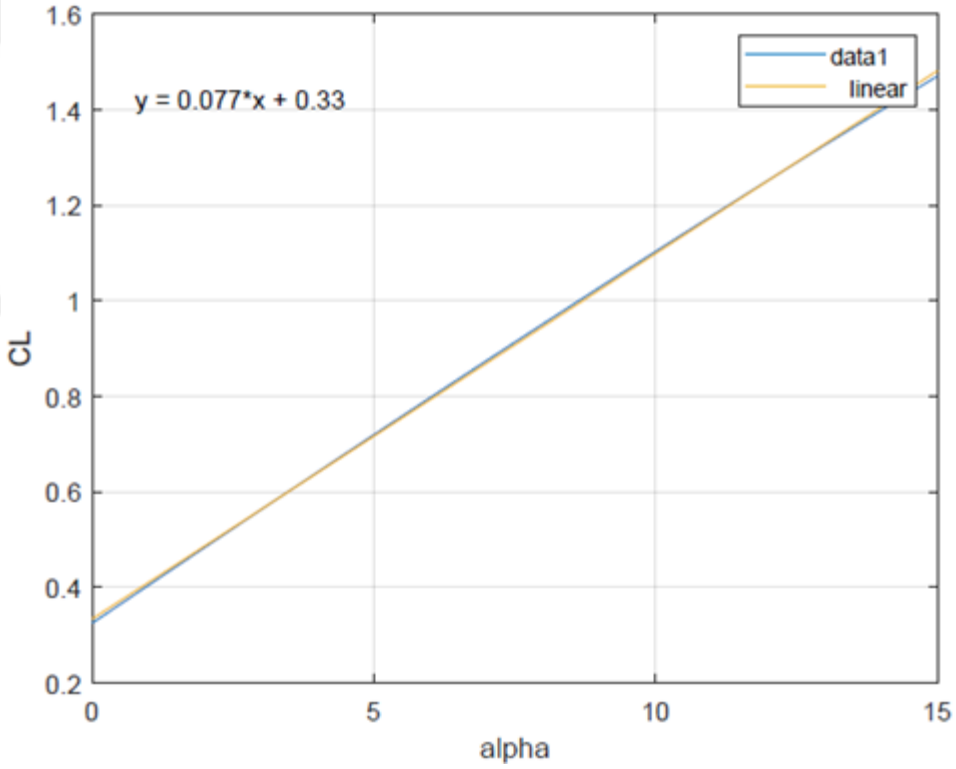

Figure 3.10 Cl-Alpha graph of the retracted wing

3.4 Landing Model

The total weight of an aerial vehicle is assumed as 1200 kg. Its total weight is 1425 kg, so the total difference between the take-off and the landing is 225 kg, which is

attributed to the consumed fuel during the whole flight. A mathematical model of landing is constructed by using the MATLAB Simulink software. A couple of parameters affect the location of the first landing position:

1- Environmental factors (e.g. wind and weather)

2- Maneuvers of ship and ocean waves

3- Reliability of autopilot

By taking these parameters into consideration, some advanced analysis could be performed to set the exact position of the landing. In Figure 3.11 presents the angle of attack of wing with respect to fuselage in the mathematical model. As can be seen in Figure 3.11, the aircraft easily approaches the airfield with the angle of attack at 10-degree. It is assumed that the landing starts at zero second. Touchdown could be detected by using inertial measure units of aerial vehicle due to high vertical acceleration during the touchdown process. One second after the touchdown, the angle of attack of wing to fuselage starts to decrease from +10-degree to -10-degree within two seconds. This angle change starts at the first second and ends at the third second, which means the total activity takes place only in two seconds. It is expected that variable incidence mechanisms supply enough torque and power values for this work to be accomplished within two seconds. To satisfy this requirement, all forces acting on the wing during this movement, such as inertial forces, aerodynamic forces, and ground effects, must be taken into consideration when selecting the true actuator mechanism. If +10 to -10-degree movement in two seconds causes a heavy mechanism, then +10 to -10 tour can be completed in more than two seconds. Another important phenomenon at this point is that the incidence angle of wing is set at -10-degrees after the touchdown. There are two reasons for this:

1- To increase the drag effect of wing for a reduced stopping distance

2- To increase the acting force on the main landing gear so that maximum brake force can be applied without slip

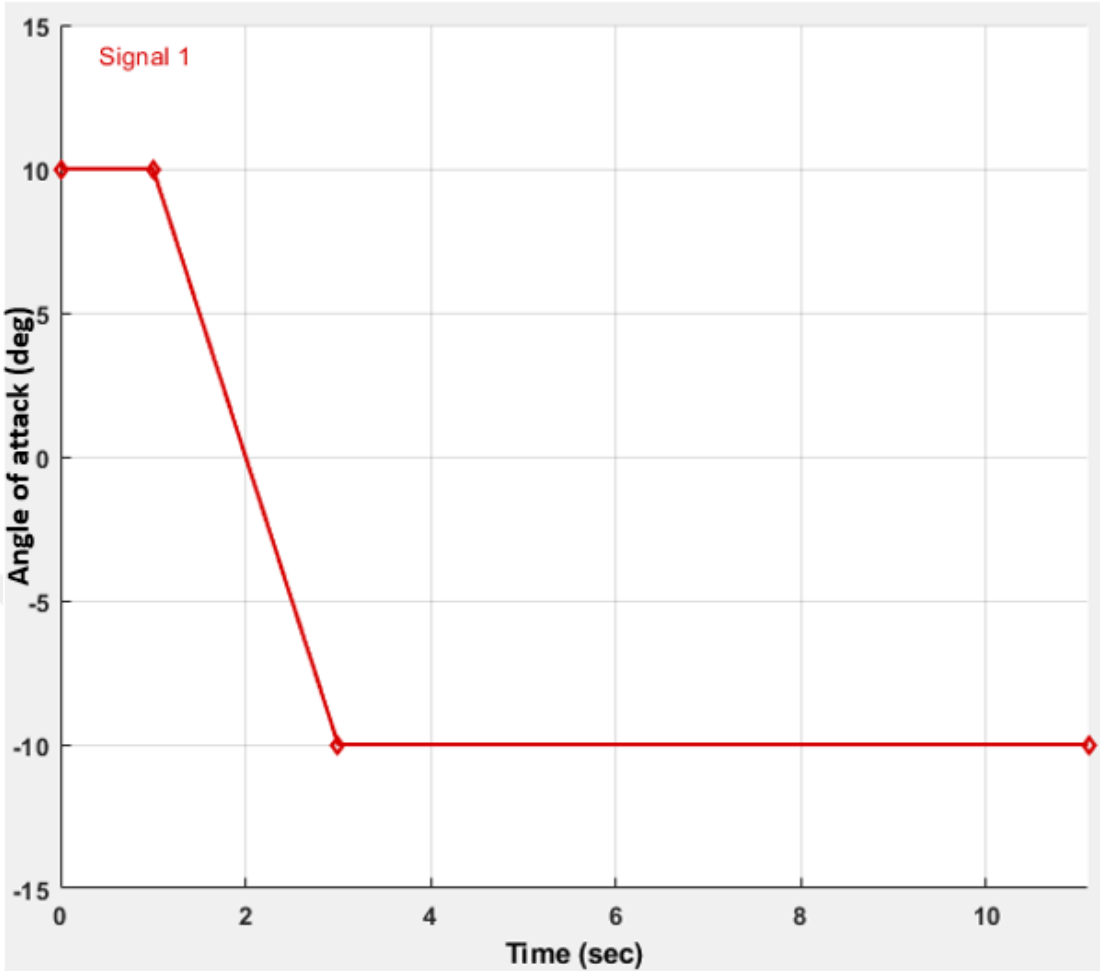

Figure 3.11 Angle of attack of wing – time (s)

One second after the angle of attack of wing becomes -10-degree which is the 4th second of landing, the main landing gear applies the brake force constantly until the UAV stops. After waiting, or when the angle of attack of wing becomes -10-degree, the acting force on the main landing gear should completely return to negative and the fluid flow over the wing reaches a steady state. To confirm this assumption, advanced CFD analysis must be performed. If this one-second waiting time is too long to reach the steady state according to the CFD analysis, it can be reduced, so the stopping distance can be reduced, too. If it is not enough to reach the steady state in the light of CFD analysis, then one-second waiting time should be increased, which is bound to, however, increase the stopping distance. Tire-road friction coefficient depends on meteorological parameters causing the asphalt to be wet, rainy, or icy [22]. Another parameter which changes with time is the lift force that the wing produces (Figure

3.12). If the change of the lift force generated by wings during landing is as seen in Figure 3.12, then it can be inferred that that, during 0-1 seconds, the total produced lift decreases despite the unchanging angle of attack of wing in this step. It decreases because the velocity of aerial vehicle decreases due to the drag force and the friction between tire and road. The produced lift force decreases remarkably in the first-third second, even returning to the negative sign in this short time step. Negative lift force means that wings are producing force at the ground direction, which causes greater force on landing gears. Negative lift decreases in the third-fourth second due to the decrease in velocity in this time step. After the 4th second, as the velocity of unmanned aerial vehicle decreases, the total produced negative sign lift also decreases until it reaches zero.

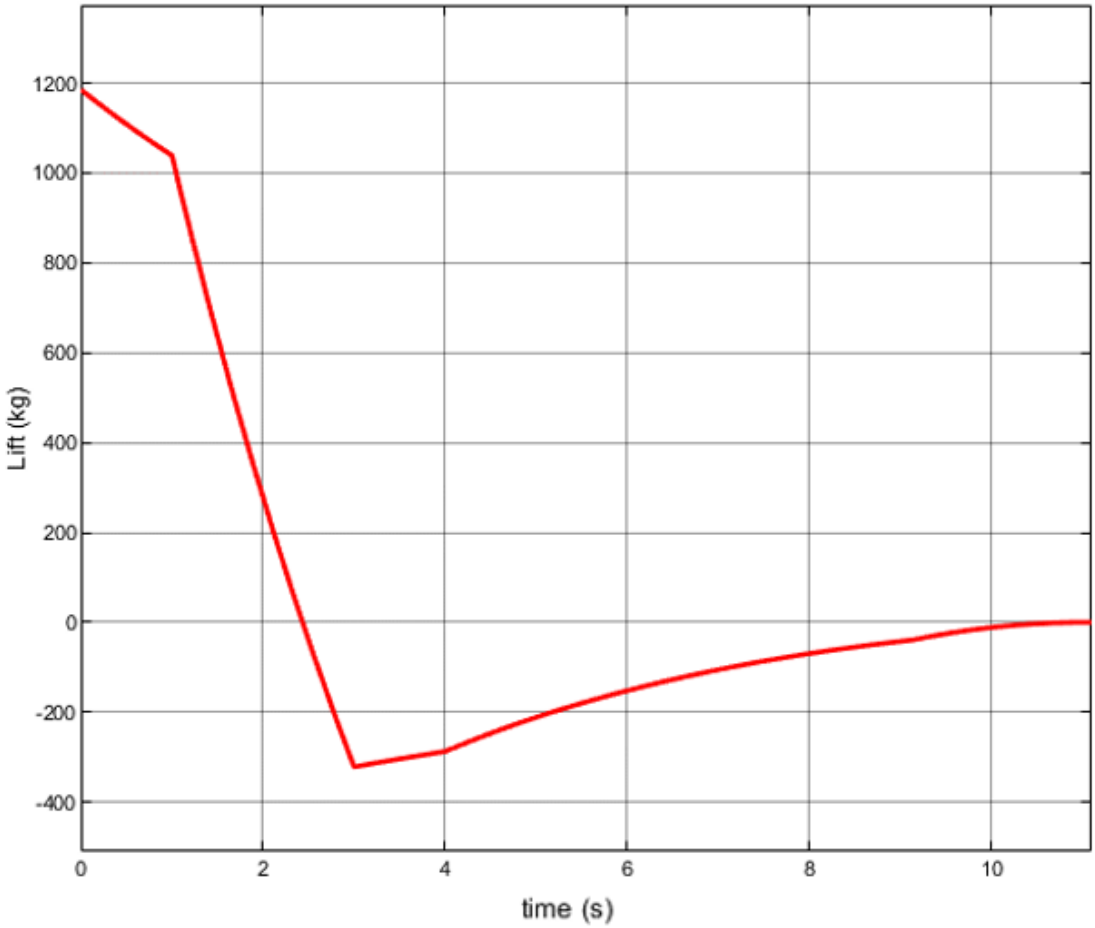

Figure 3.12 Lift force (Newton) - time (s)

The mathematical model was developed by the MATLAB Simulink software in this study, the drag force is just the drag force of the wing; other aircraft parts' drag effects were not included to simplify the model. In other words, aircraft components like fuselage and landing gear, except the wing, has no drag effect on the mathematical model explained in this study. As can be clearly seen in Figure 3.13, the drag force produced by the wing decreases as the velocity of the aerial vehicle decreases until it reaches zero.

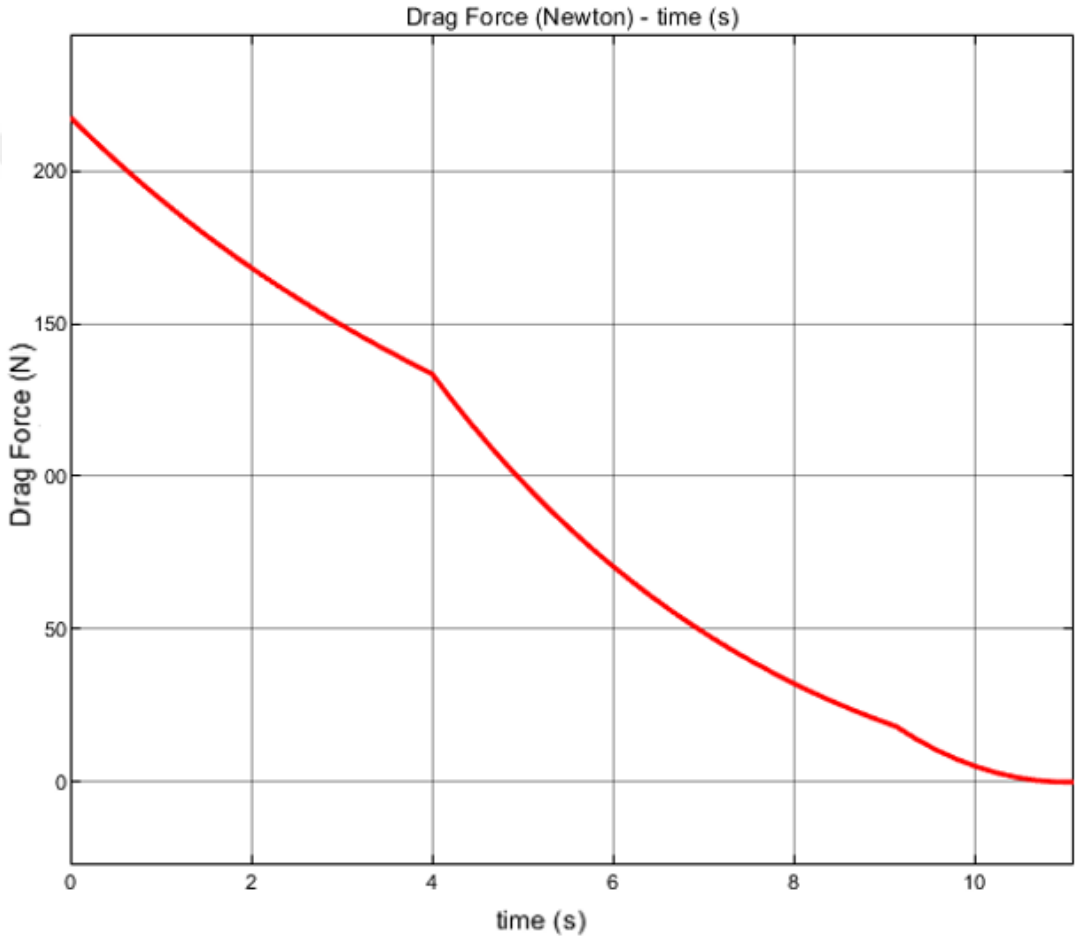

Figure 3.13 Drag force (Newton) - time (s)

Another function that is used in the landing mathematical model is skyjump stopping effect. This function is expressed as "m.g.cos (12)". his formula was used to present the stopping effect of a skyjump ramp which has a 12-degree angle. The starting point of the skyjump ramp was assumed to be at 172 meters, and the mathematical model was based on this. In other words, the last 30 meters of the runway was assumed as the

skyjump slope. Stopping force caused by the 12-degree skyjump ramp is shown in Figure 3.14.

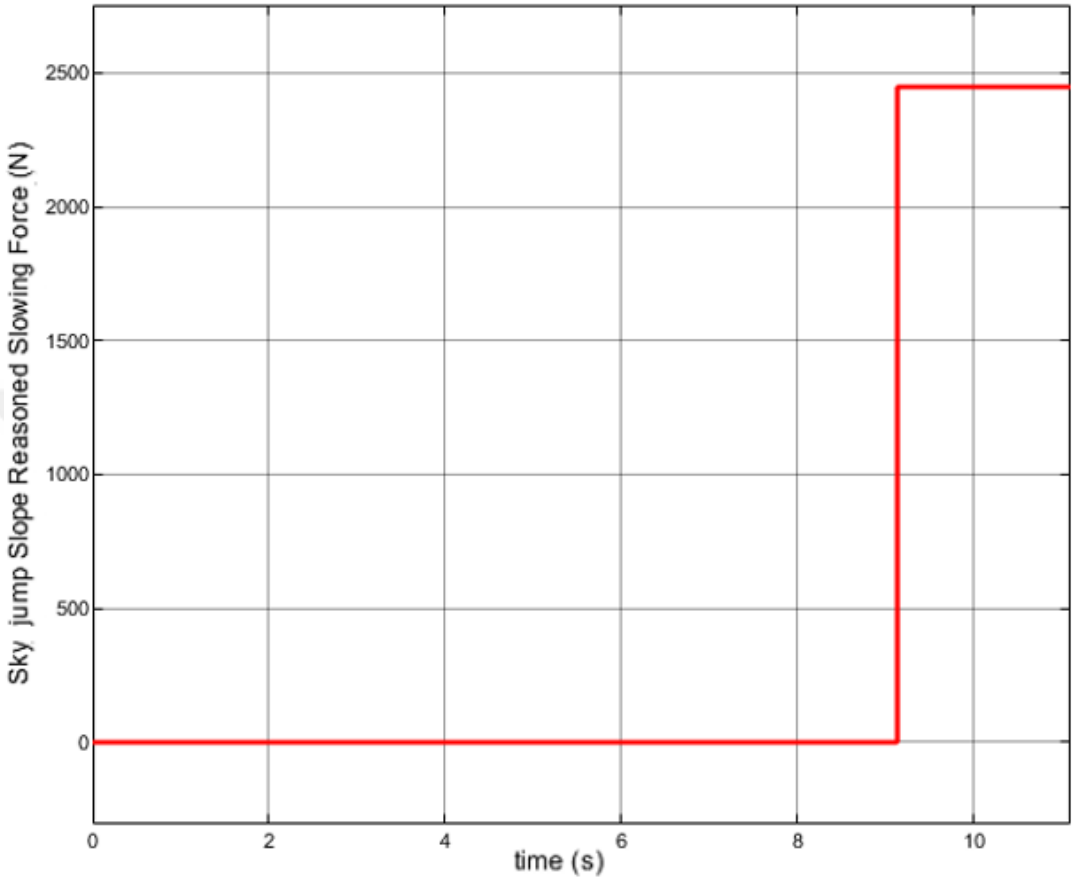

Figure 3.14 Skyjump slope reasoned slowing force (Newton) - time (s)

This study proposes two parameters to stop an aerial vehicle on carrier. The first one is the drag force. As discussed earlier, to increase the drag force, the angle of attack of wing is rotated -10-degree at the first second of landing. The second parameter, and indeed the most important parameter, is the brake force applied to the main landing gear. However, this brake force's maximum application value keeps changing. The two most important parameters that the maximum applicable brake force depends on could be sorted out as follows:

1- Friction coefficient between the asphalt and tire

2- Meteorological conditions of asphalt

No matter how much brake force is applied by a brake system, the effective brake force is defined by the tire-asphalt friction coefficient. In fact, it is as important as the brake system assembled into the aerial vehicle simply because the applicable brake force is proportional to the friction force between the tire and road. If applied brake force exceeds the friction force between the tire and the road, then the tire slips. If the applied brake force is less than the friction force, then the braking phenomenon is insufficient. The brake force can be transmitted as the friction force between the tire and road. This maximum transmittable brake force can be found by the following formula:

$$Fs = \mu.N \qquad (3.1)$$

Fs: Friction force

μ: Friction coefficient between tire and asphalt

N: Acting force on main landing gear

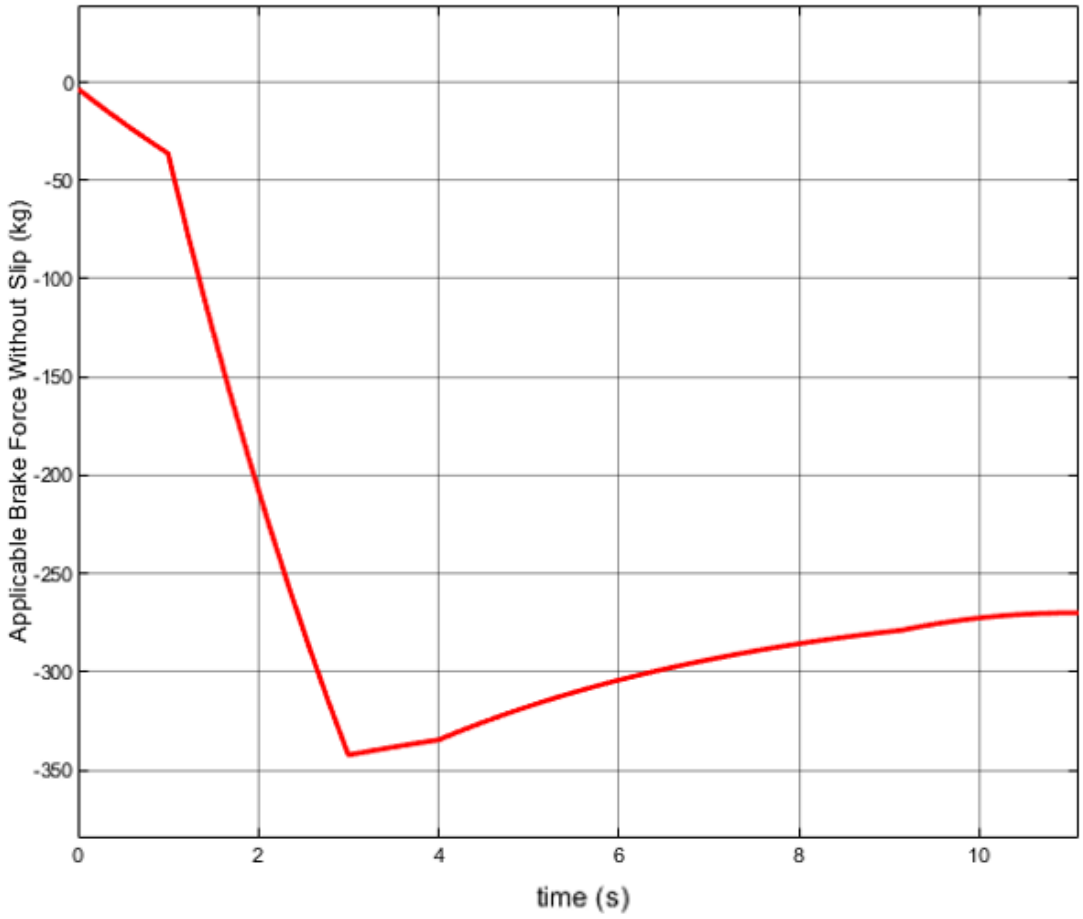

Figure 3.15 Applicable brake force without slip (Newton)

The maximum applicable instant brake force can be as much as the instantly changing friction force, which is represented by Fs. If the braking force, generated by brake, is exceeded, the tire begins to slip, which may potentially cause a catastrophic failure. Thus, designers must perform certain tests to assess the coefficient of friction between the tire and the road with different meteorological conditions. However, as it was not possible to perform this test, this thesis continued based on some referenced data. Therefore, although it is stated in [23] friction coefficient between the tire and wet asphalt changes between 0.3 and 0.8, the friction coefficient was selected as 0.25 to be on the safe side. In Figure 3.15, the friction force between tire and road is presented with the friction coefficient of 0.25. This graph also indicates the maximum brake force allowed to prevent skidding.

If the aerial vehicle can land safely when the runway asphalt is wet, it can land much more easily when the runway asphalt is dry because of the friction coefficient difference between dry and wet road, so in this thesis the mathematical model and all the related visual representations are based on the wet runway condition. The maximum brake force applied to prevent skidding exceeds 250 kg after the 2.25^{th} second of landing as can be seen in Figure 3.15, and after this time, the maximum applicable force is always beyond 250 kg, which means 250 kg brake force can be applied without causing any skid after the 2.25^{th} second until the aerial vehicle stops. As it is understood from Figure 3.15, greater brake force can be applied, but to be conservative, this study did not apply any brake force greater than 250 kg. Another conservative choice in the mathematical model was that the brake force is not applied after the 2.25^{th} second, but rather after the 4^{th} second. The applied brake force can be seen in Figure 3.16.

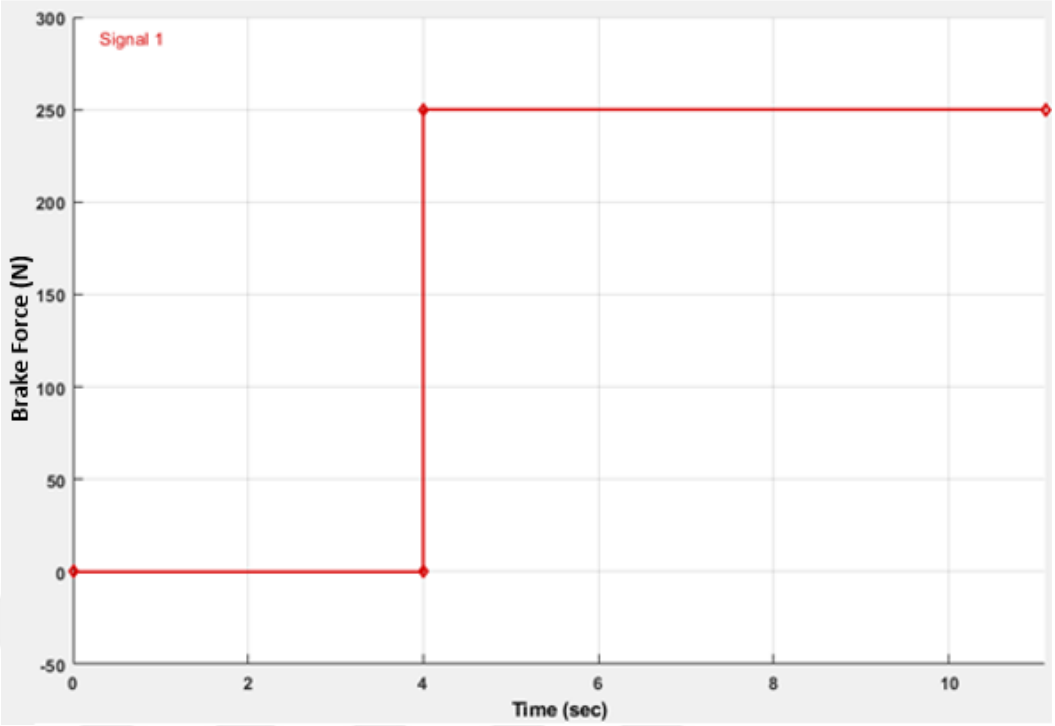

Figure 3.16 Applied brake force

Many expressions are used in this thesis to express the forces acting on the unmanned aerial vehicles on lateral direction. The force graph pertaining to all lateral forces acting on aerial vehicles can be seen in Figure 3.17, which manifests that the lateral resultant force acting on the unmanned aerial vehicle decreases during the first 0-4 seconds. It is simply because of the reduction in drag force associated with the loss of speed at this time step. The resultant force increases abruptly in the negative direction, reach nearly -400 at the 4^{th} second, due to the applied brake force at the 4^{th} second (Figure 3.15). After the 9^{th} second, a sudden increase takes place in the resultant force in the negative direction skyjump causes the stopping effect of m.g.sin (12) as shown in Figure 3.14.

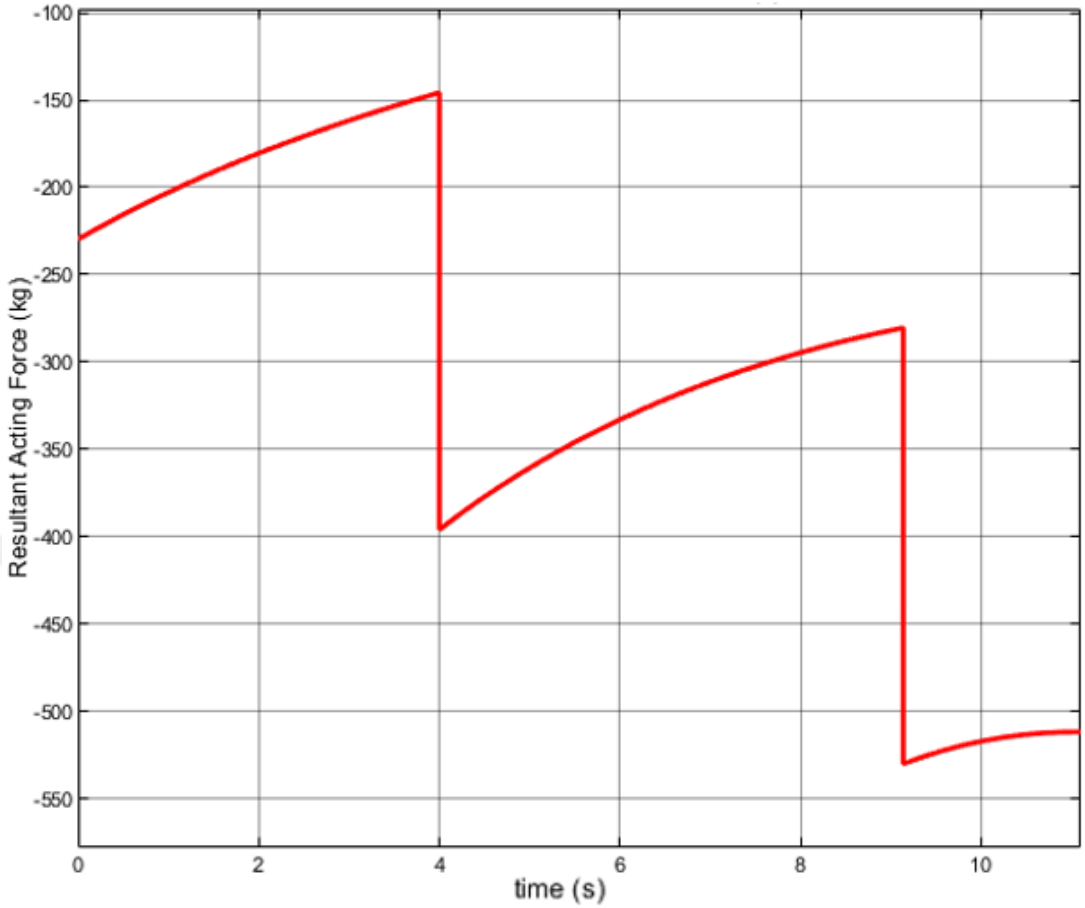

Figure 3.17 Resultant acting force (kg) - time (s)

The velocity-time and distance-time graphs of unmanned aerial vehicles' landing can be seen in Figure 3.18 and 3.19, respectively.

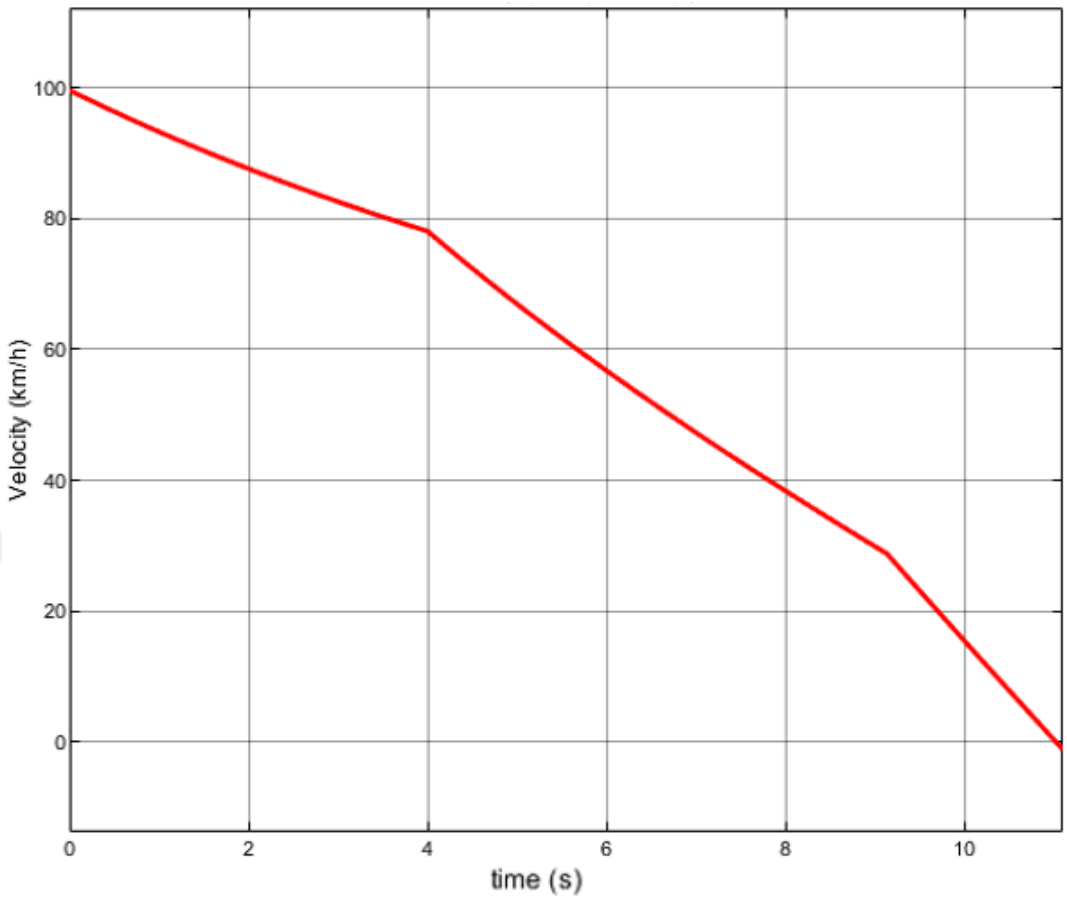

Figure 3.18 Velocity (km/h) - time(s)

As it is seen in Figure 3.19, the unmanned aerial vehicle stops at the last 10th meter of the runway. An advanced analysis would prove that the unmanned aerial vehicle can stop during landing by using less of the runway. At this point, this thesis adopts some conservative calculations as follows:

1- The friction coefficient taken as 0.25, consequently the maximum applicable brake torque, remained lower than it could be in real life. This value could be fixed to higher values by test campaigns so that maximum applicable brake force could be achieved. Even new tire models could be developed for this carrier based unmanned aerial vehicle to increase coefficient of friction between tire and road during landing.

2- Although 250 kg brake force could be applied after the 2.25th second, it was applied after the 4th second in the mathematical model.

3- Although greater brake force could be applied, as clearly seen in Figure 3.12, only 250 kg brake force was implemented in the mathematical model.

4- The drag force effect of UAV components other than wing is disregarded.

5- It is assumed that there is no spoiler on the wing of UAV to produce drag force during landing. Spoilers are so effective aircraft components that drag force increased during landing.

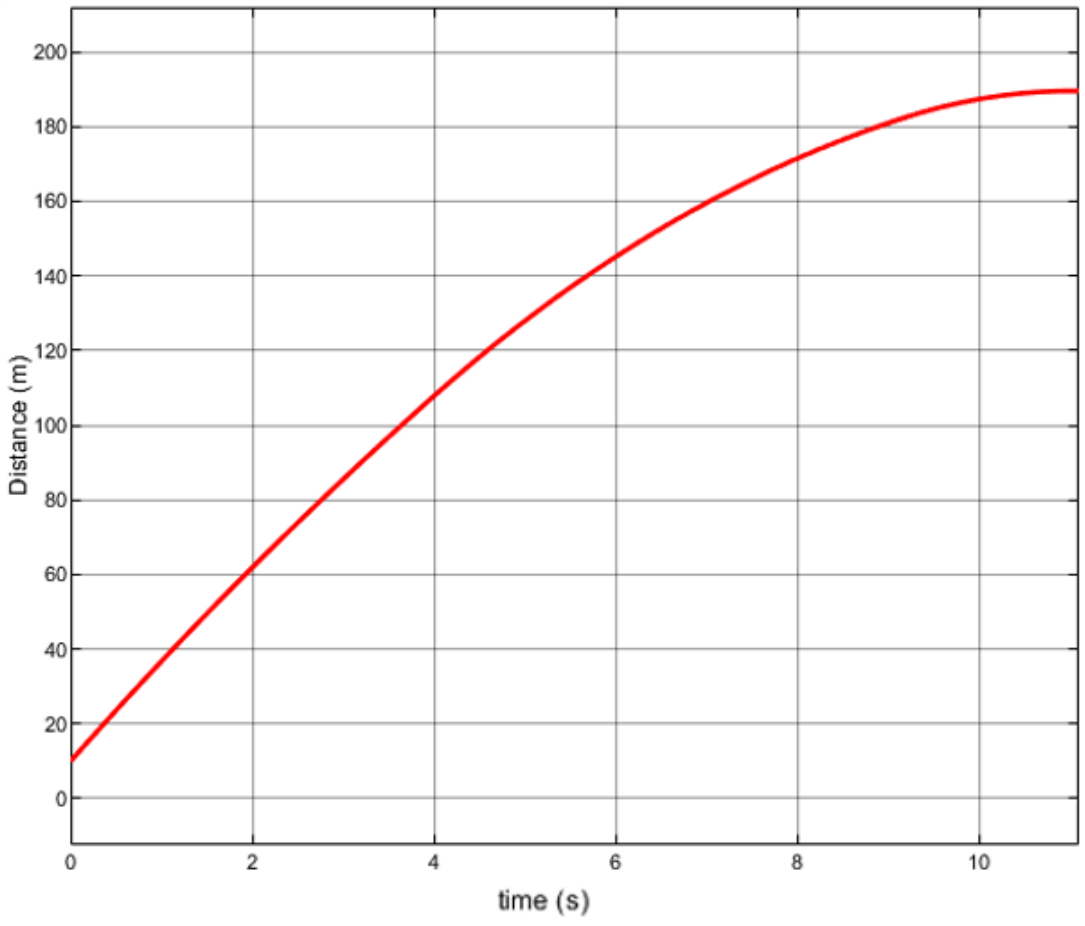

Figure 3.19 Distance (m) - time(s)

3.5 Take-off Model

The total maximum weight of unmanned aerial vehicle is assumed to be 1425 kg. Actually, it could be increased up to 1600 kg technically. To provide the maximum weight of 1600 kg, the angle of attack of wing with respect to fuselage should be greater than 10-degree. However, this situation results in a stall problem. As the angle of attack of wing increases, so does the stall risk. Before increasing the angle of attack of wing by more than 10 degrees, advanced CFD analysis must be performed to determine the stall point of wing so that the maximum applicable limit of the angle of attack could be determined. Consequently, Cl-alpha graph can be obtained, which could be used in instead of the Cl-alpha graph of XFLR5, as presented in Figures 3.9 and 3.10, respectively. The maximum applicable incidence angle could be determined according to the detailed CFD based Cl-alpha graph and the meteorological conditions in which unmanned aerial vehicle must be operated. This advanced analysis can prove that the maximum applicable angle of attack of wing to fuselage could be set to more than 10-degree. It is assumed that total produced thrust is 3000 Newton. To prevent the increase of drag force that is generated by wings, the angle of attack of wing is set to zero degree until the 12^{th} second of take-off. In the 12-14 time step, the angle of attack of wing is increased to 10-degree to provide enough thrust force to keep height. The change in the angle of attack of wing during take-off can be seen in Figure 3.20.

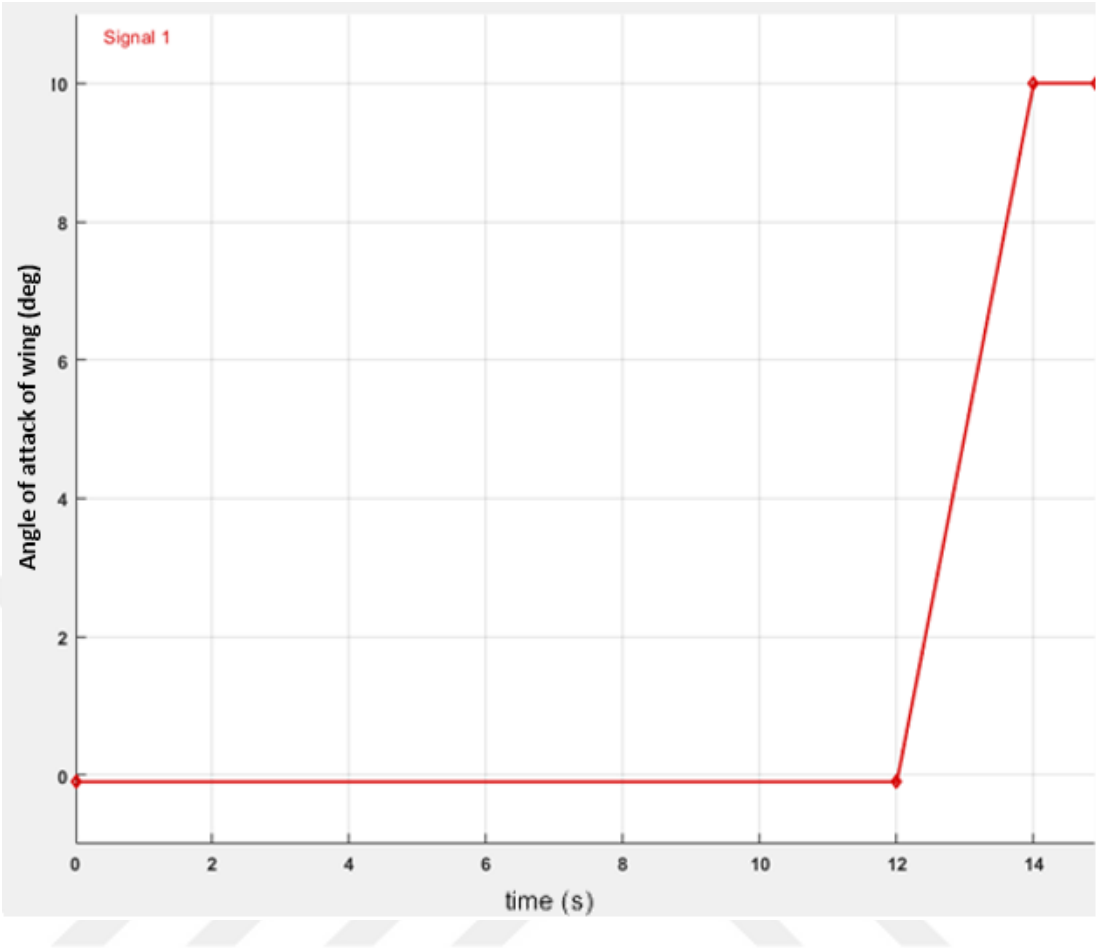

Figure 3.20 Angle of attack of wing - time (s)

Lift force - time graph is presented in Figure 3.21. Although the produced lift force increases gradually until the 12th second of take-off run, an abrupt increase in the produced lift force occurs at the 12th to 14th seconds. This is explained, as seen in Figure 3.20, by a sudden change in the wing's angle of attack during this time step. In just two seconds (12-14th seconds), the total produced lift quadruples. This marked reality confirms the strength of the variable incidence wing idea. If the incidence angle of wing cannot be changed along the runway, take-off of 1425 kg UAV, which has 3000 N engine thrust, would not be possible in 202 m without using the catapult mechanism.

The produced lift force after the 14th second is reduced gradually. The reason is the decelerating effect of sky jump caused by its own ramp. As can be seen in Figure 3.21, the required lift force for take-off of UAV is achieved at the end of a runway.

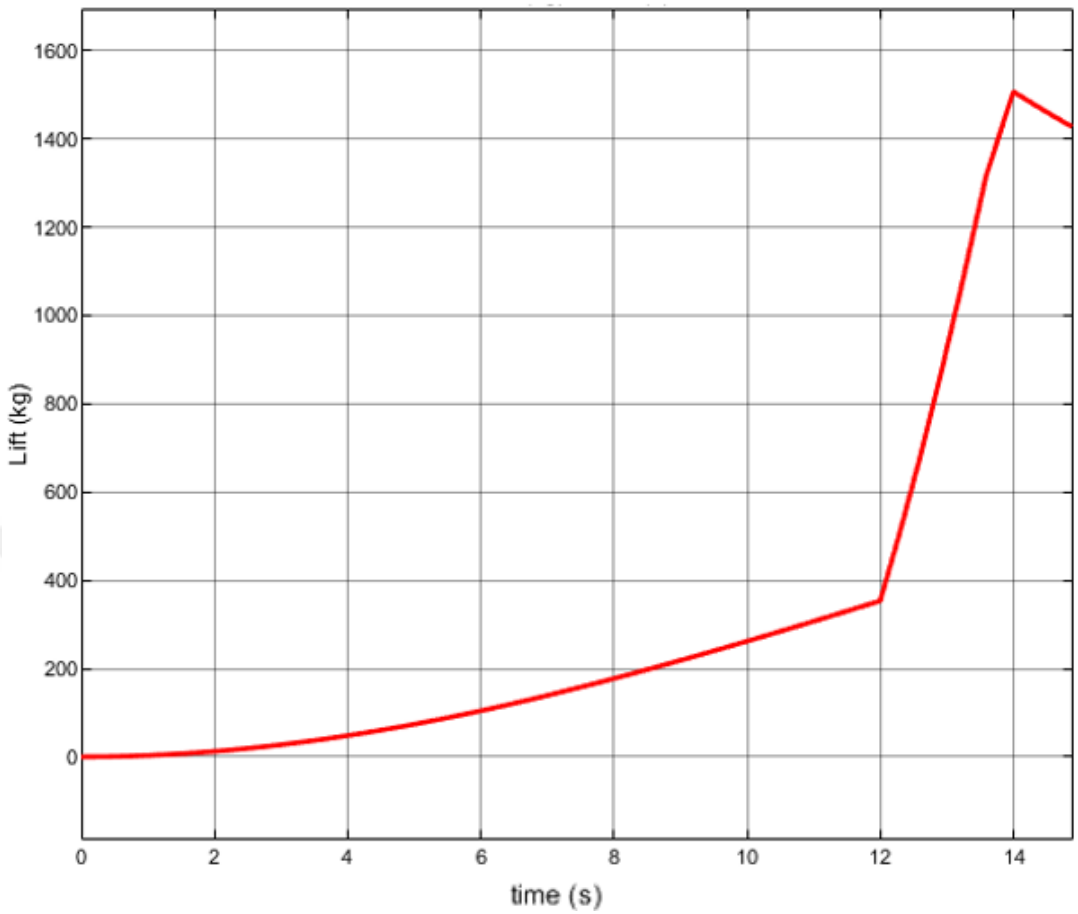

Figure 3.21 Lift force (Newton) - time(s)

Drag force increases as velocity of UAV increases in time up to the 13.5th second. After this point, it starts to decrease due to the decelerating effect of the sky jump ramp. The drag force - time graph can be examined in Figure 3.22.

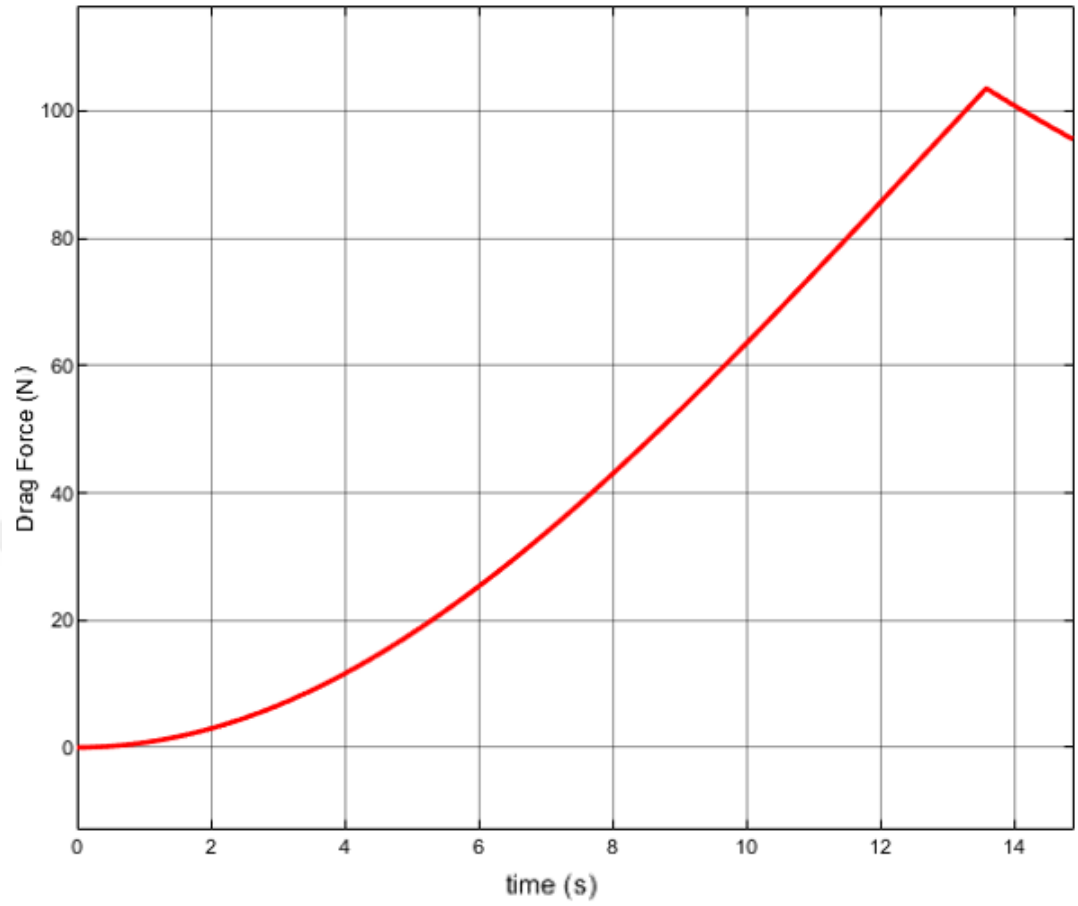

Figure 3.22 Drag force (Newton) – time(s)

Sky jump's slope leads to a change in the slowing force during the time as shown in Figure 3.23. The slowing force stays as zero up to the 13.5th second of take-off because the sky jump is on the last 30 meters of the runway, and the UAV reaches this point at the 13.5th second of take-off.

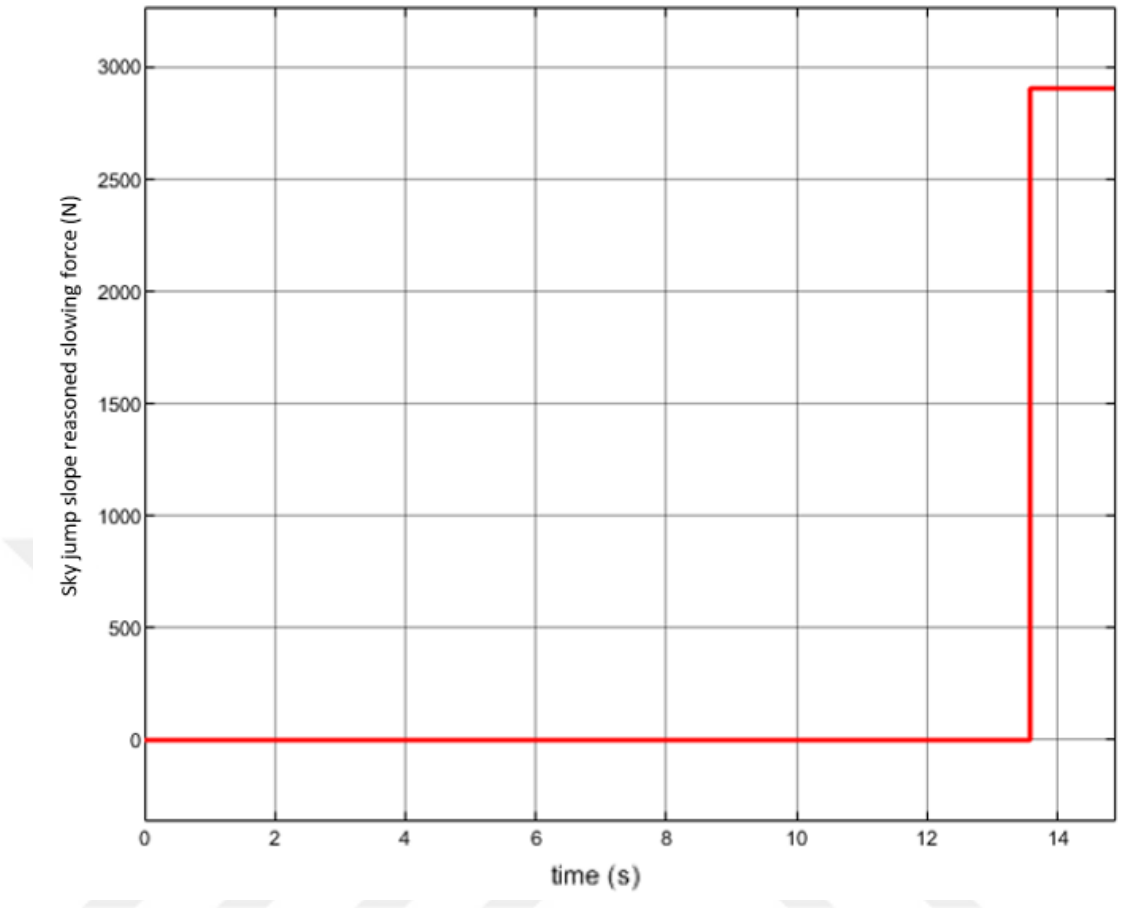

Figure 3.23 Sky jump slope reasoned slowing force (N) - time(s)

The lateral forces that act on the UAV are the thrust force that is produced by the engine and propeller, the friction force between the tire and the road, the drag force, and the slowing force due to sky jump ramp. The lateral resultant force change in time is presented in Figure 3.24. The resultant force is reduced during in the 0 - 13.5th second because the drag force increases parallel to an increase in UAV velocity in this time period. After the 13.5th second, the resultant force is reduced suddenly due to sky jump's decelerating effect.

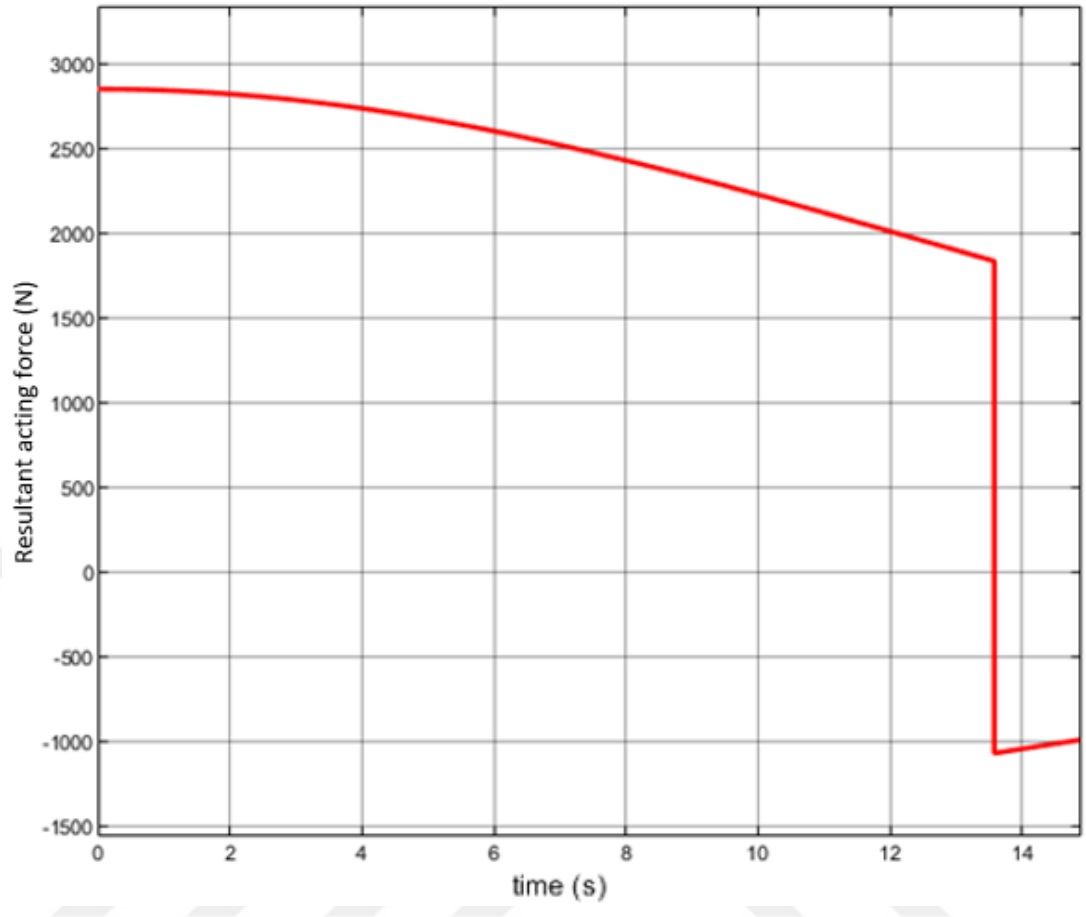

Figure 3.24 Resultant acting force (Newton) - time (s)

The aerial vehicle reaches the end of runway under the influence of resultant lateral force. The change in the velocity of the aerial, and indeed how sky jump reduces the velocity of UAV vehicle, is shown in Figure 3.25.

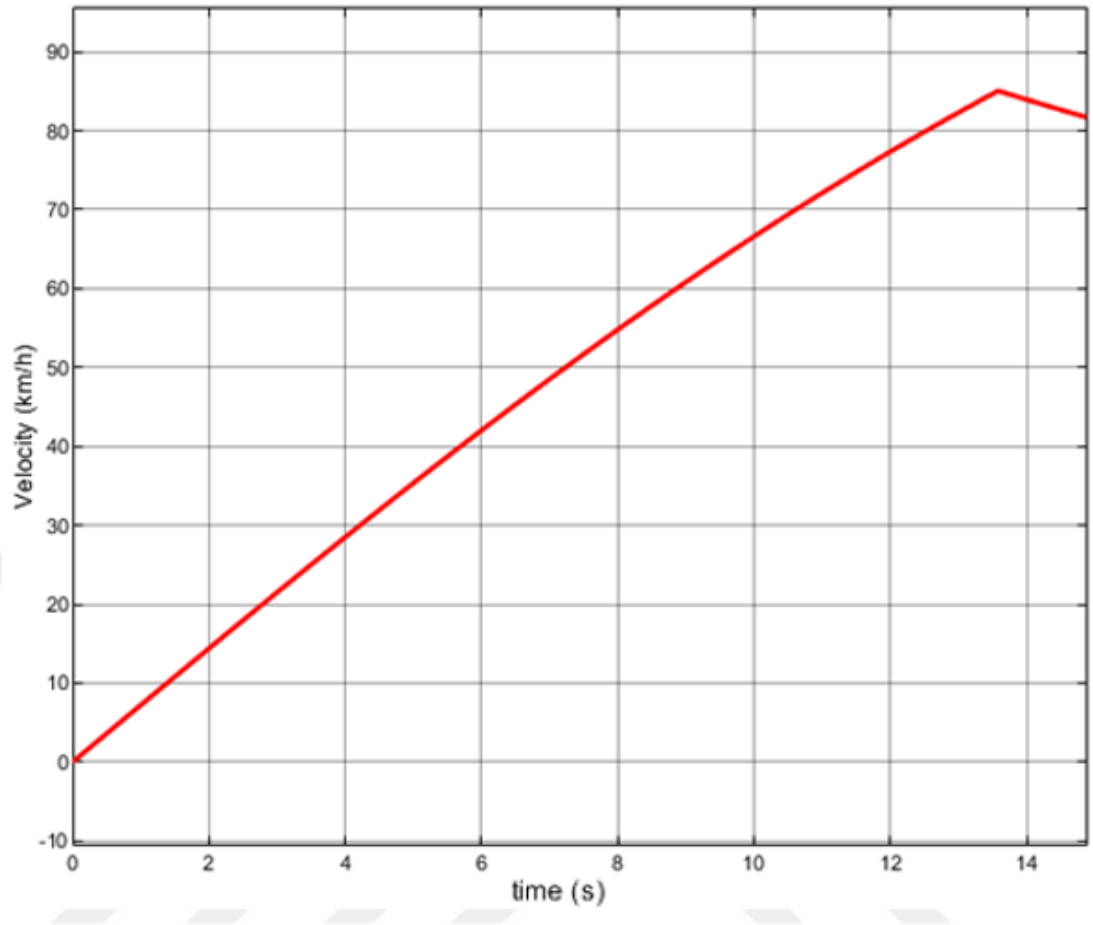

Figure 3.25 Velocity (km/h) - time(s)

Another important graph is position - time graph of the UAV, which is demonstrated in Figure 3.26. Here, the increase in velocity results in the parabolic increase in the position of the aerial vehicle.

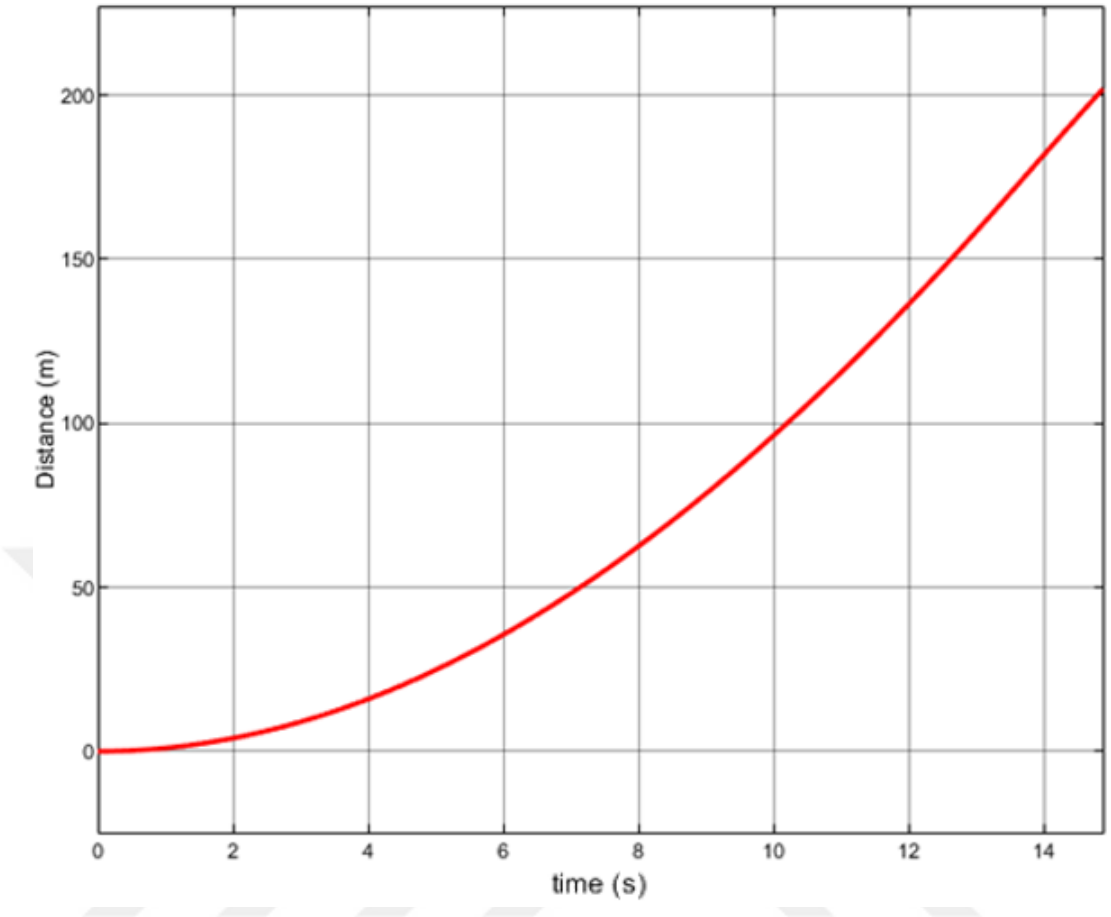

Figure 3.26 Distance (m) - time (s)

3.6 Take-off Case Study

In this case study, 3 and 10-degree incidence wing configurations were examined by using a proposed mathematical model. Take off distance, total produced lift, and velocity comparisons are plotted for each configuration. All the parameters are kept the same in the two configurations except the incidence angle of wings. As it can be seen in Figure 3.27, the time required to reach 1425 kg lift for a 3-degree configuration is calculated as 34 seconds**.**

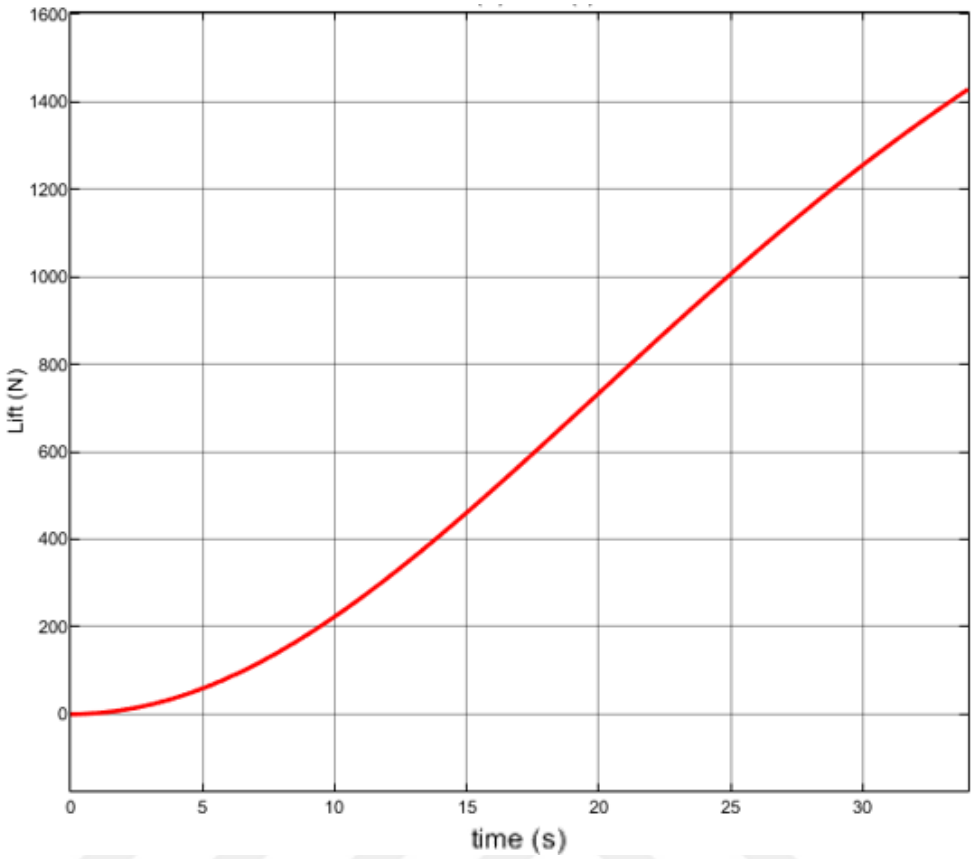

Figure 3.27 Lift (N) - time (s) graph for 3-degree incidence configuration

Also, the time required to reach 1425 kg lift for the 10-degree configuration is calculated as 20.1 seconds as seen in Figure 3.28.

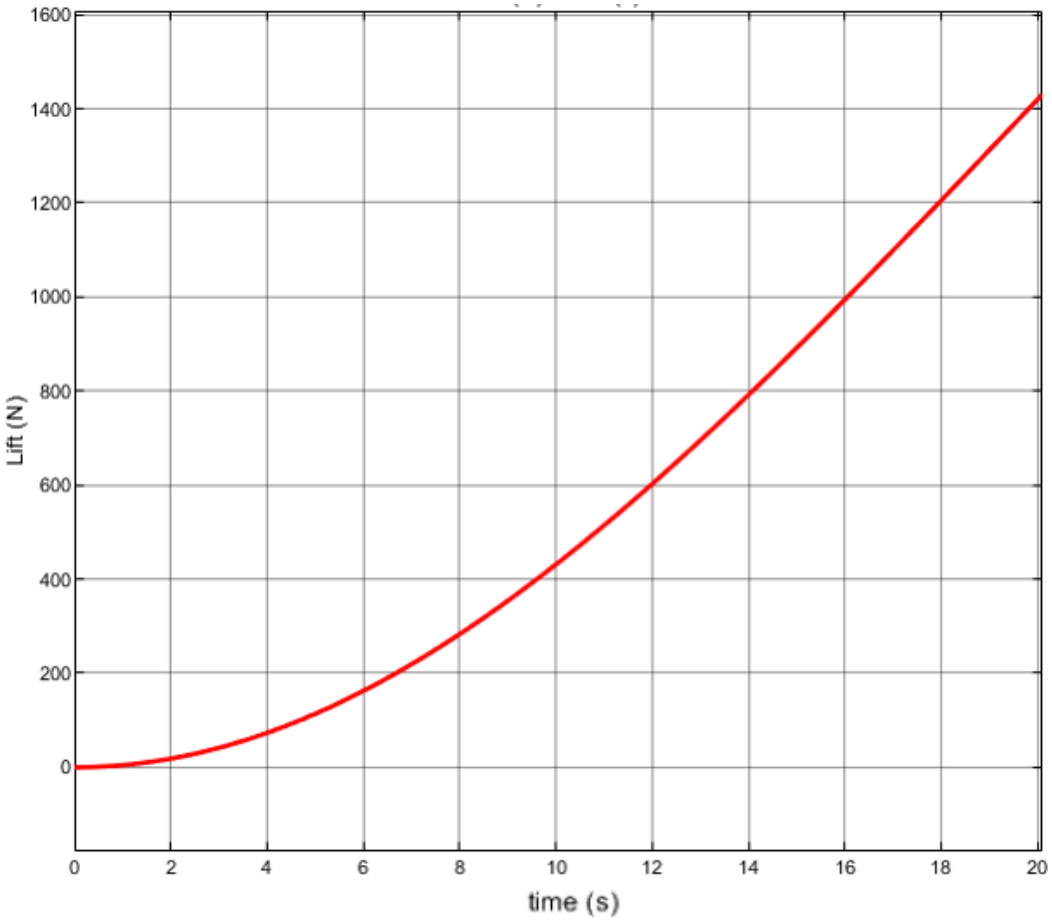

Figure 3.28 Lift (N) - time (s) graph for 10-degree incidence configuration

Figure 3.27 and 3.28 show that a 7-degree increase in the incidence angle of wing causes 40% reduction in the take-off time. Another parameter which is compared in this case study is the position time graphs for the configurations. The position time graph for the 3-degree configuration can be examined in Figure 3.29.

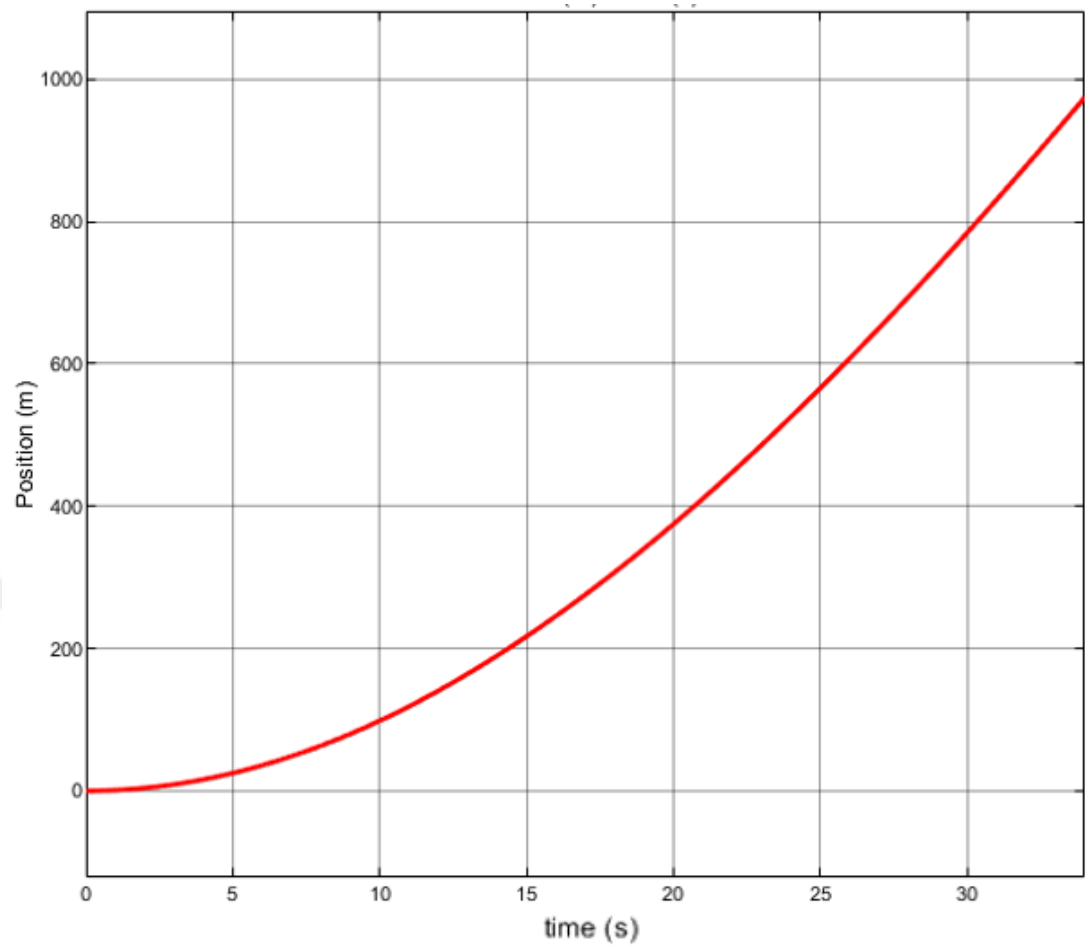

Figure 3.29 Position (m) - time (s) graph for 3-degree incidence configuration

It is understood from Figure 3.29, the aerial vehicle travelled about 950 m in 34 seconds in the 3-degree configuration. The travelled distance is reduced by up to 375 m in the 10-degree configuration, which can be seen in Figure 3.30.

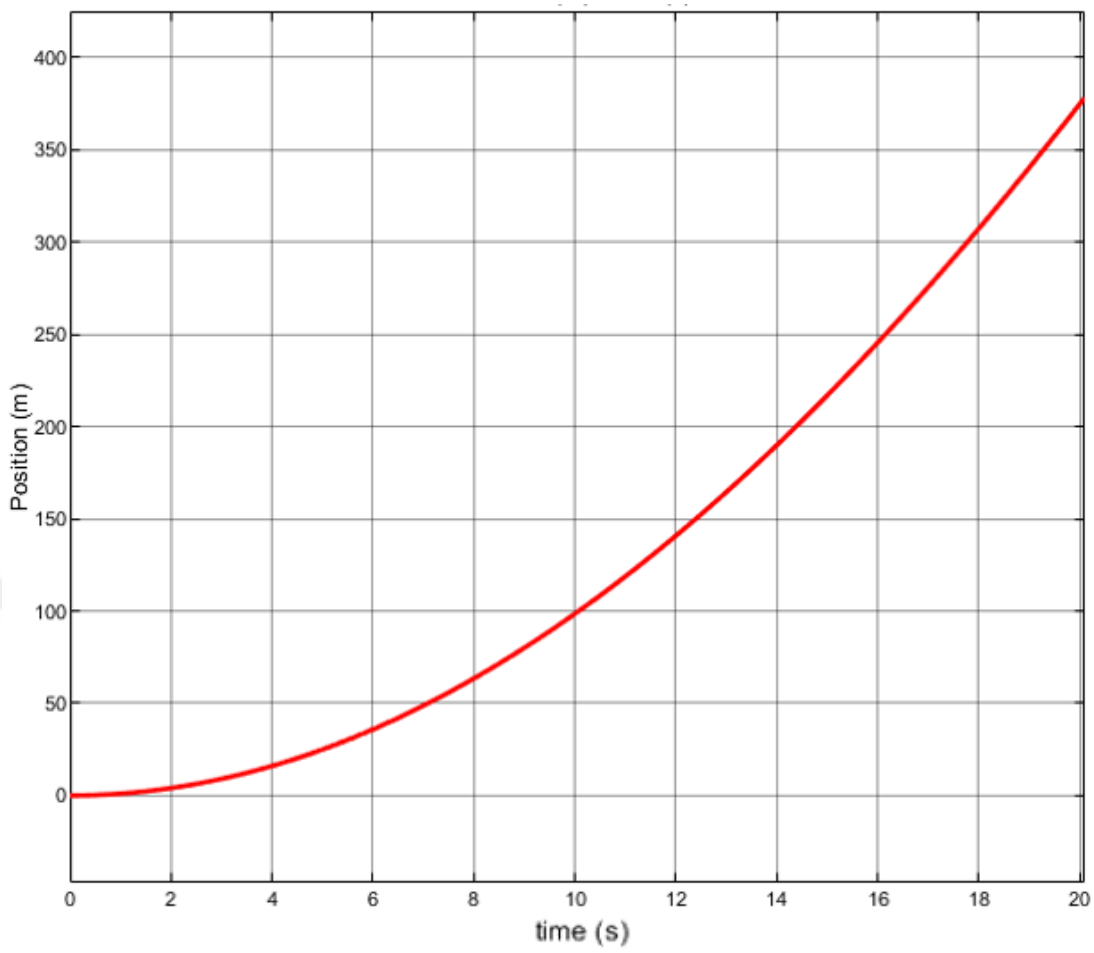

Figure 3.30 Position (m) - time (s) graph for 10-degree incidence configuration

It is presented, in Figure 3.29 and 3.30, respectively, that the runway distance is reduced by nearly 60% by a 7-degree increase in incidence angle of wing. The shortening of runway distance to this extent is noteworthy given that the only reason for this phenomenon is a 7-degree increase in incidence angle of wing. Another parameter which is compared is velocity - time graphs. Velocity - time graph for a 3-degree configuration is presented in Figure 3.31.

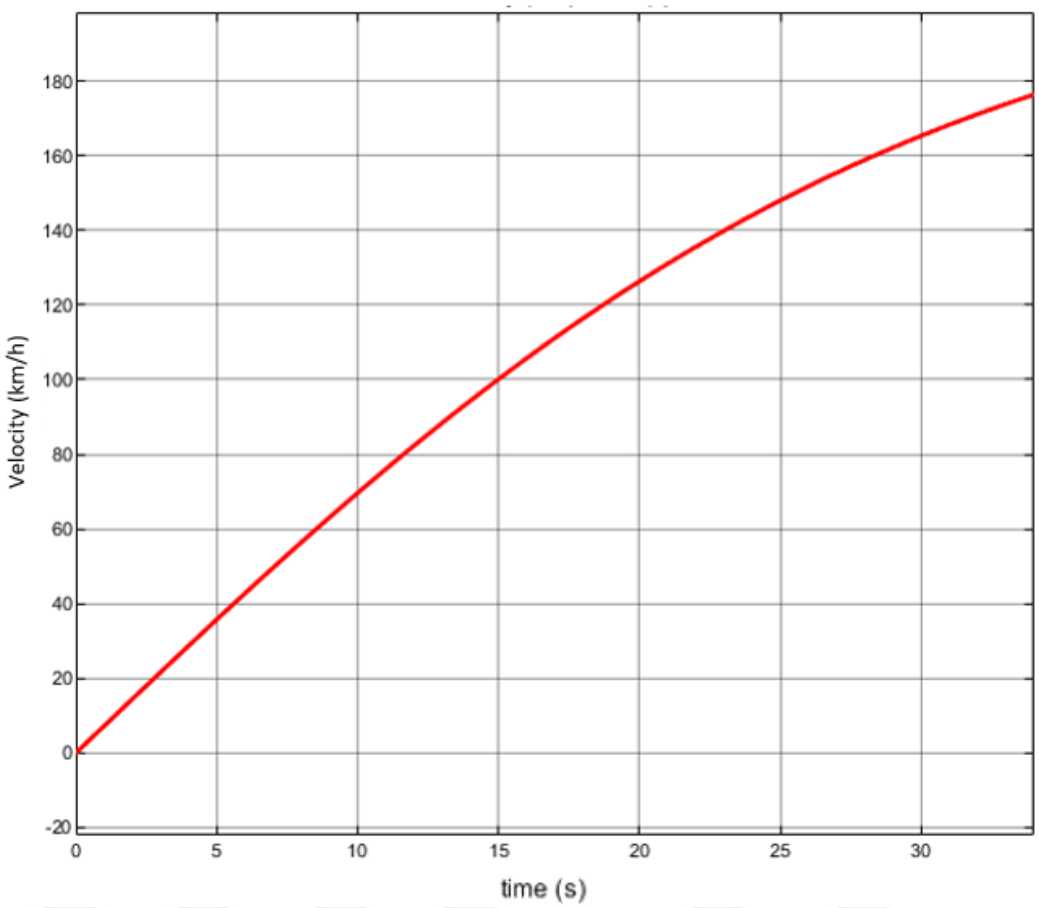

Figure 3.31 Velocity (km/h) - time (s) graph for 3-degree incidence configuration

As it is seen in Figure 3.31, the velocity of aerial vehicle reaches km/h at the end of the 34th second. Velocity time graph for a 10-degree configuration can be seen in Figure 3.32.

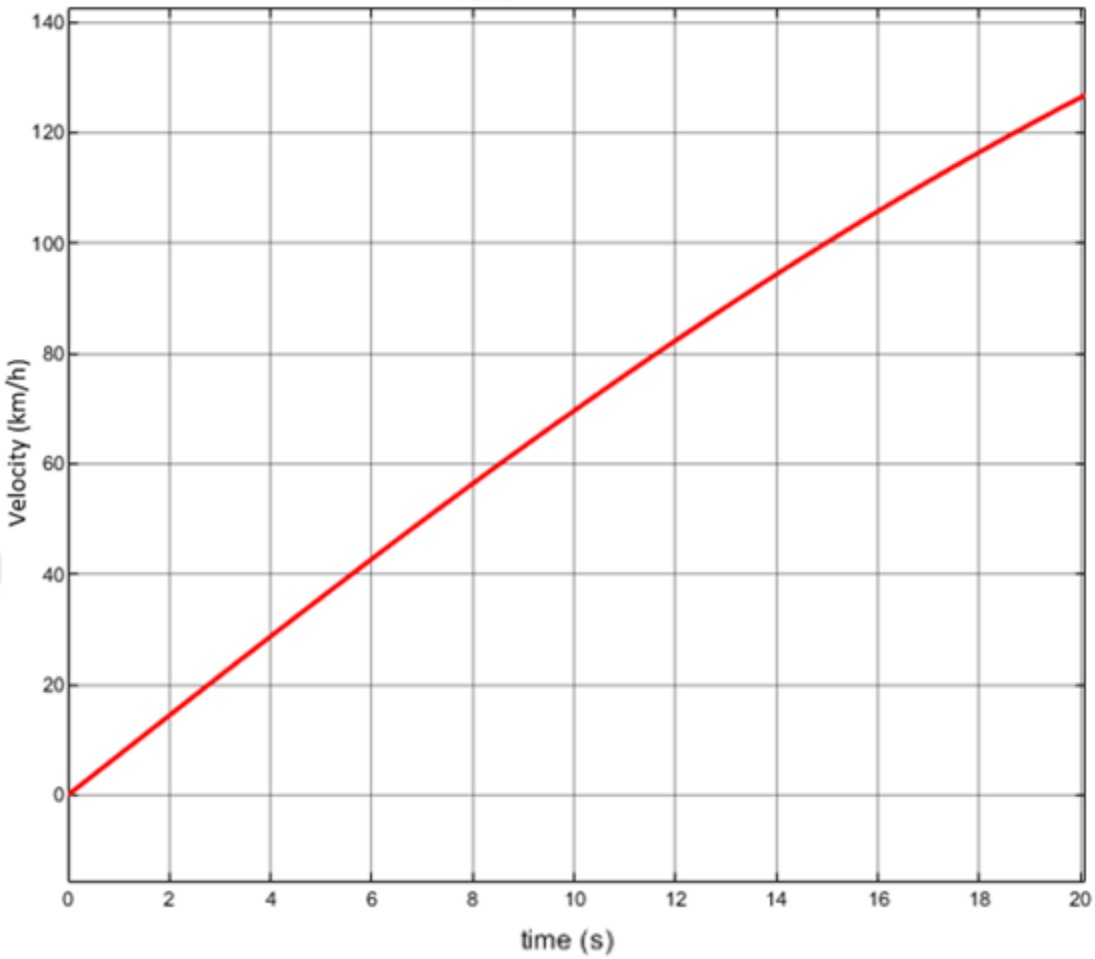

Figure 3.32 Velocity (m) - time (s) graph for 3-degree incidence configuration

As it is presented in Figure 3.32, the 10-degree configuration reaches 125 km/h velocity at the end of 20.1th seconds. It indicates that the 10-degree configuration can take off with lower velocity than the 3-degree configuration by 30%. This validates the thesis's main argument.

CHAPTER 4

COMPUTATIONAL FLUID DYNAMICS ANALYSIS

Computational fluid dynamics analysis was run for the wing. The COMSOL was preferred to perform CFD simulation. The mesh structure constructed has 5256247 elements and 8564257 grids. As presented in Figure 4.1, denser mesh was generated around the airfoil as 2D mesh to increase the accuracy of the model.

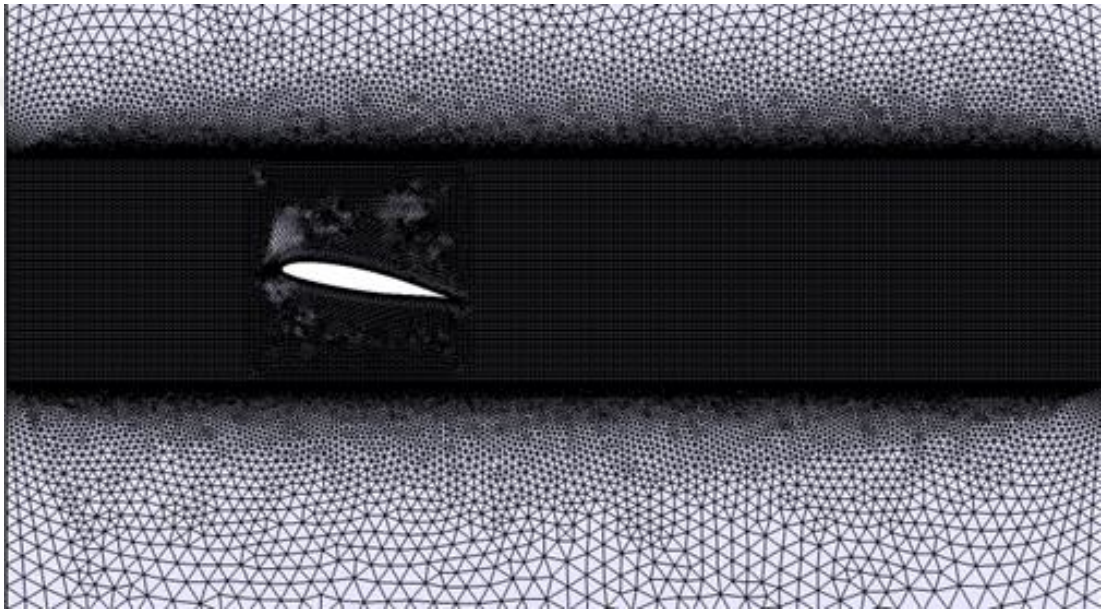

Figure 4.1 Meshed structure

The boundary layer region was meshed with boundary layer meshes which are used to accurately capture the drag forces.

In CFD analysis, wing was rotated from -10 to 14-degree, and the dataset required to create Cl-alpha graph was obtained. The air density was taken as 1.225 kg/m^3 and the air velocity was entered as 100 km/h for the mathematical model.

4.1 Velocity Contours

As a result of the CFD analysis, velocity contours are extracted for each angle of attack. In this context, velocity contours between -10 and +14 degree are presented in the following figures. The counter unit is selected as m/s.

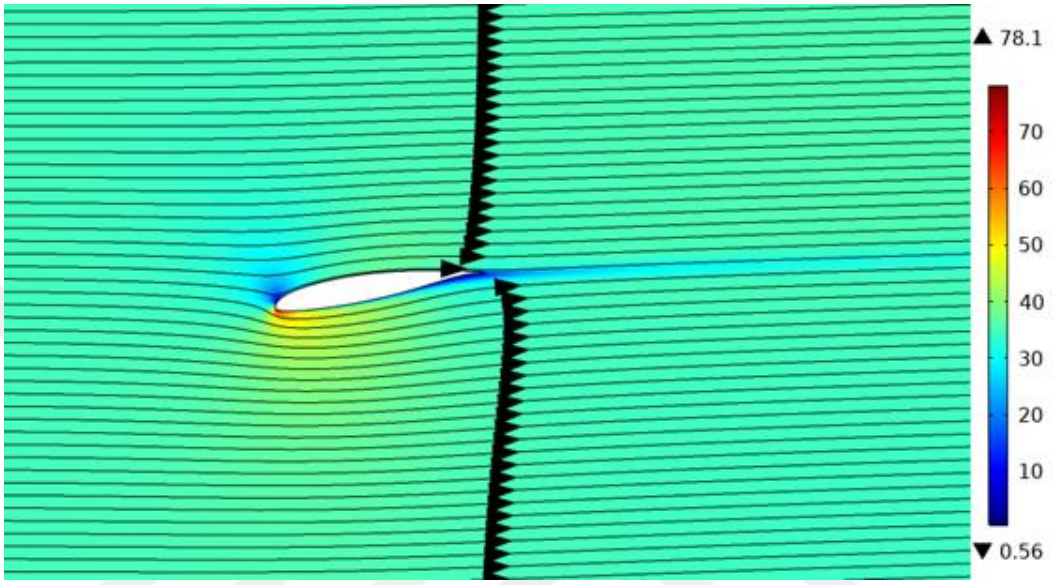

Figure 4.1 The -10-degree velocity contours

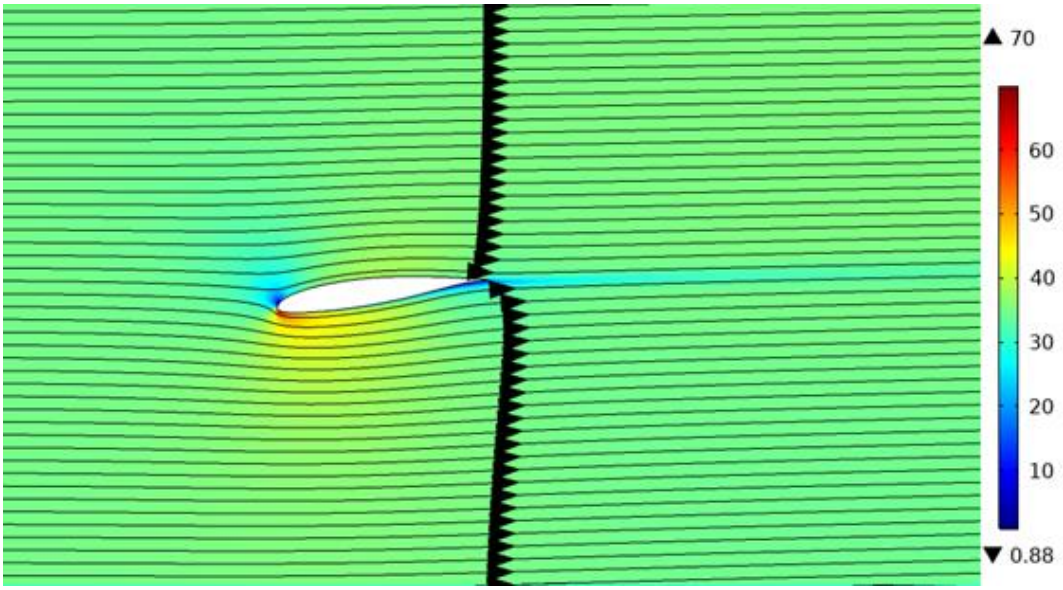

Figure 4.2 The -8-degree velocity contours

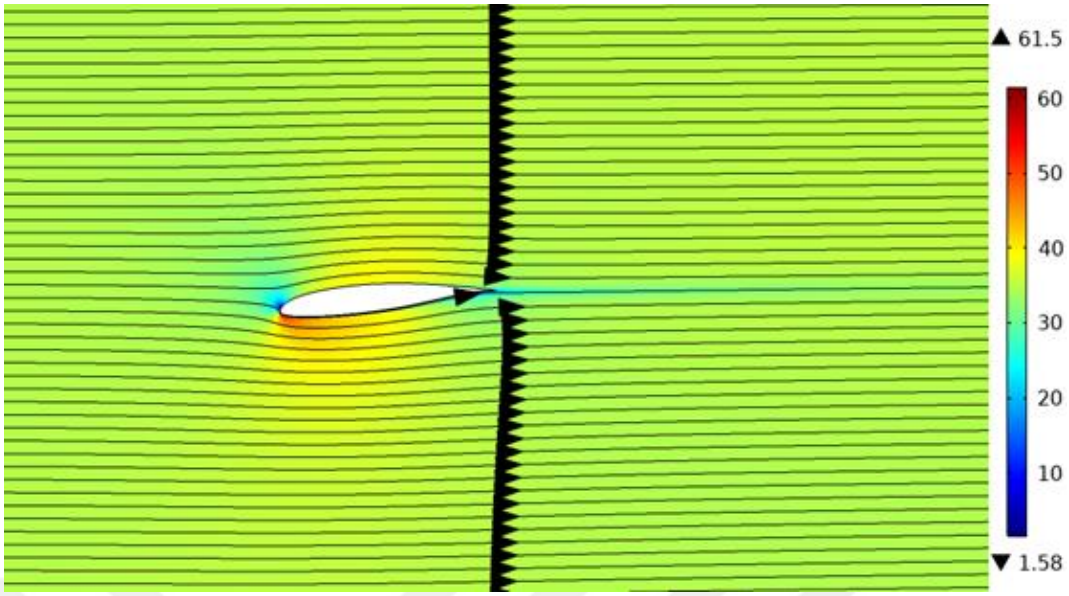

Figure 4.3 The -6-degree velocity contours

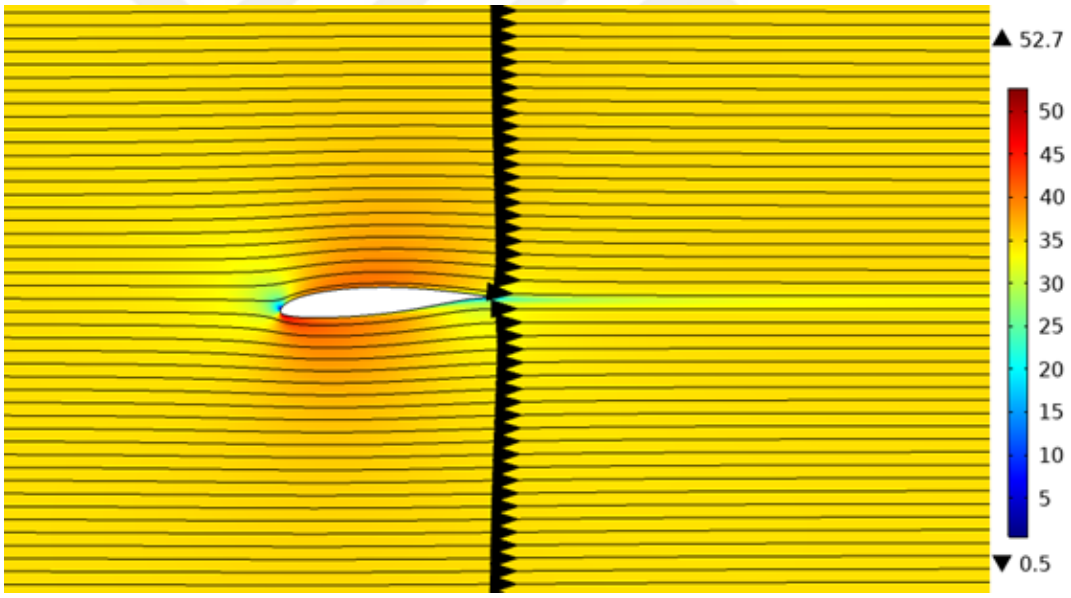

Figure 4.4 The -4-degree velocity contours

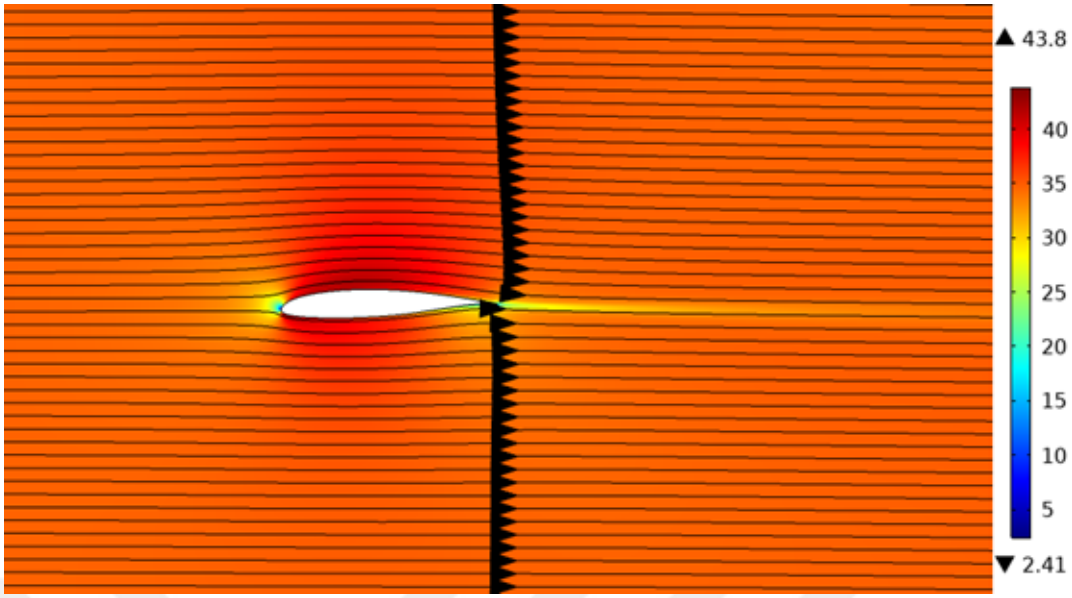

Figure 4.5 The -2-degree velocity contours

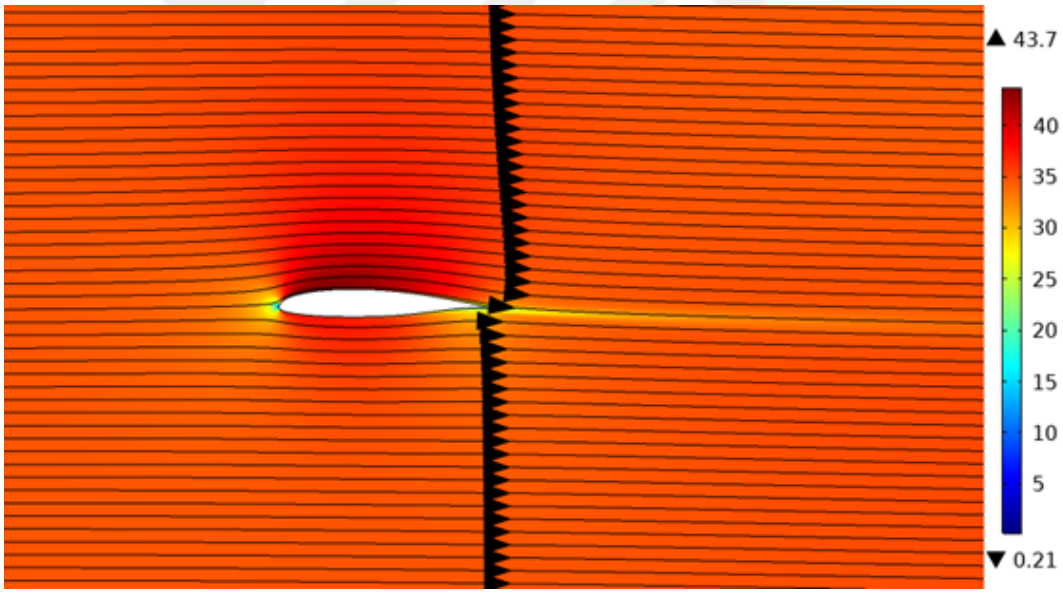

Figure 4.6 The 0-degree velocity contours

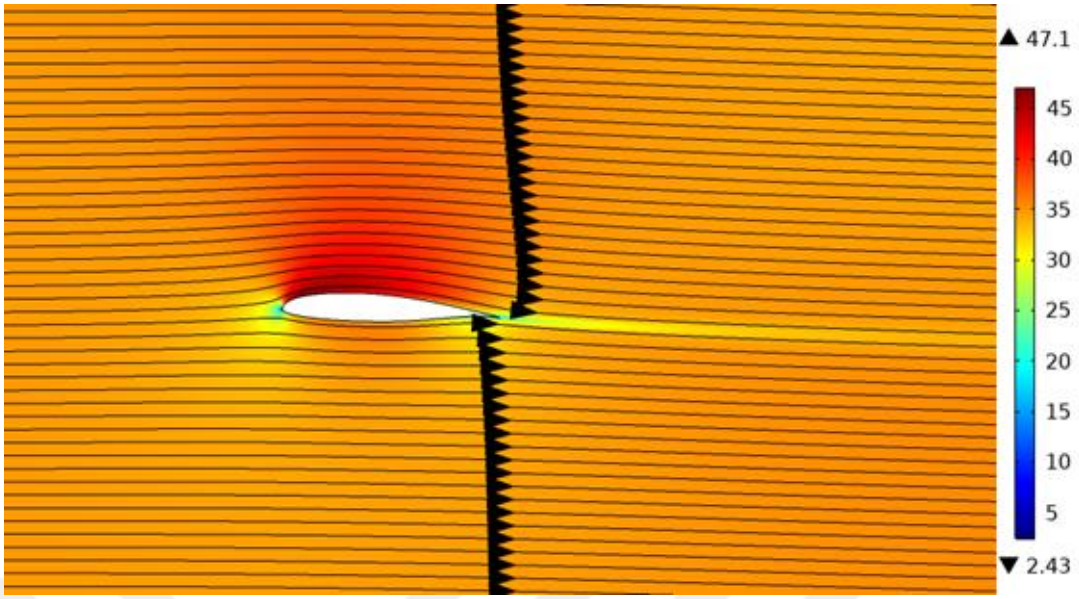

Figure 4.7 The 2-degree velocity contours

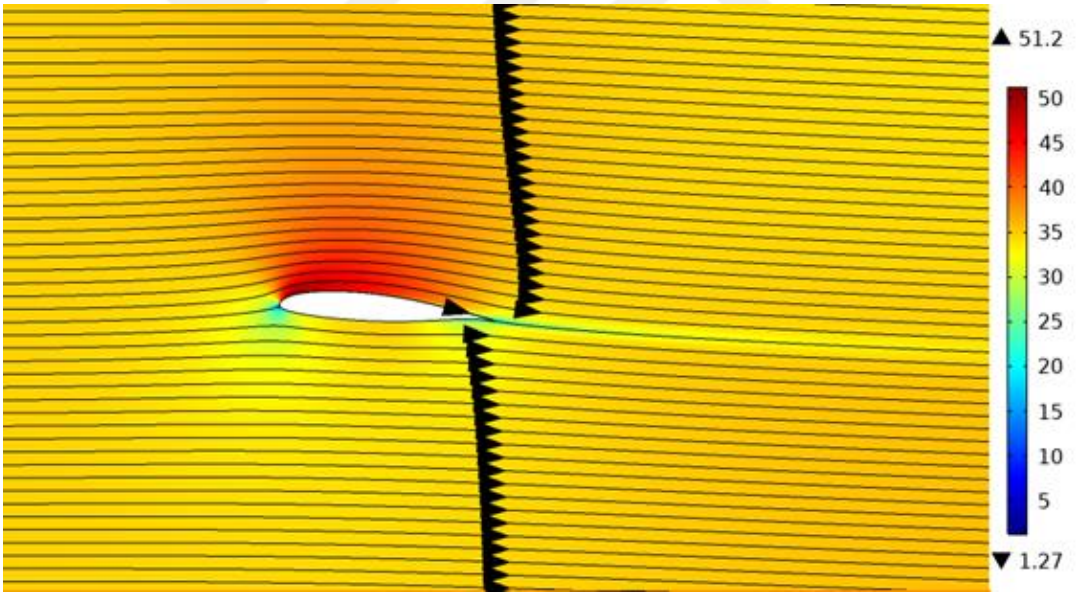

Figure 4.8 The 4-degree velocity contours

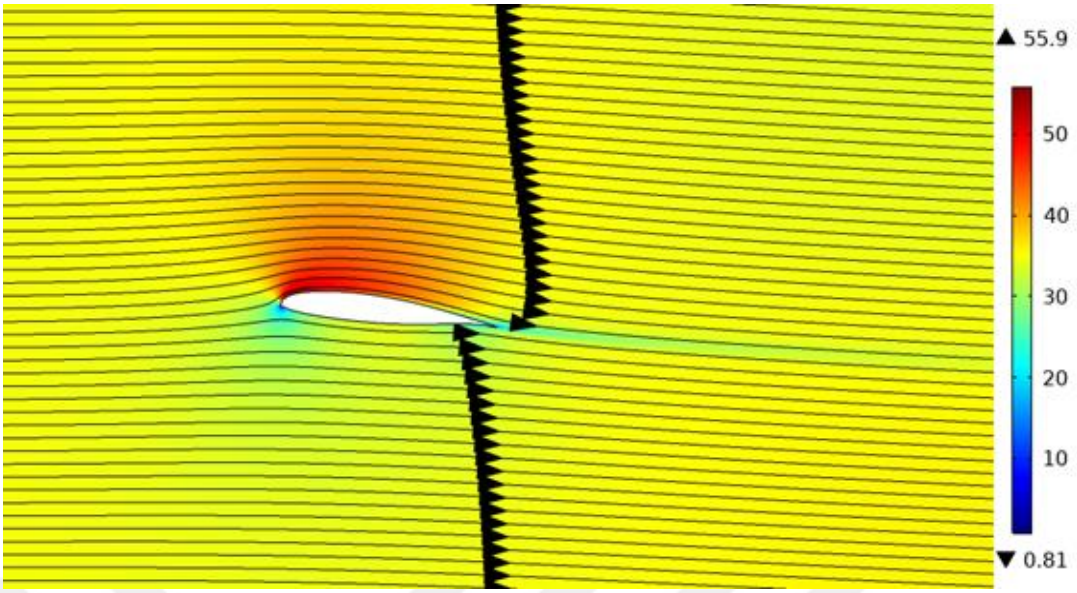

Figure 4.9 The 6-degree velocity contours

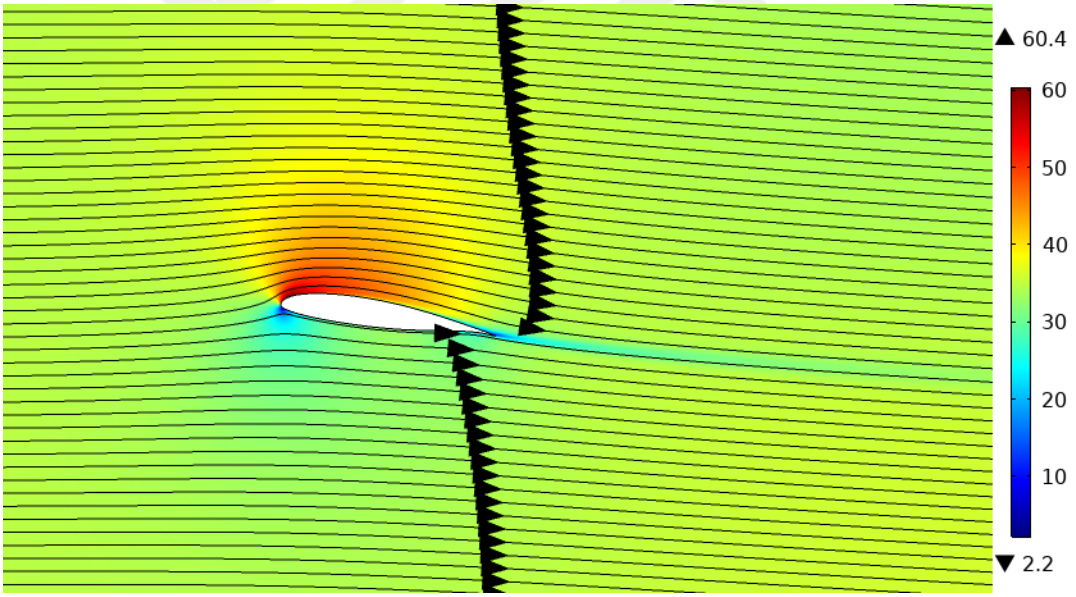

Figure 4.10 The 8-degree velocity contours

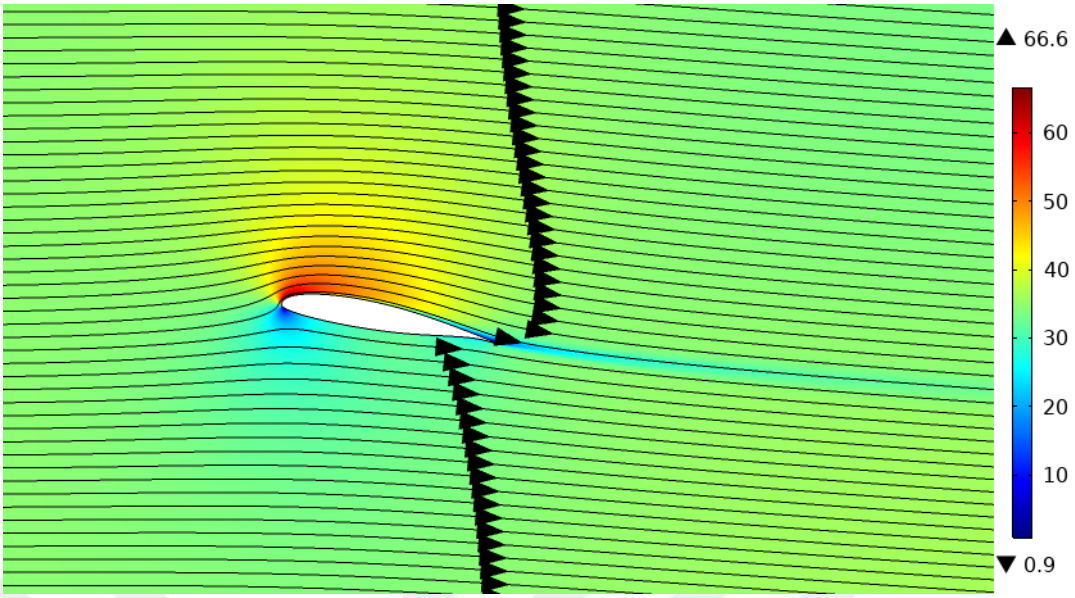

Figure 4.11 The 10-degree velocity contours

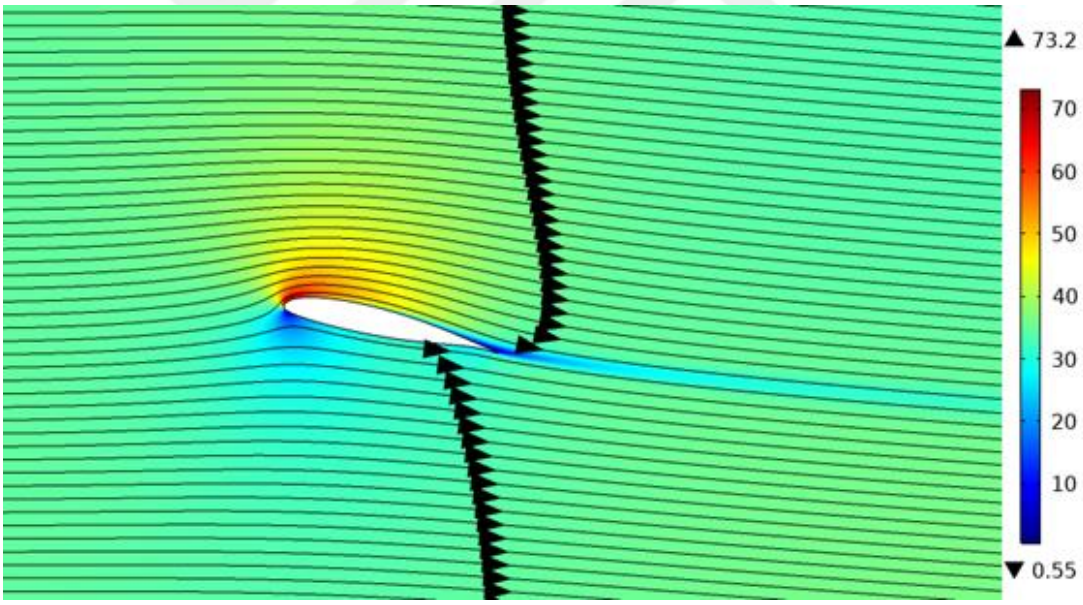

Figure 4.12 The 12-degree velocity contours

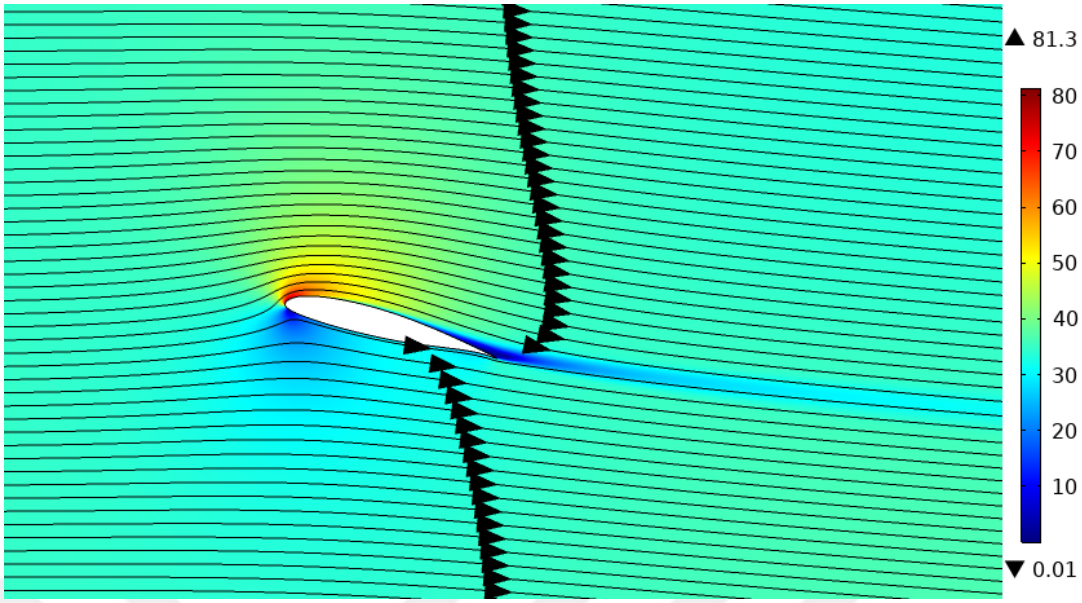

Figure 4.13 The 14-degree velocity contours

4.2 Pressure Contours

As a result of the CFD analysis, pressure contours were extracted for each angle of attack. In this context pressure contours and pressure boundary contours between the -10 and +14-degree are presented in Figure 4.14 to Figure 4.39. The contour unit is selected as Pascal.

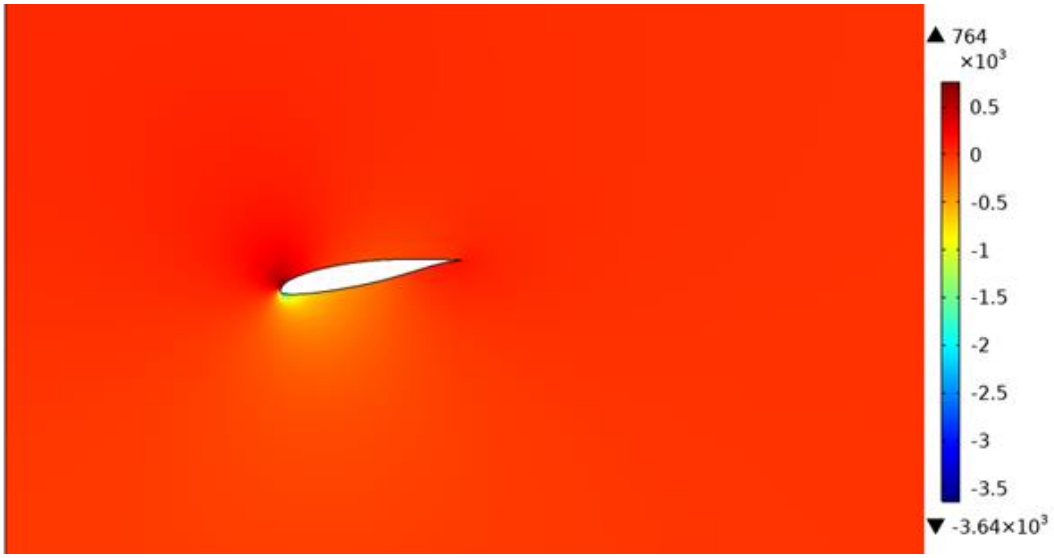

Figure 4.14 The -10-degree pressure contours

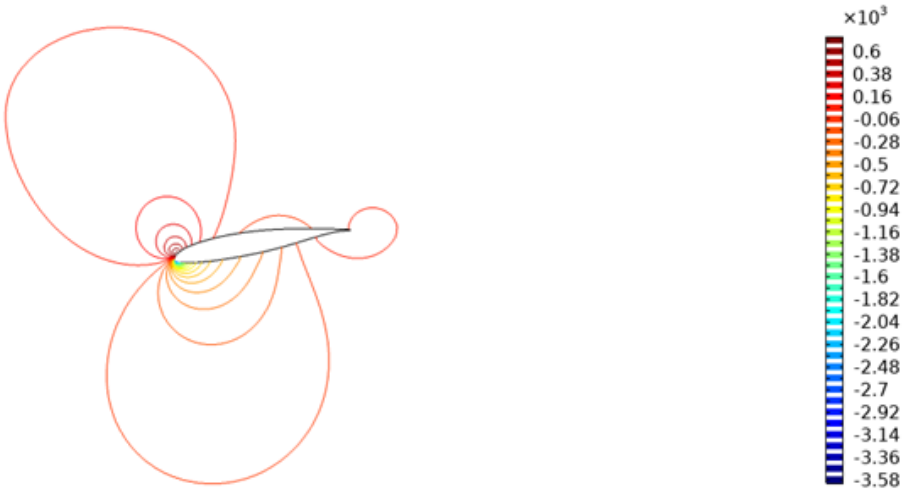

Figure 4.15 The -10-degree pressure boarders

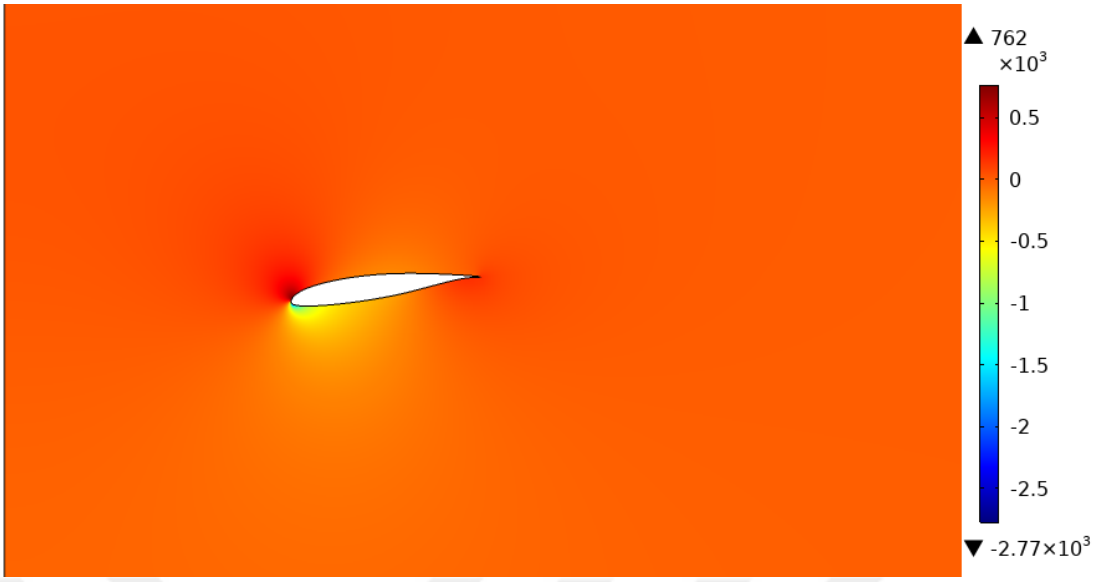

Figure 4.16 The -8-degree pressure contours

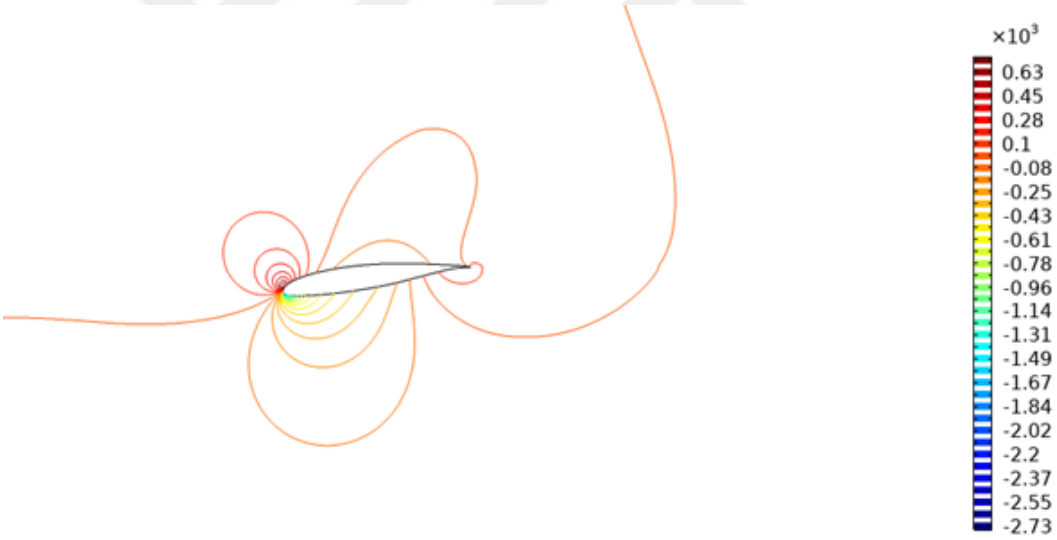

Figure 4.17 The -8-degree pressure boarders

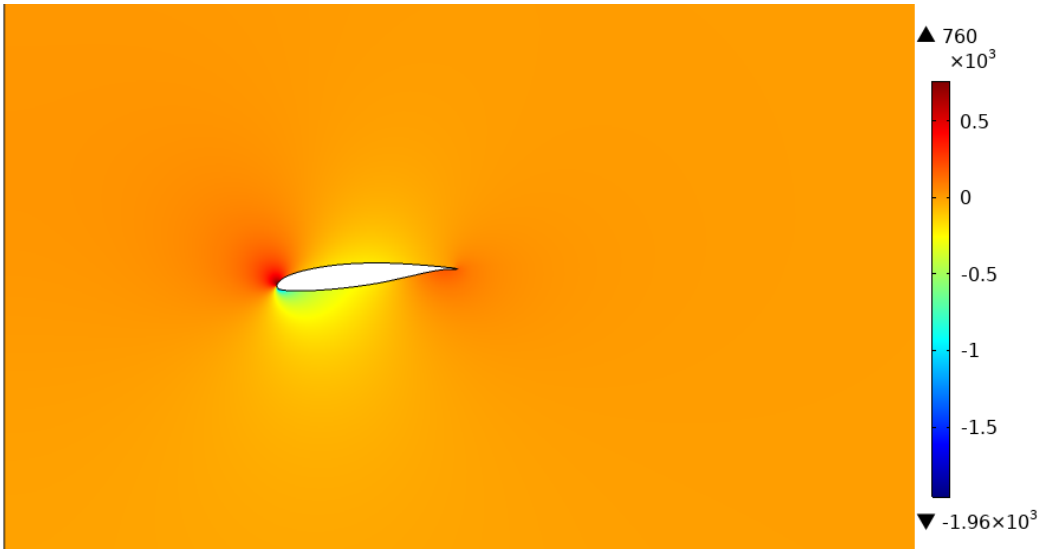

Figure 4.18 The -6-degree pressure contours

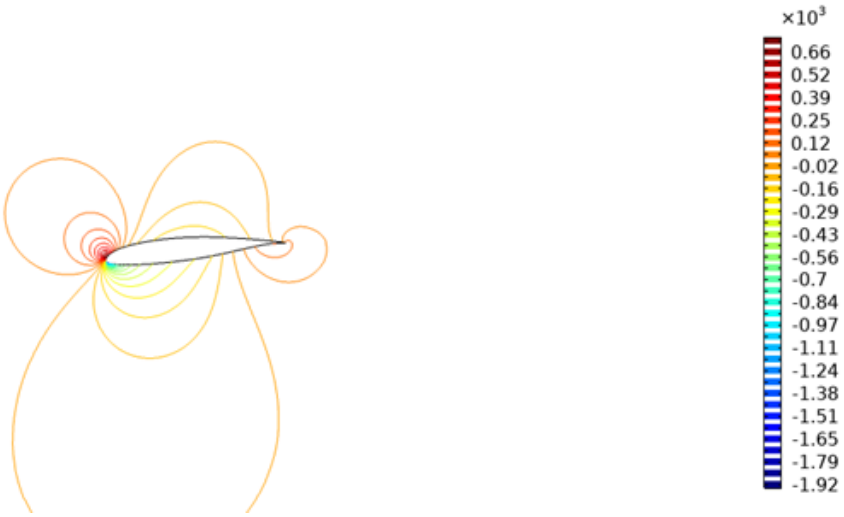

Figure 4.19 The -6-degree pressure boarders

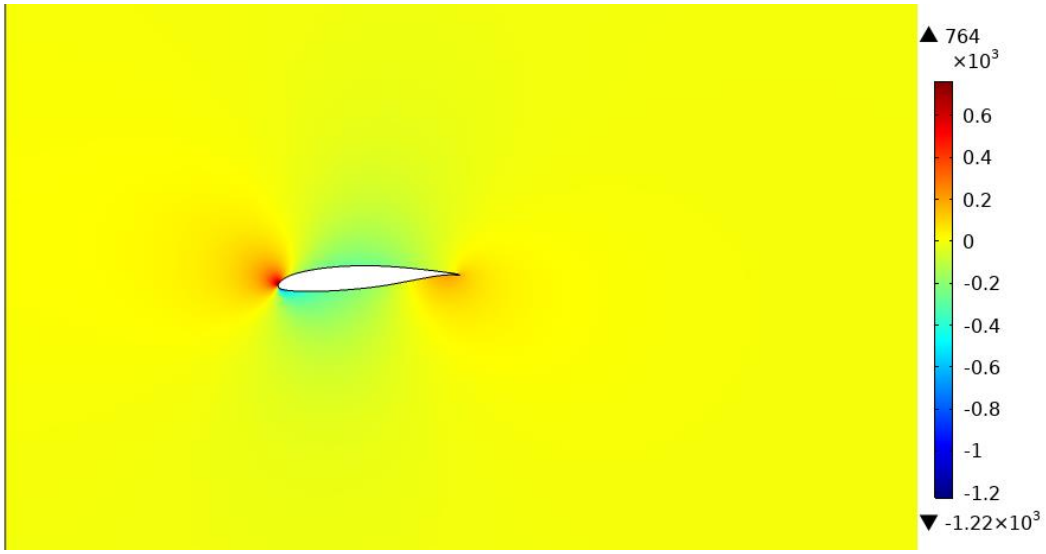

Figure 4.20 The -4-degree pressure contours

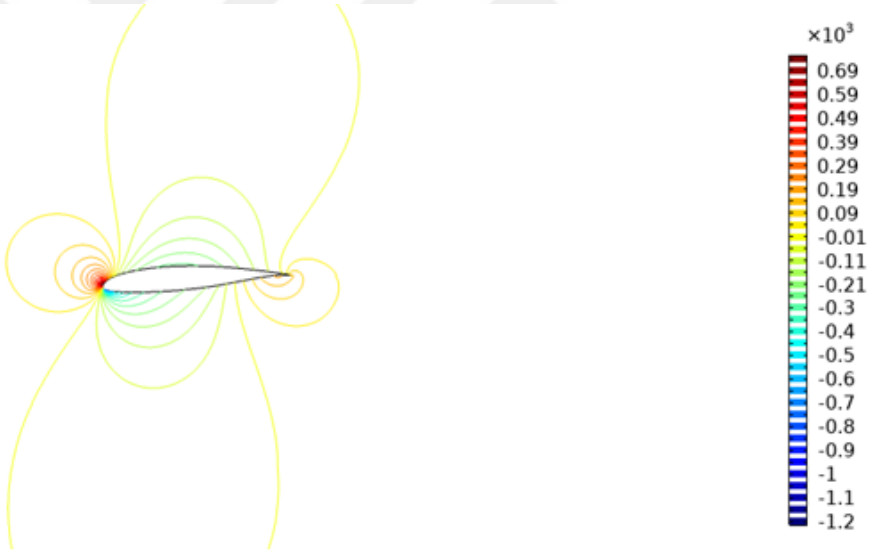

Figure 4.21 The -4-degree pressure boarders

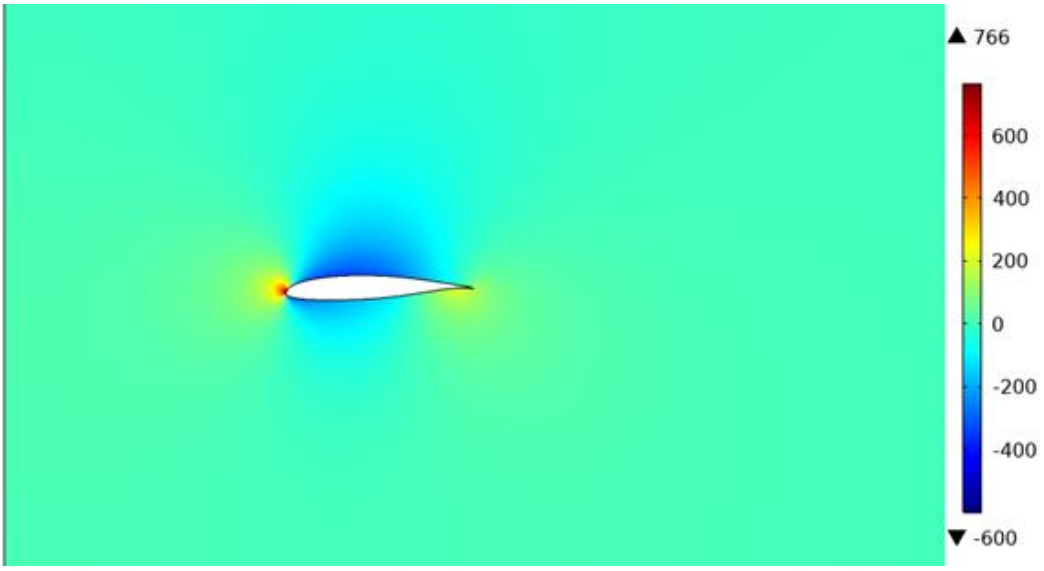

Figure 4.22 The -2-degree pressure contours

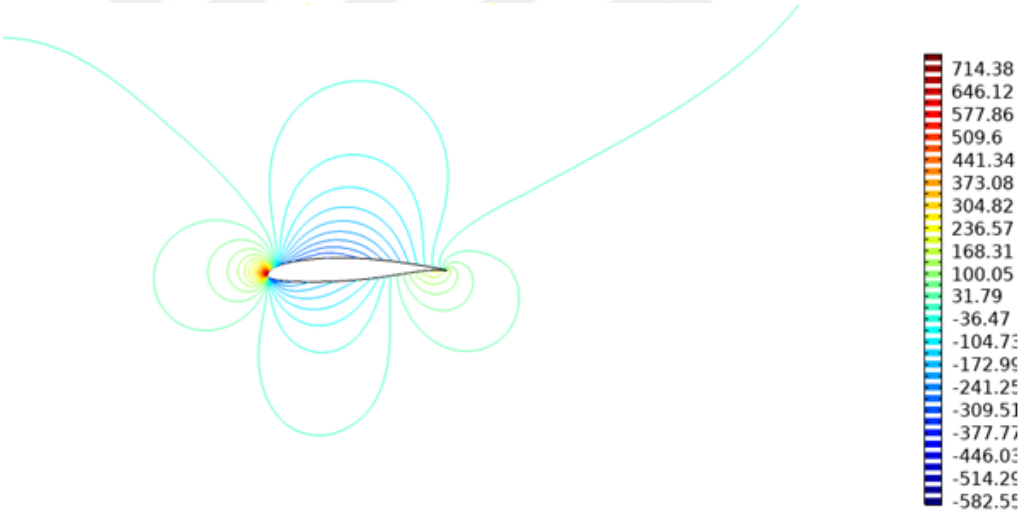

Figure 4.23 The -2-degree pressure boarders

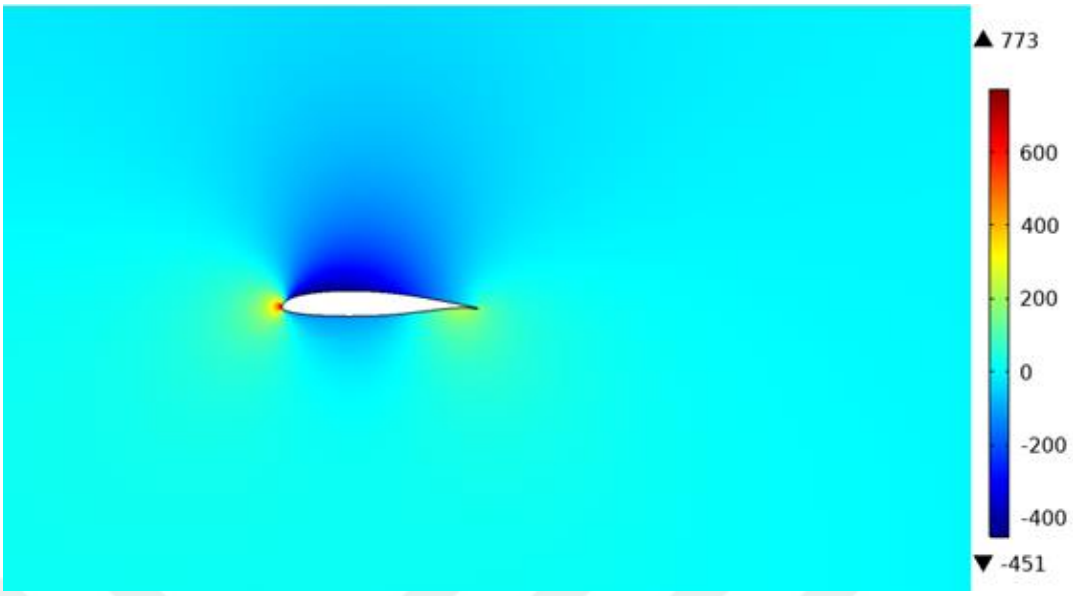

Figure 4.24 The 0-degree pressure contours

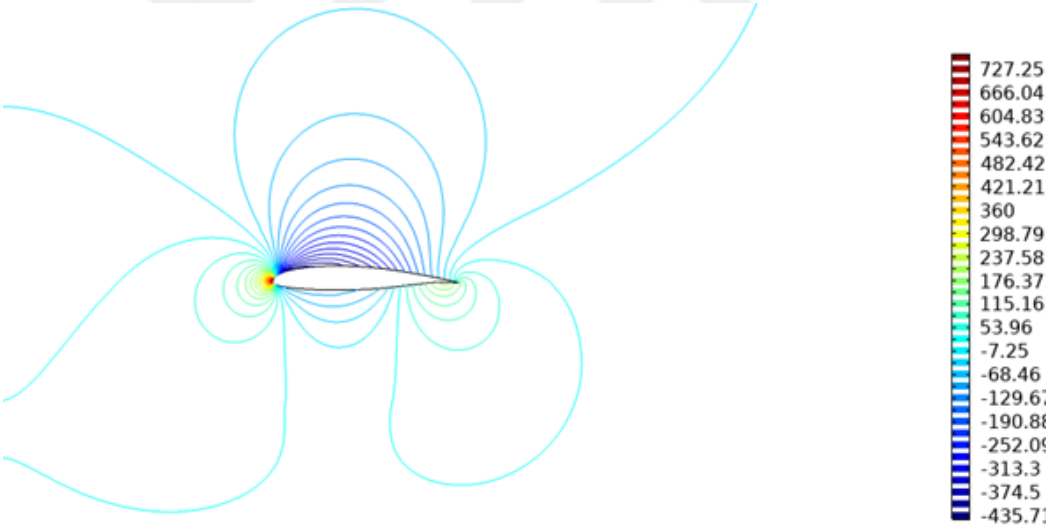

Figure 4.25 The 0-degree pressure boarders

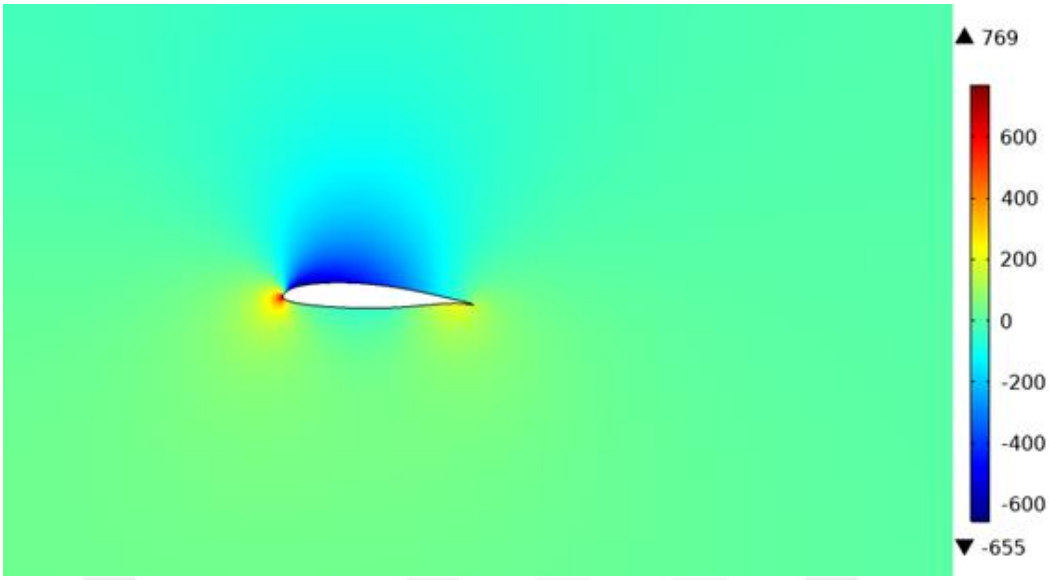

Figure 4.26 The 2-degree pressure contours

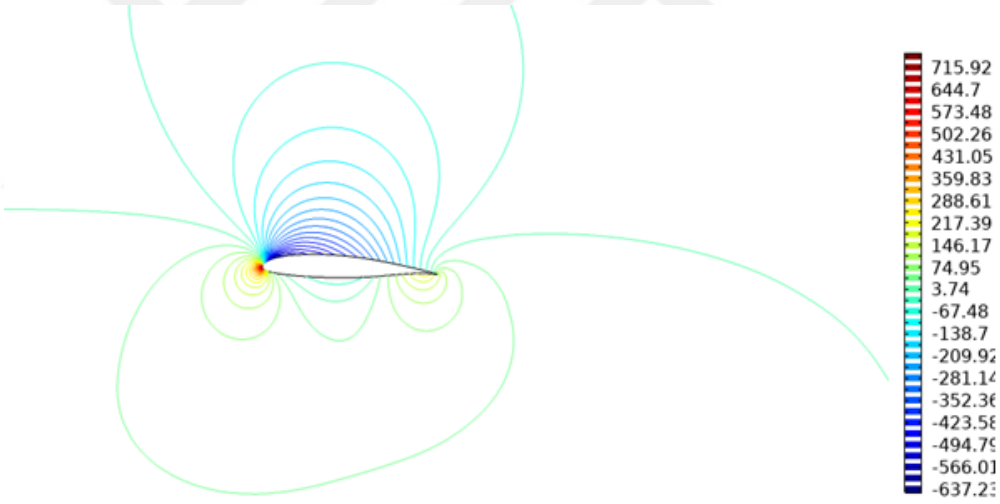

Figure 4.27 The 2-degree pressure boarders

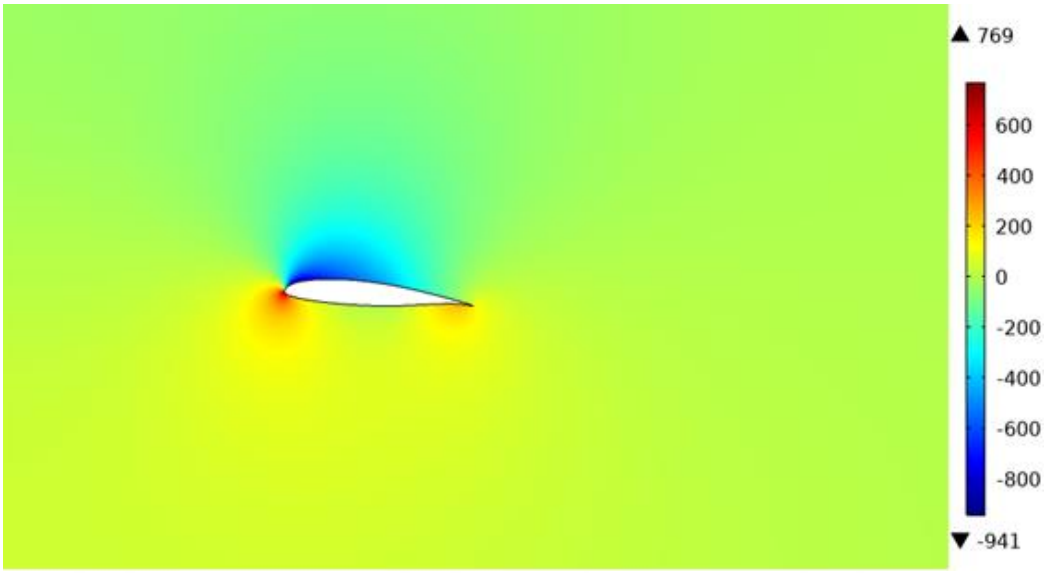

Figure 4.28 The 4-degree pressure contours

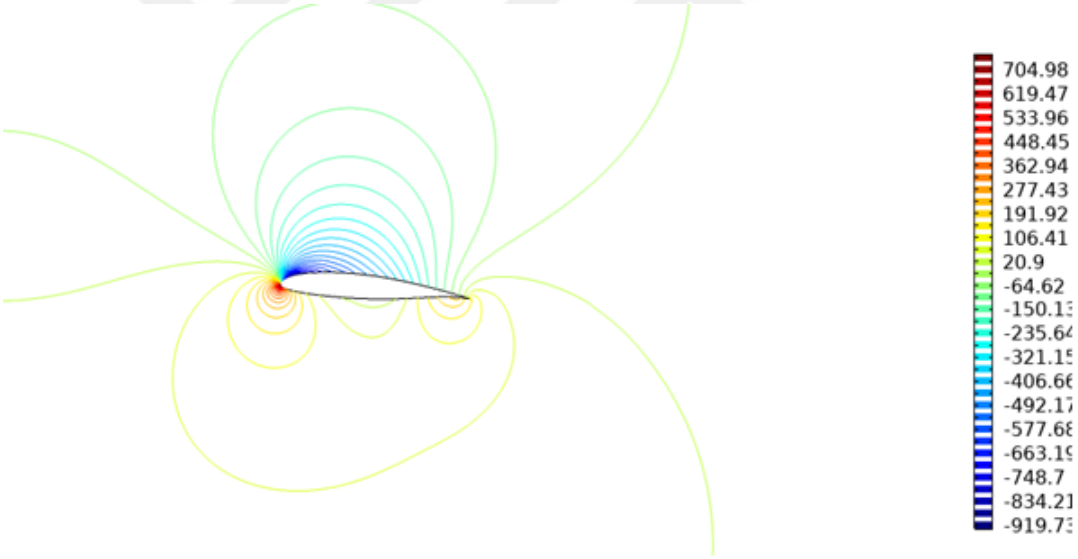

Figure 4.29 The 4-degree pressure boarders

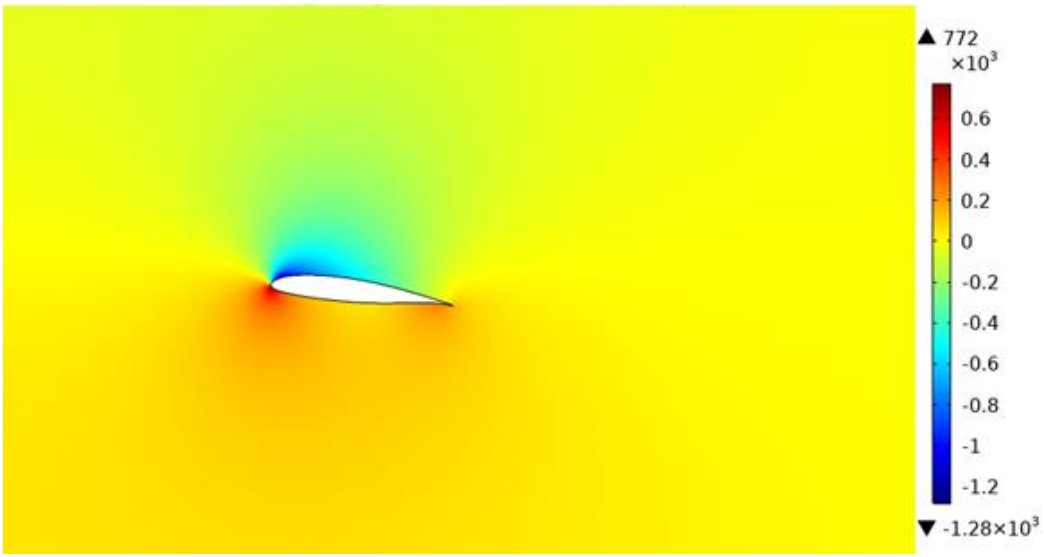

Figure 4.30 The 6-degree pressure contours

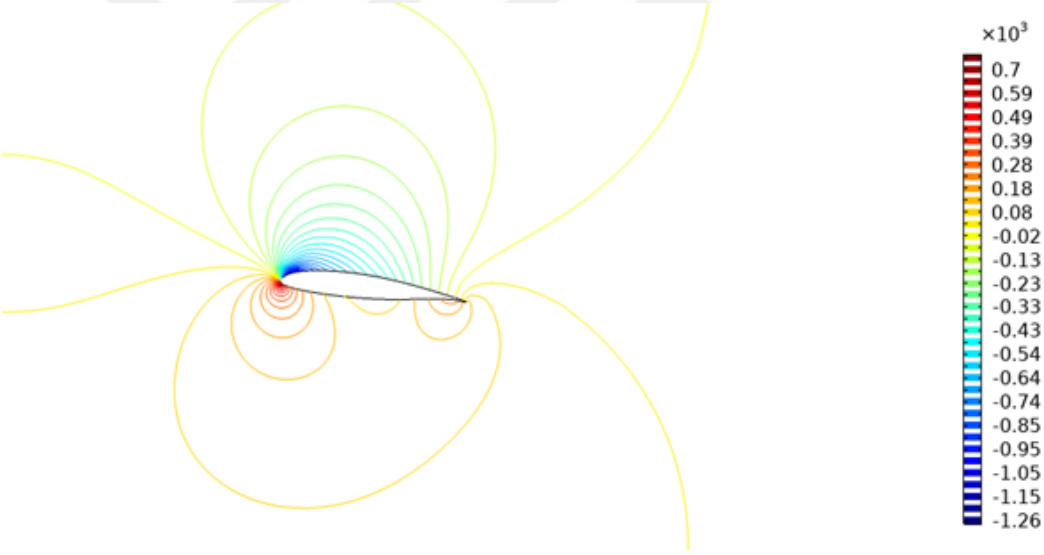

Figure 4.31 The 6-degree pressure boarders

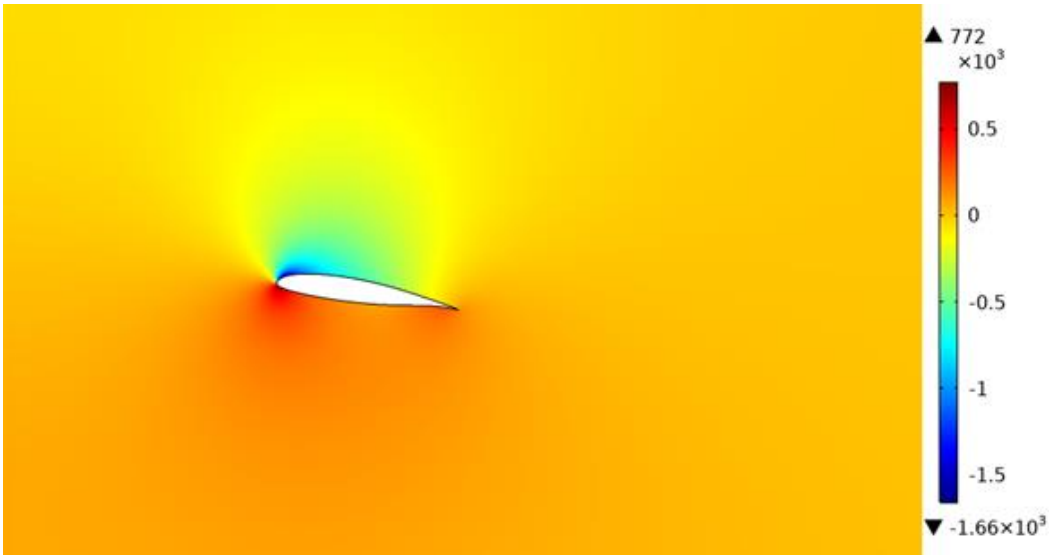

Figure 4.32 The 8-degree pressure contours

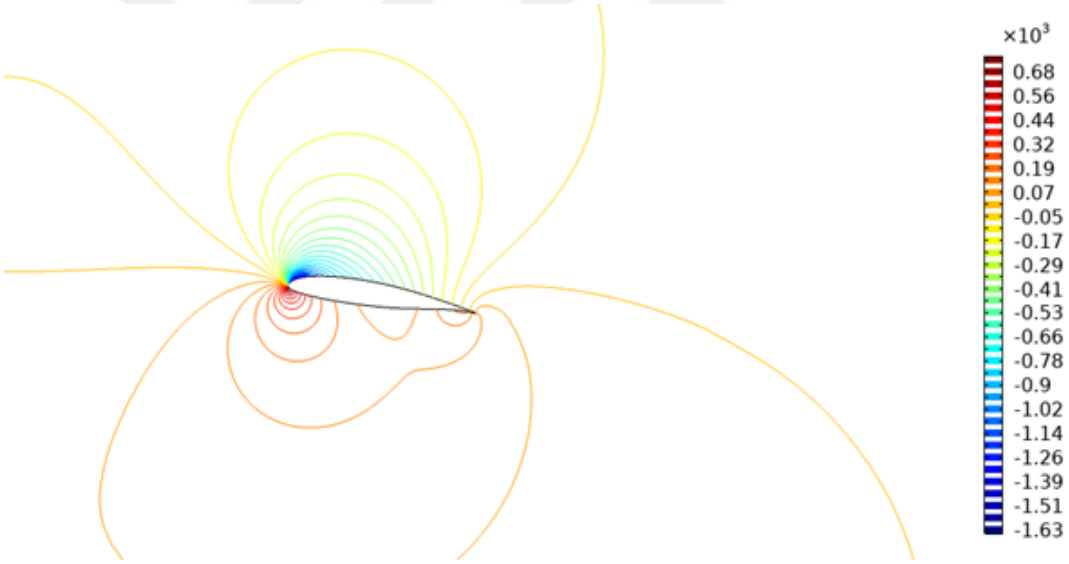

Figure 4.33 The 8-degree pressure boarders

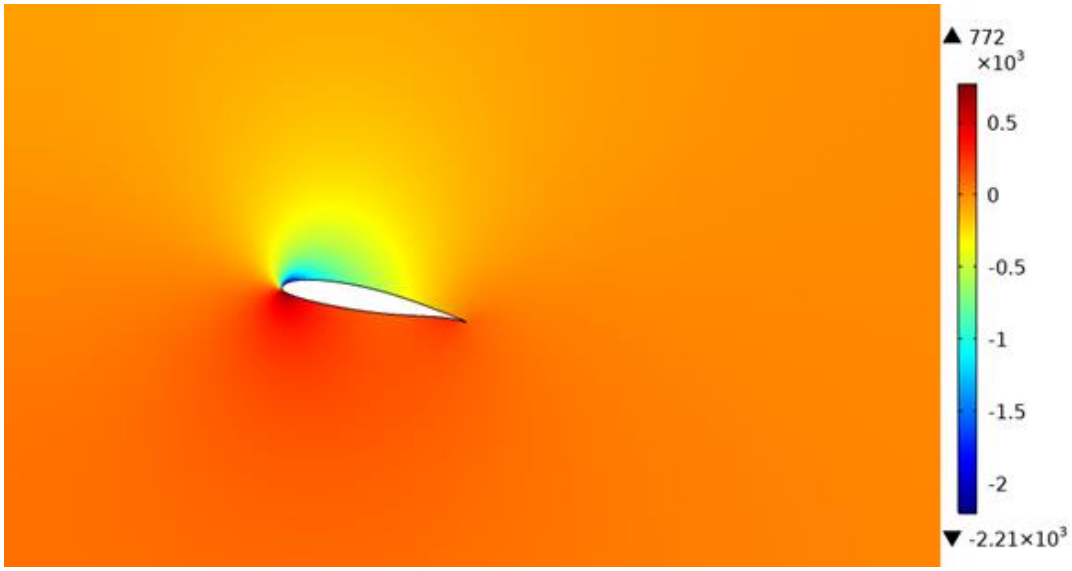

Figure 4.34 The 10-degree pressure contours

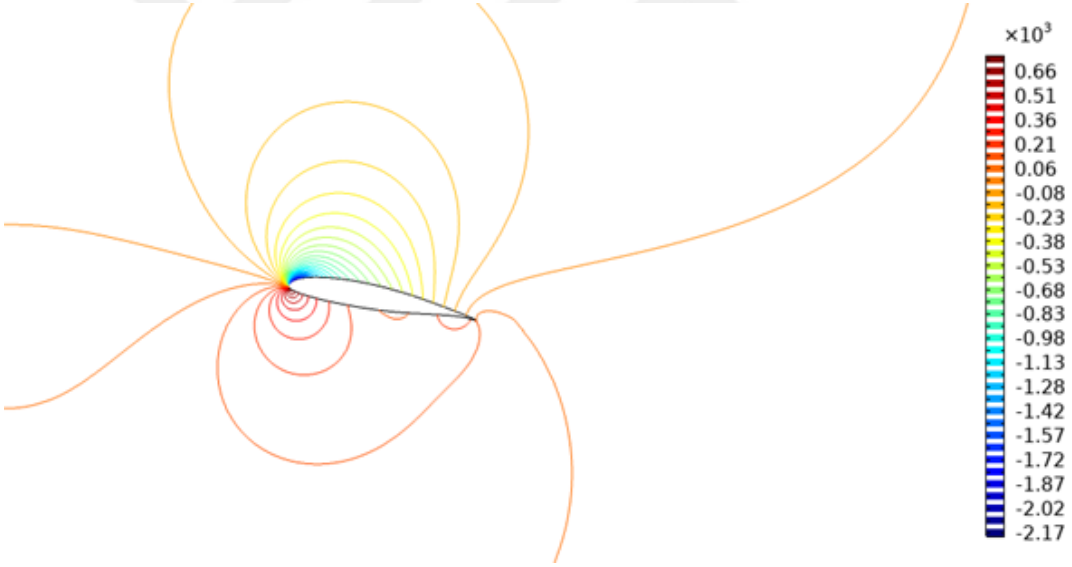

Figure 4.35 The 10-degree pressure boarders

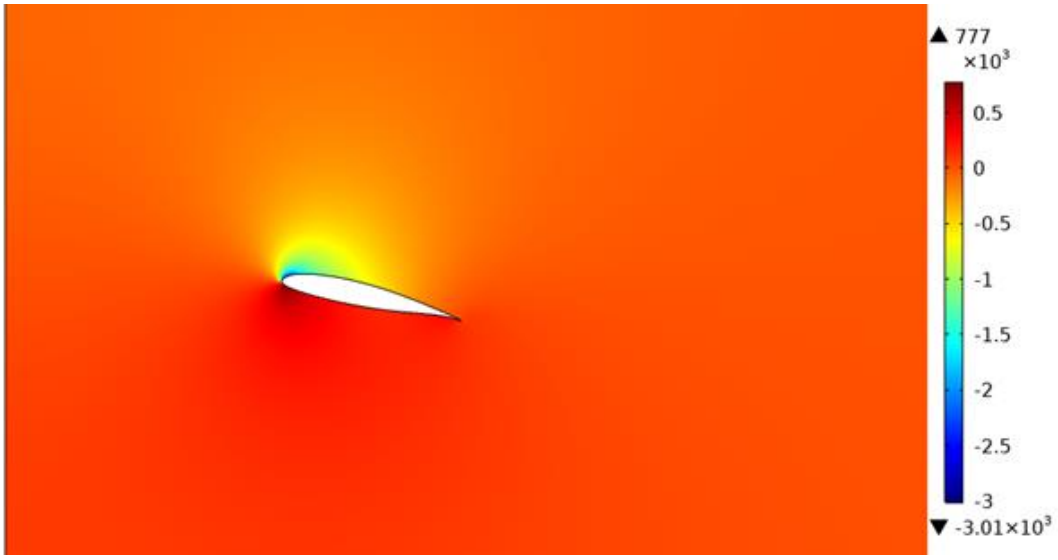

Figure 4.36 The 12-degree pressure contours

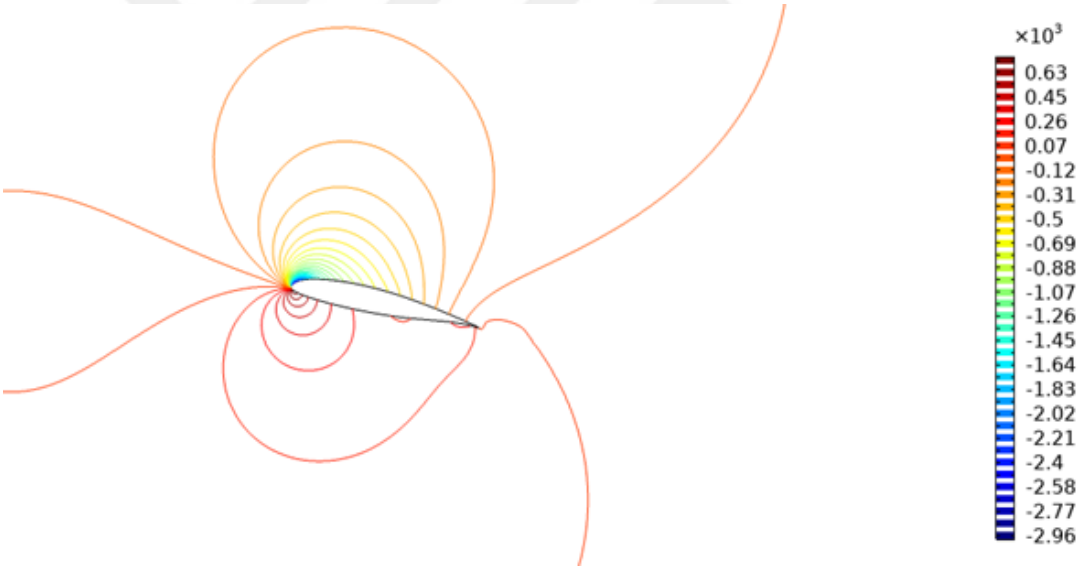

Figure 4.37 The 12-degree pressure boarders

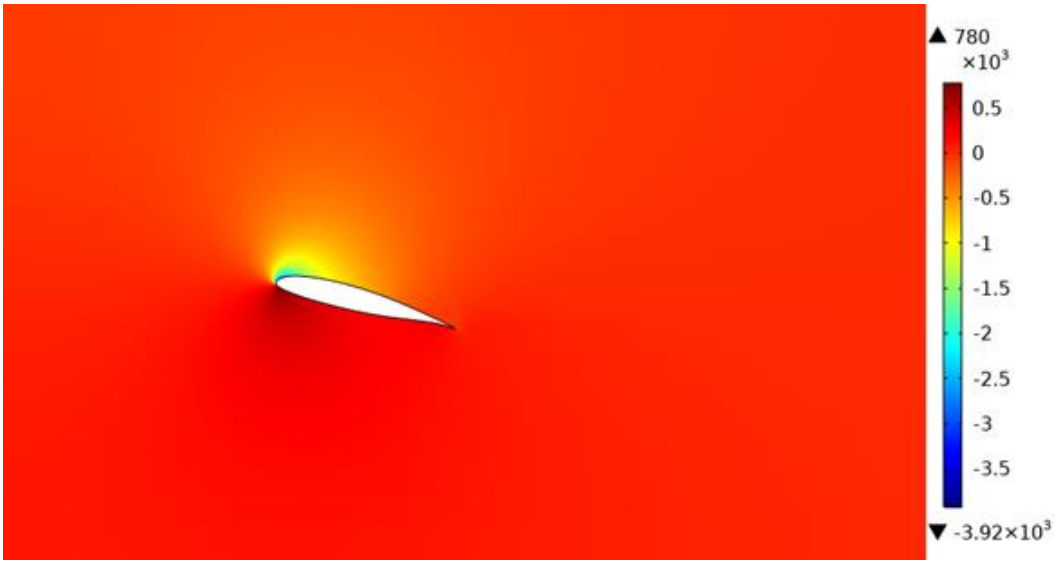

Figure 4.38 The 14-degree pressure contours

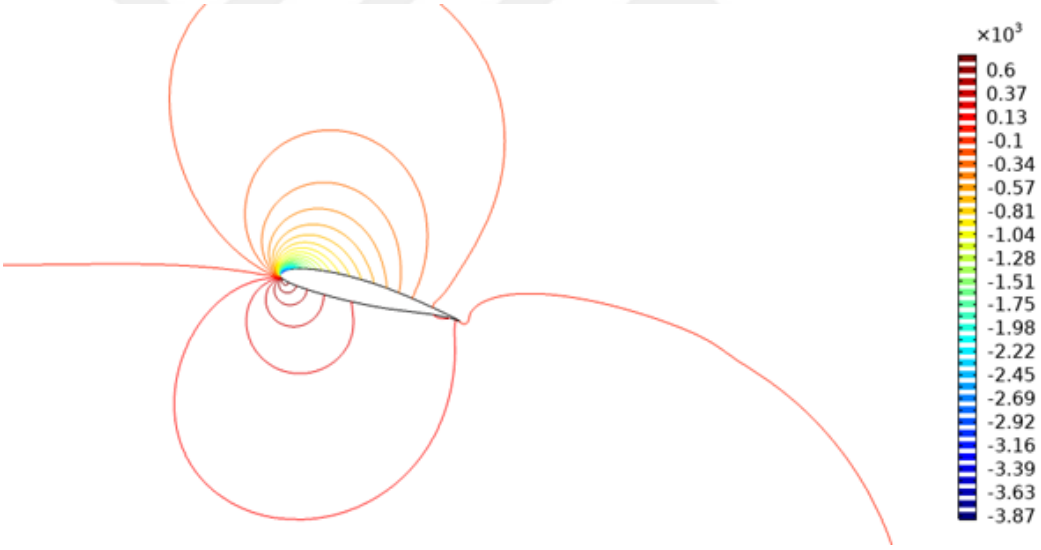

Figure 4.39 The 14-degree pressure boarders

As it is seen from the pressure contours, the produced lift certainly increases by angle of attack. The Cl-alpha graph of the wing, which was obtained by the CFD analysis, is presented in Figure 4.41. This graph has lower Cl value than the one in Cl-alpha graph, which was obtained by the XFLR5 software (Figure 3.9). The CFD and the XFLR5 results differ, both lead to the same conclusion: lift increases as the angle of attack increases.

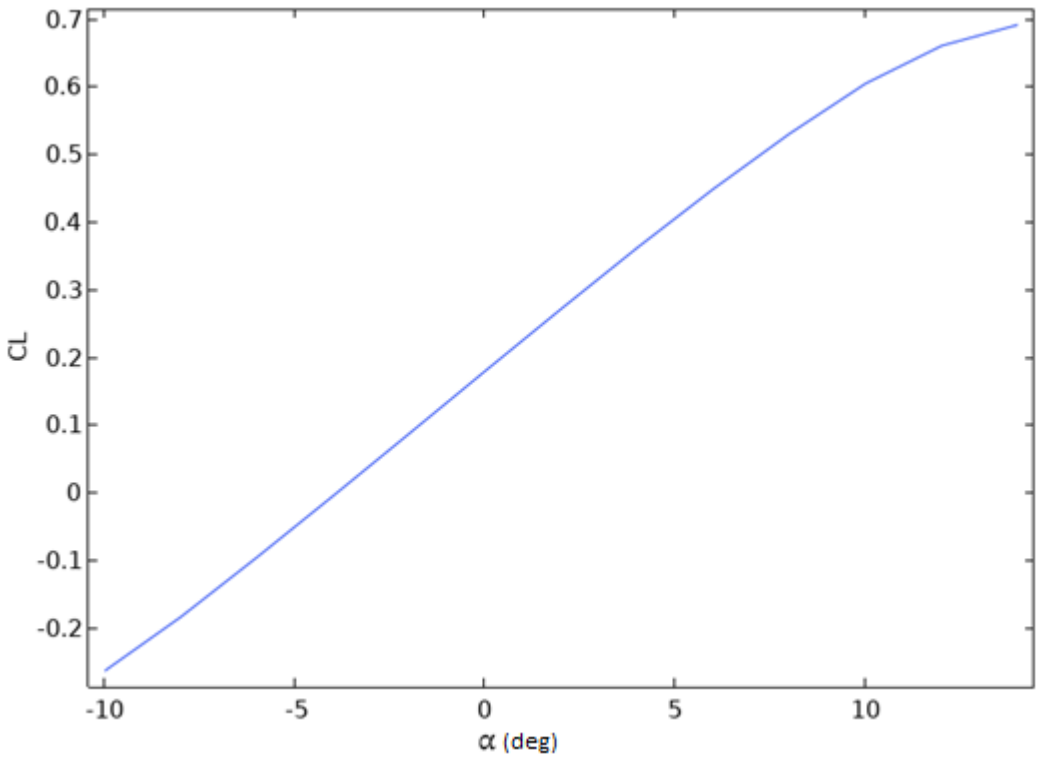

Figure 4.40 Cl-alpha graph gained by the CFD analysis

CHAPTER 5

TAKE OFF EXPERIMENT RESULTS

A test campaign was conducted to prove the proposal. A 2-degree configuration's properties are listed below.

- Weight: 2 kg
- Cruise speed: 15 m/s
- Flight time: 10 minutes
- Flight envelope: 2.85 km
- Stall velocity 7.5 m/s
- Incidence angle: 2 degrees.
- Payload: 0.3 Kg
- Maximum velocity: 21 m/s.
- Thrust: 2.7 kg

The first one was for +10-degree incidence configuration, and the second was for +2-degree incidence configuration. To measure the take off distance, lines with 1 meter intervals are drawn. As the total weight of the UAV is 2 kg, the NACA 4415 airfoil is selected for this UAV. The image of the UAV is given in Figure 5.2. The thrust of the selected engine propeller combination for this UAV is 2.7 kg. The mathematical model was constructed under these conditions, and take off time and take off distance were predicted in the computer environment. The constructed mathematical model has the same infrastructure with the former models. The only difference is that the Cl-alpha graph of wing is different from other constructed mathematical models because of the change of wing airfoil. The Cl-alpha graph for the NACA4415 was formed by the XFLR5 software, which can be examined in Figure 5.1.

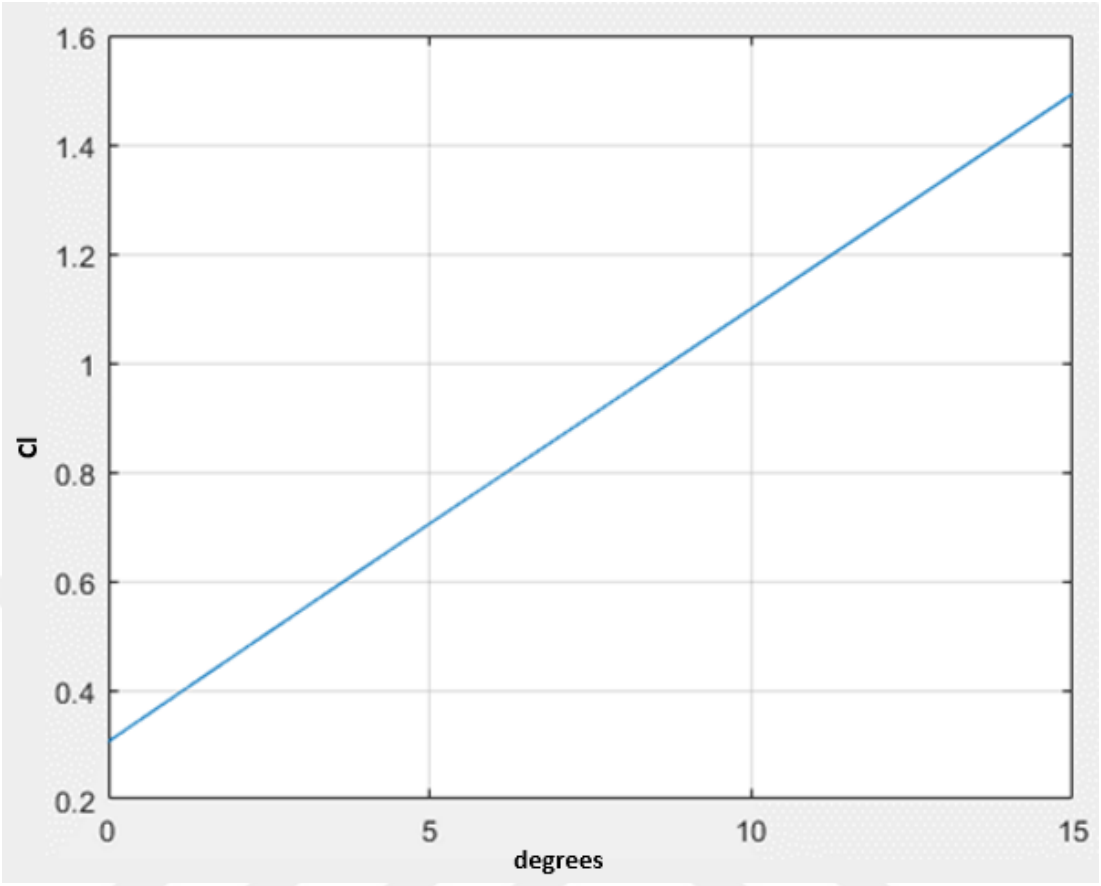

Figure 5.1 Cl-alpha graph of the NACA 4415

Figure 5.2 Experimental UAV

The velocity time graph for the 2-degree configuration is presented in Figure 5.3.

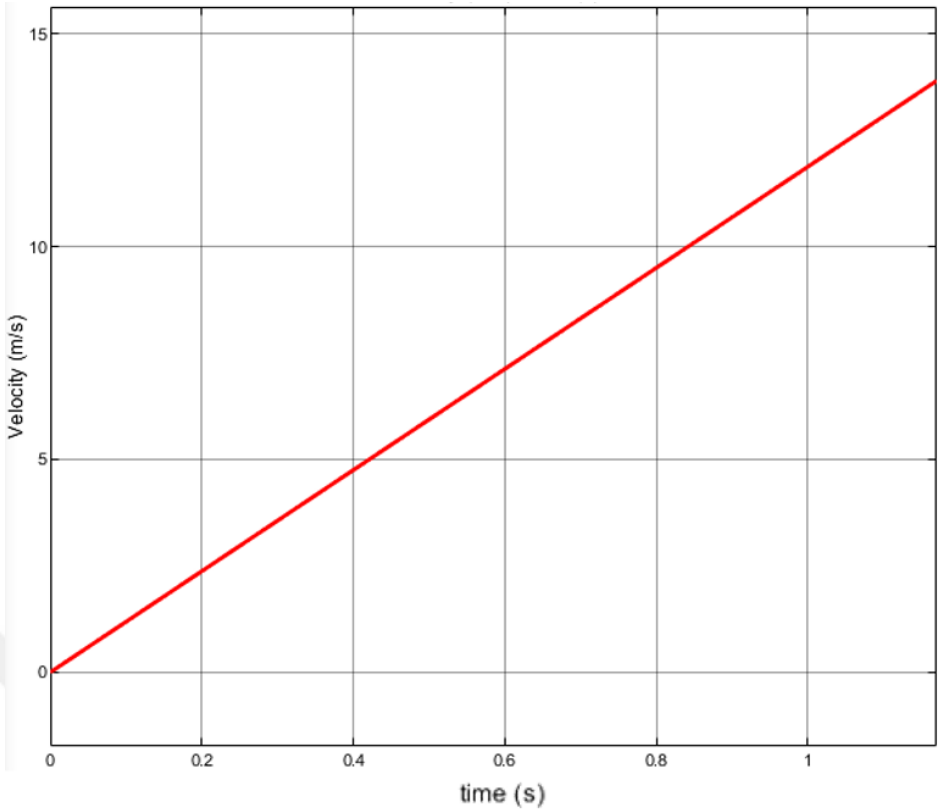

Figure 5.3 Velocity time graph for the 2-degree configuration

The lift time graph for the 2-degree configuration is presented in Figure 5.4.

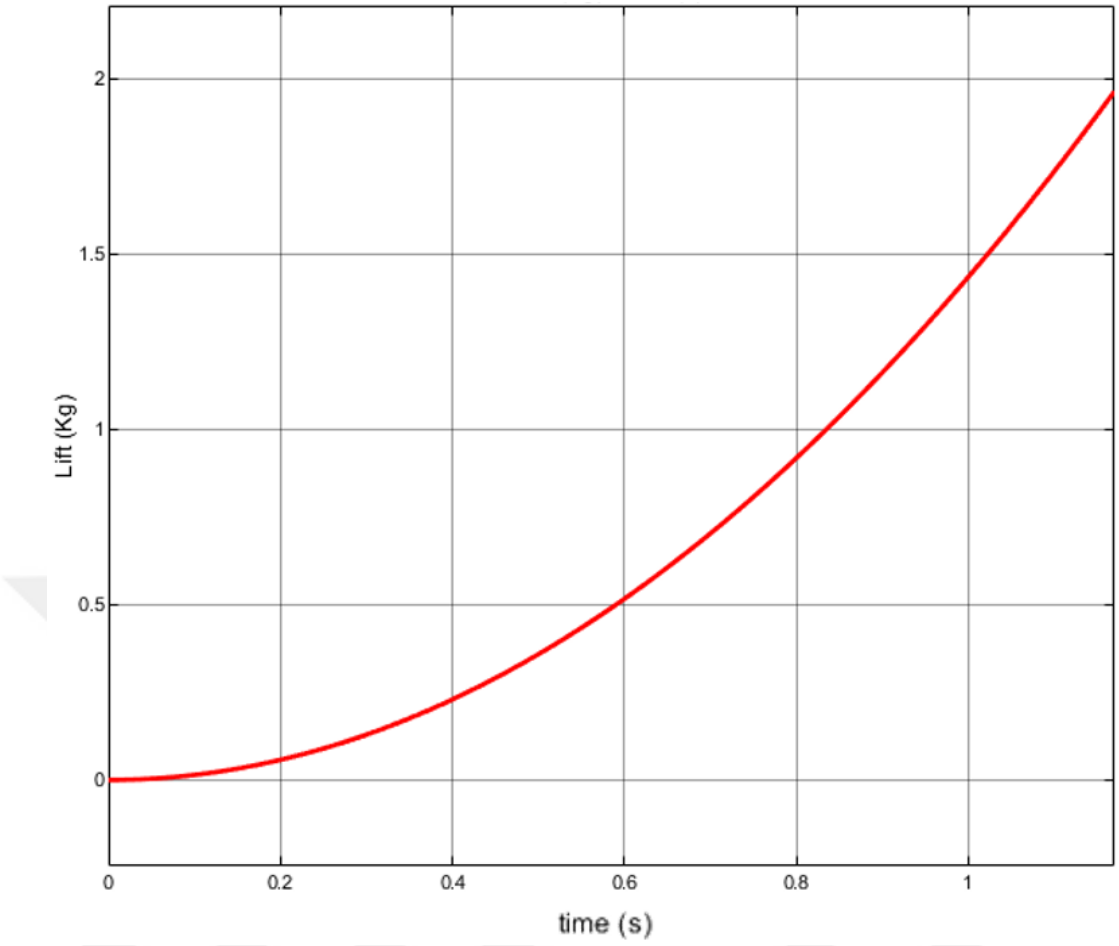

Figure 5.4 Lift time graph of the 2-degree configuration

The simulation for the 2-degree configuration was ended at the 1.17th seconds because the produced lift force reached 2 kg, which means take off. The position time graph for the 2-degree configuration is presented in Figure 5.6.

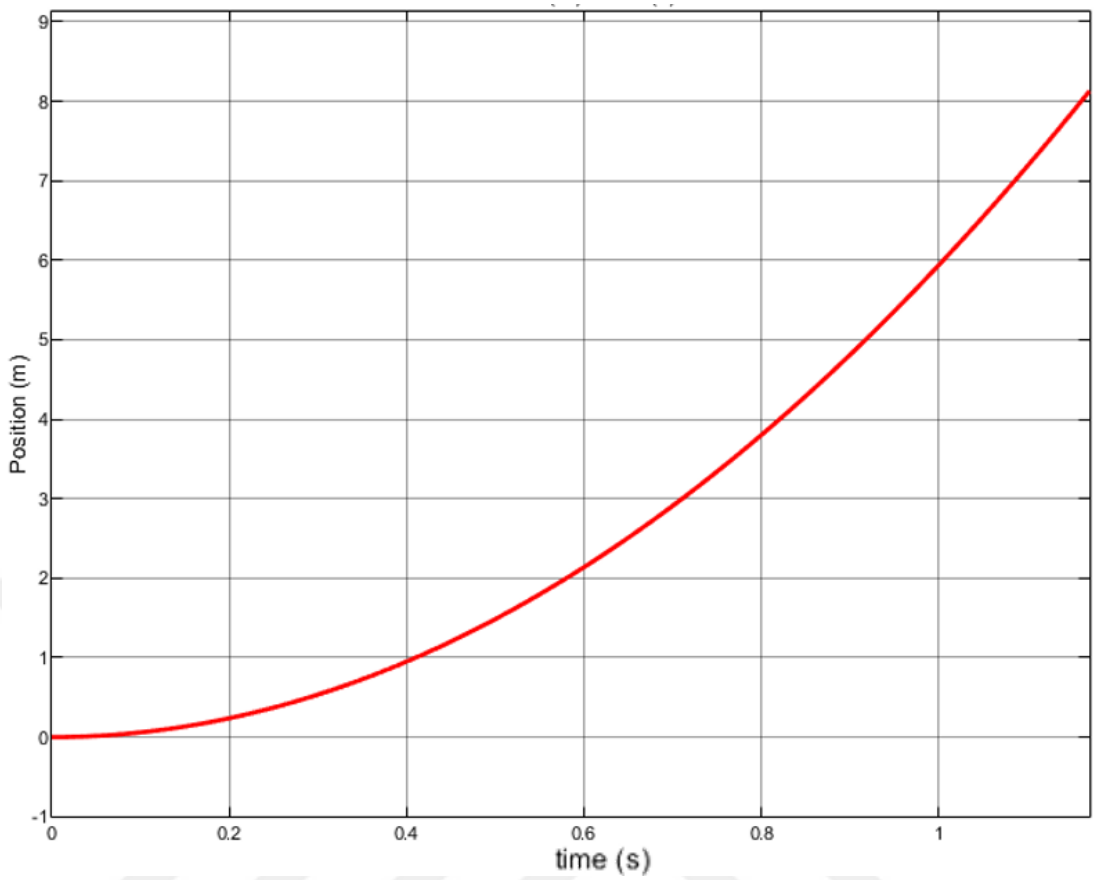

Figure 5.6 Position - time graph of the 2-degree configuration

As this graph shows, the experimental UAV takes off at 8 meters. The velocity time graph for the 10-degree configuration is presented in Figure 5.7.

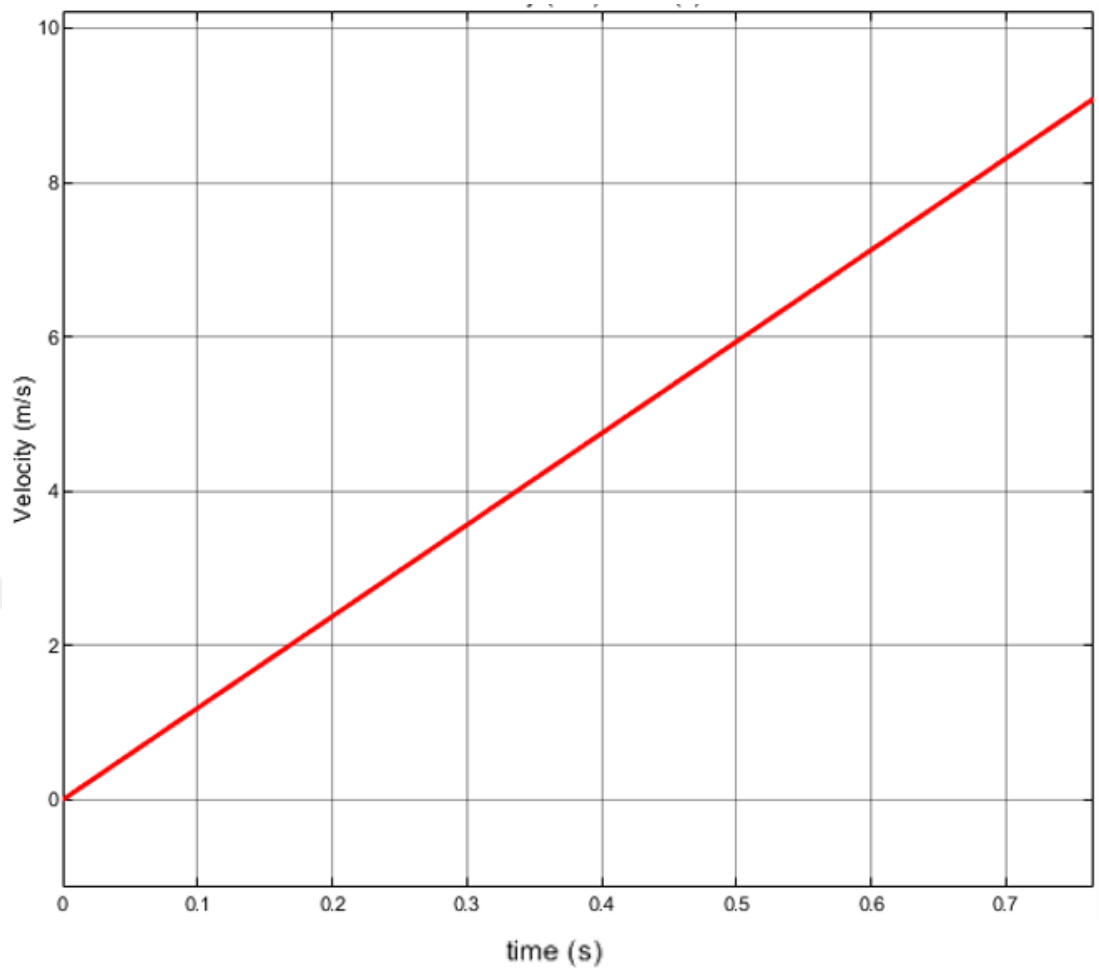

Figure 5.7 Velocity - time graph of the 10-degree configuration

A comparison of a 2-degree configuration velocity time graph and a 10-degree configuration velocity time graph reveals that velocity required for the 10-degree configuration was less than that required for the 2-degree configuration. Lift - time graph for the 10-degree configuration is presented in Figure 5.8.

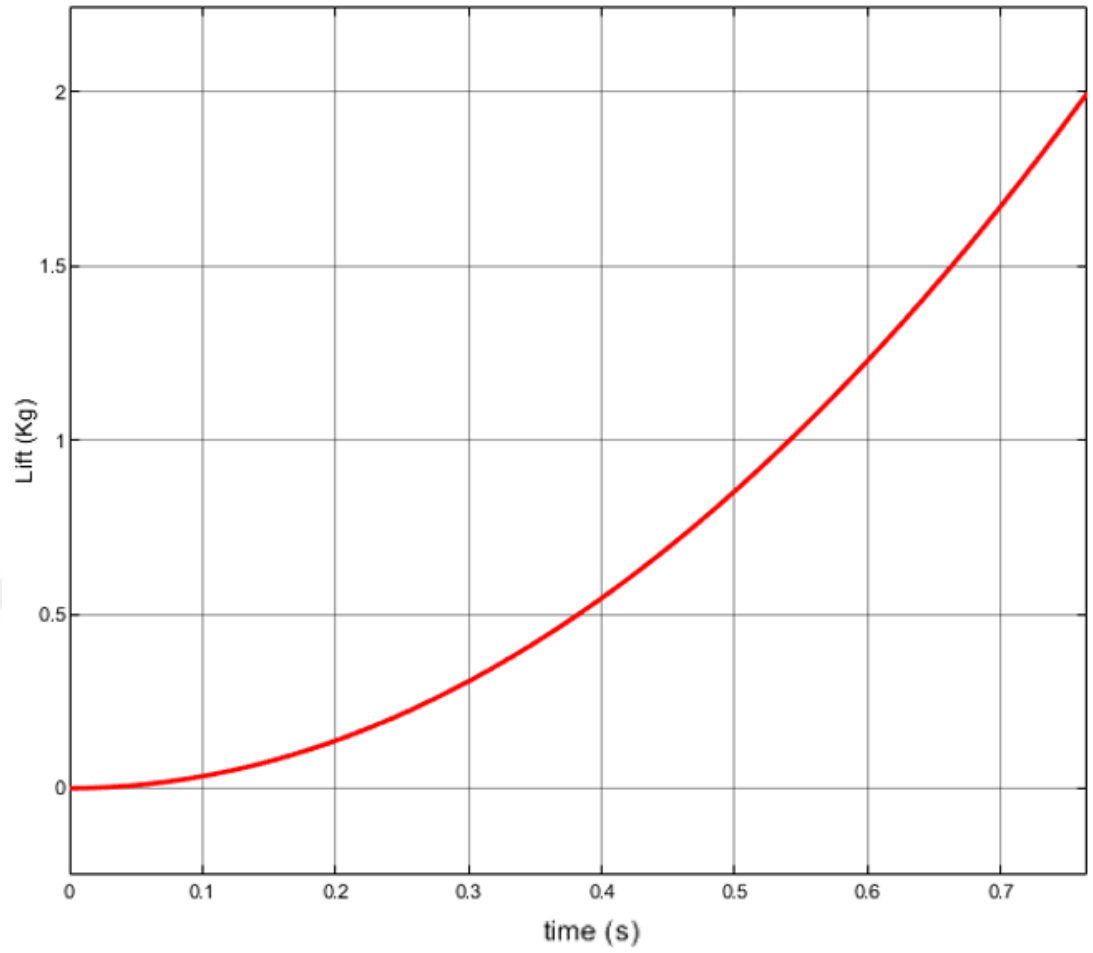

Figure 5.8 Lift time graph of the10-degree configuration

As Figure 5.8 presents, the aerial vehicle gets the required lift force at the 0.765th second; hence, the simulation time for the 10-degree configuration was ended at this time. The position time graph for the 10-degree configuration is shown in Figure 5.9.

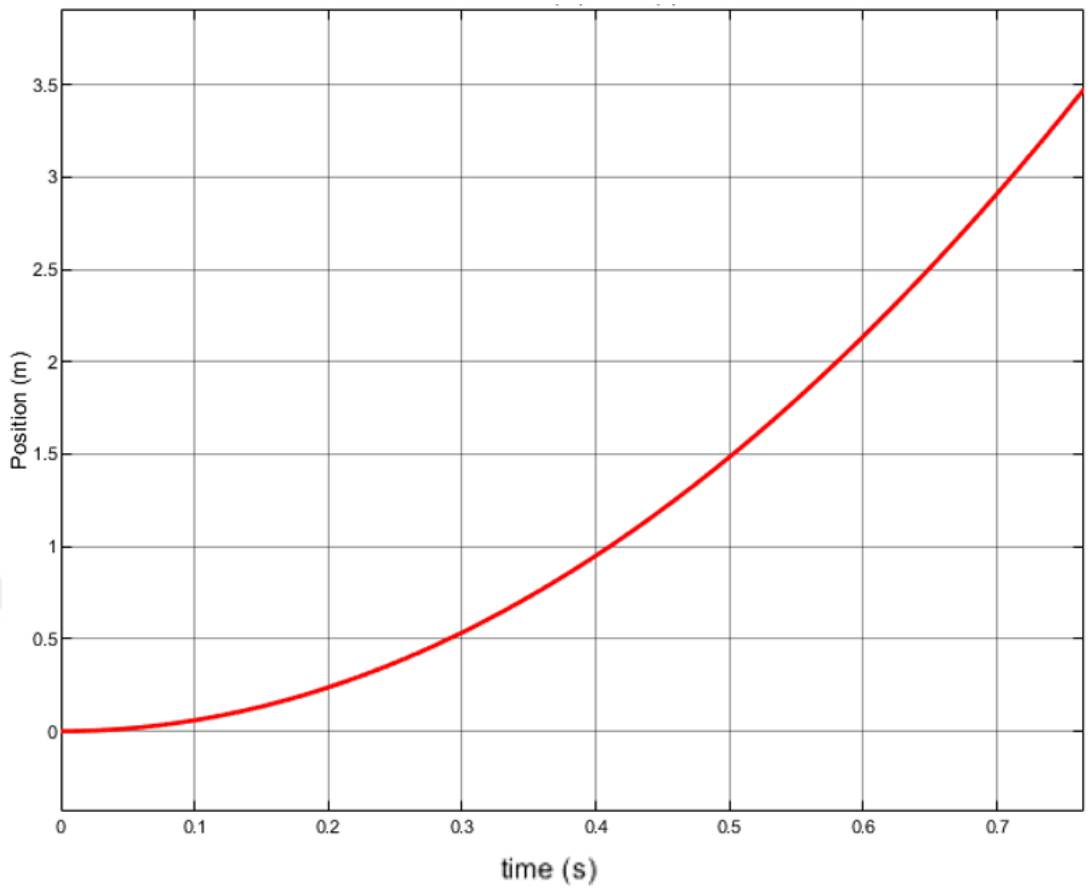

Figure 5.9 Position time graph for the 10-degree configuration

As it is seen in the position time graph, the runway distance required for the 10-degree configuration was 3.5 m. Considered that the required runway distance was 8 meters for the 2-degree configuration, the 10-degree configuration will certainly affect the required runway in a positive way.

In the experiment with the 2-degree configuration, the aerial vehicle could easily take off at 8 meters, which can be seen in the image from the flight test video in Figure 5.10. As you can observe from the figure, the take off took place at 8 meters of the runway, proving an obvious benefit: it can take off at a considerably short distance.

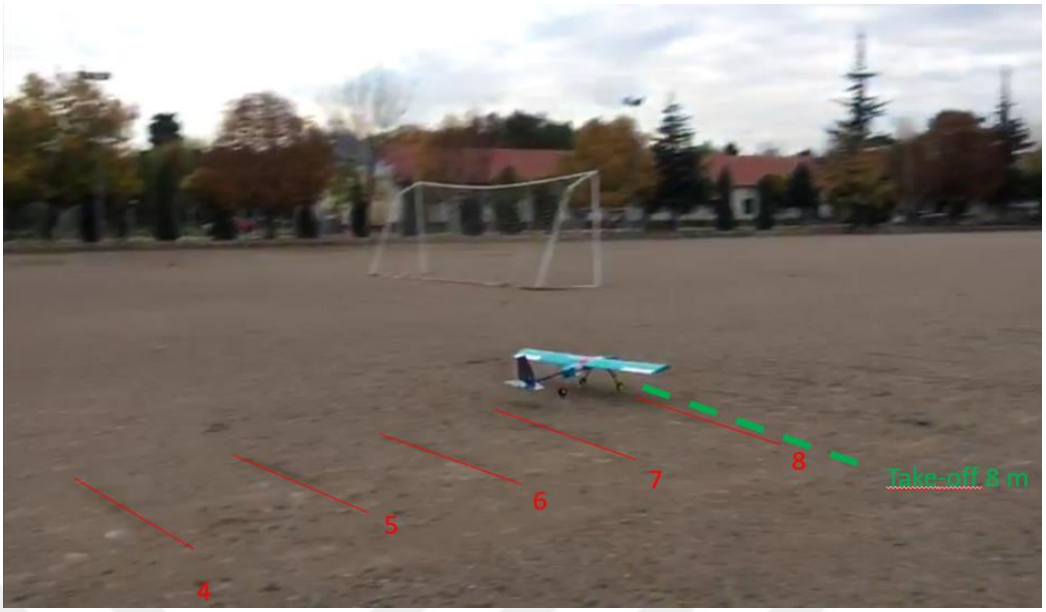

Figure 5.10 Take off position of the 2-degree configuration

The snapshot of the take off, taken from the 10-degree configuration video, is presented in Figure 5.11.

Figure 5.11 The take off position of the 10-degree configuration

The runway distance required for the 2-degree configuration was calculated as 8 meters in the mathematical model. In the flight experiment, the 2-degree

configuration's take off took place at 8 meters of the runway, which verifies that the constructed mathematical model gives accurate results. The 3.5 m take off distance, which was calculated by the mathematical model, was measured as 4.5 m in the flight experiment. This discrepancy could be linked with the following factors:

1- Decrease in the lift force due to airfoil's damaged regions [24]

2- Increase in tip vortexes due to the increased incidence angle [25]

3- The probability that Cl-alpha graph, which was calculated by the XFLR5 software, is not that accurate.

CHAPTER 6

APPLICATION OF PATENTS

It this thesis, completely novel ideas were proposed for easy and short distance take off. All the necessary tests and verifications were performed. The angle of attack of model aircraft was changed from 2 to -0 degree, and this change was performed by a mechanism. A special mechanism was designed for the wing and the ruddervator that was capable of changing the angle of attack of the wing and the ruddervator during the operation. All the findings in this study proved that the novel ideas proposed are applicable, so three patents applications to Turkish Patent Institution were made with these application numbers: 2021/015233 – 2021/015231 – 2021/015227.

6.1 Design of Variable Incidence Wing Mechanisim

The working mechanism of the variable incidence wing was grabbing the wing spars inside the fuselage and turning them nearly around the aerodynamic center. The rotation center was selected as the aerodynamic center mainly to prevent the rapid moment changes caused by an incidence angle change [26]. Slotted holes were designed at both sides of fuselages to allow entrance of wing spar into fuselage and rotational movement inside it. These holes can be seen in Figure 6.1.

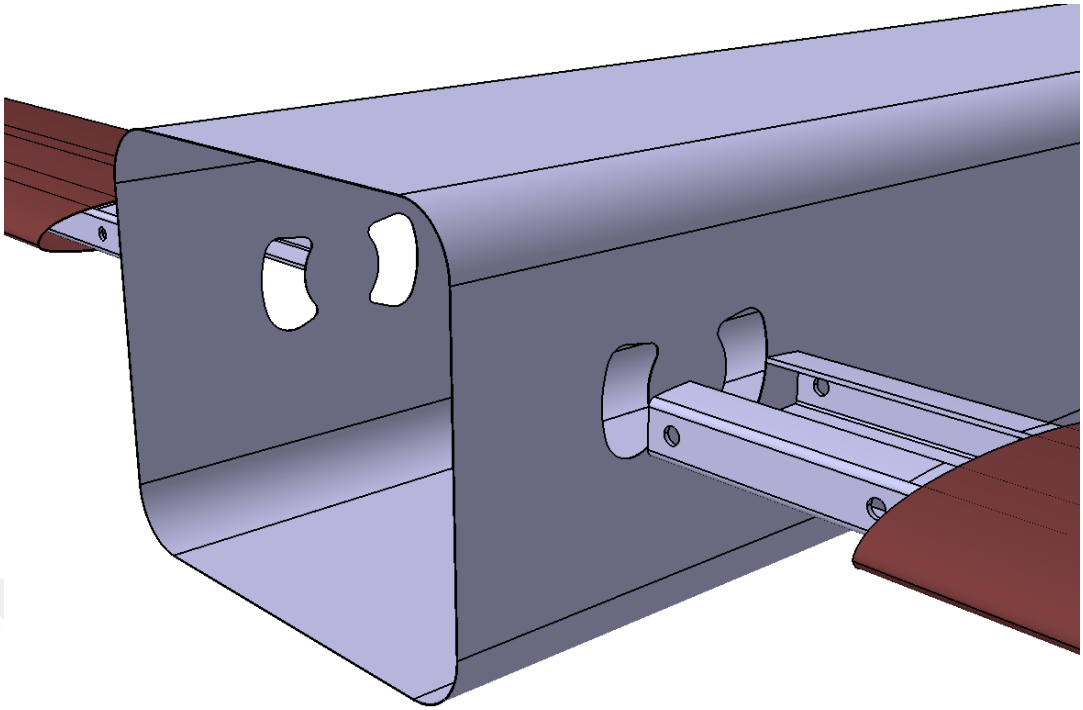

Figure 6.1 Fuselage slots

As it is shown in the Figure 6.1, the slotted holes that were created in the fuselage were designed in a way that fits the spar shape. As spar profile, C profile was selected, though any box profile could be selected according to the calculations. The C spar has easy manufacturing capability, yet it also has some disadvantages. One of its major disadvantages is the shear center of the C profile. When the wing is loaded, the spars rotated around the shear center of spars, which creates external forces in the spar web region. This situation is a disadvantage for the C spar because both the I spar and the box spar have shear centers inside them [27].

Another important feature of the mechanism is the main carrier beams designed. They were assembled with the spars as presented in Figure 6.2. The wing spars were connected to the main carrier beam by means of two pins on each spar. Consequently, all the forces that the wing produces was transmitted to the main carrier beam by these pins. The main carrier beam design was crucial because all the forces acting on the wing were carried through it. Any damage that occurred in the main carrier beam can cause a catastrophic failure of the whole aircraft. As the main carrier beam is a category

A structure, this means a catastrophic failure of the whole aircraft. The analytical analysis of the beam is very important for beam design because the analytical findings give us important clues to or early predictions about design decisions.

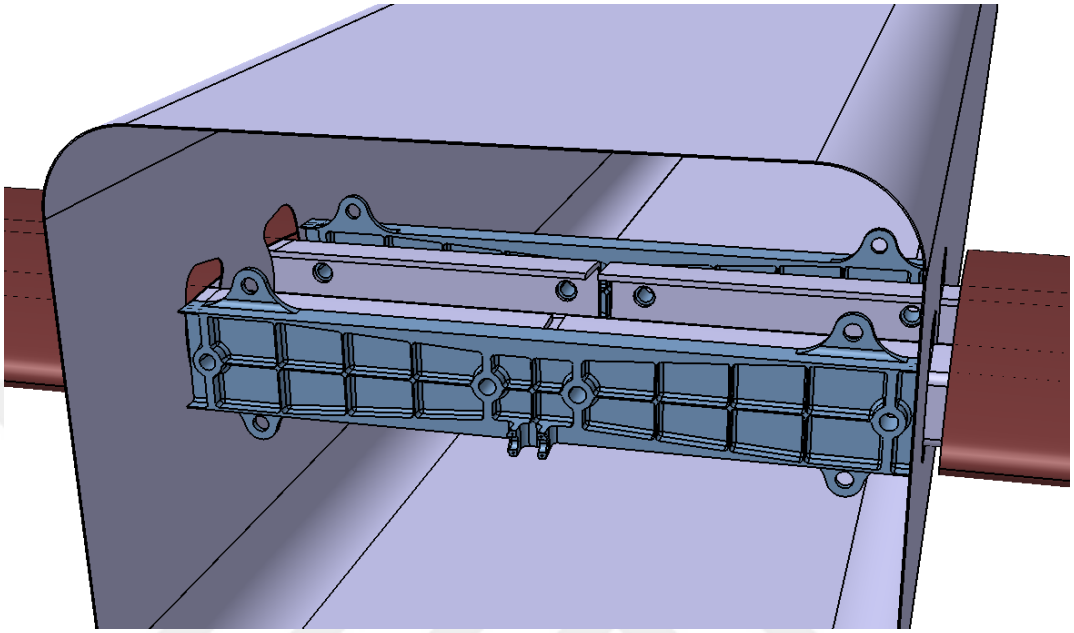

Figure 6.2 Main carrier beam

The main acting forces that define rough sizing of beam could be seen in Figure 6.3. As it is shown in the figure, when only the main carrier beam was isolated, it was subjected to a 4-point bending. Actually, the 4-point bending is a kind of experiment that reveals the bending and shear behavior of the structure [28].

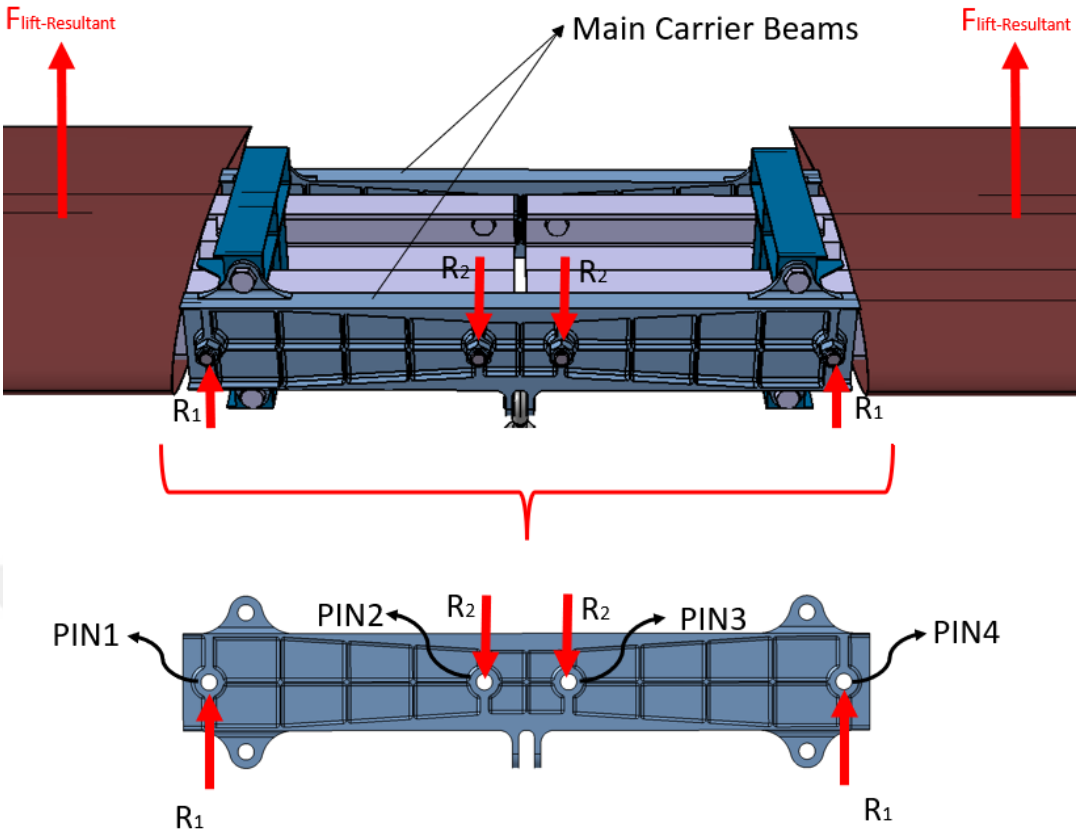

Figure 6.3 Acting forces

The free body diagram of the main carrier beam and the moment shear diagram are presented in Figure 6.4.

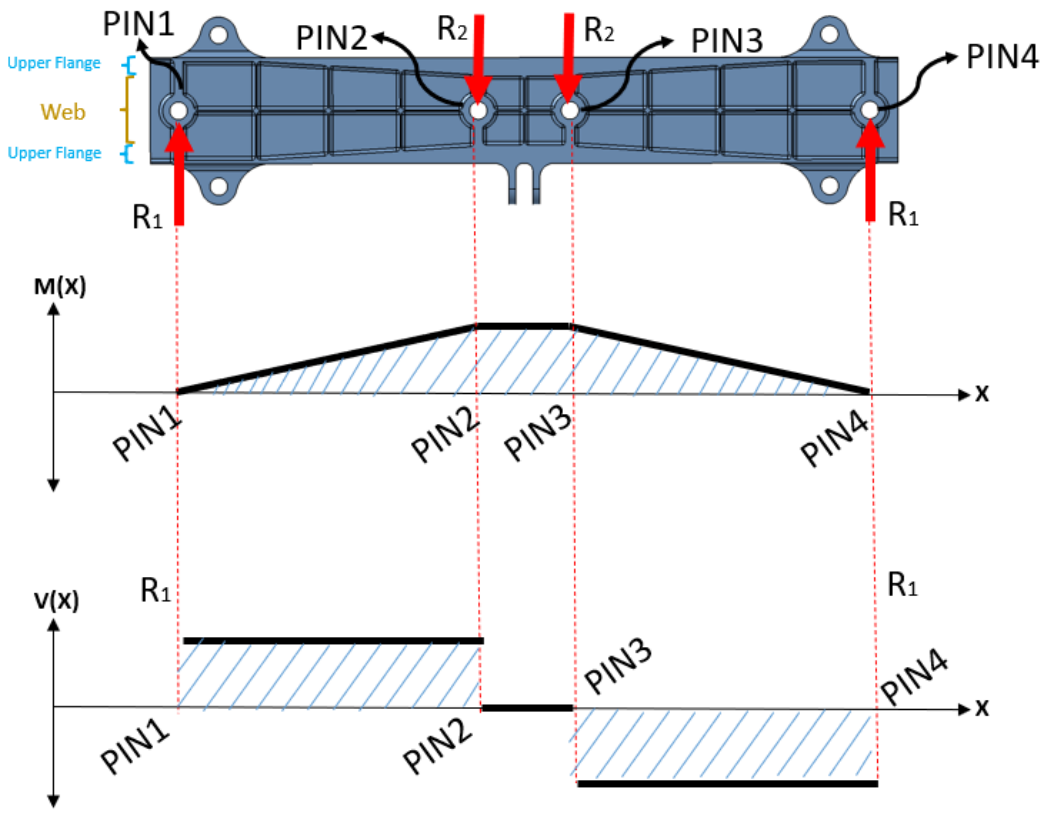

Figure 6.4 Free body and moment - shear diagrams of the main carrier beam

As can be clearly seen in the moment diagram, the moment acting on the beam was zero at PIN 1 and PIN4 and the moments acting on the body increase up to PIN2 and PIN3. The region between PIN2 and the PIN3 is a pure bending region with no shear. Simplified bending stress formula is explained in Equation (6.1) [29]

$$\sigma = \frac{Mc}{I} \qquad (6.1)$$

c = The distance from the neutral axis to a point

I = Moment of inertia

M = Applied moment

Bending stress over the cross-sections is illustrated in Figure 6.5.

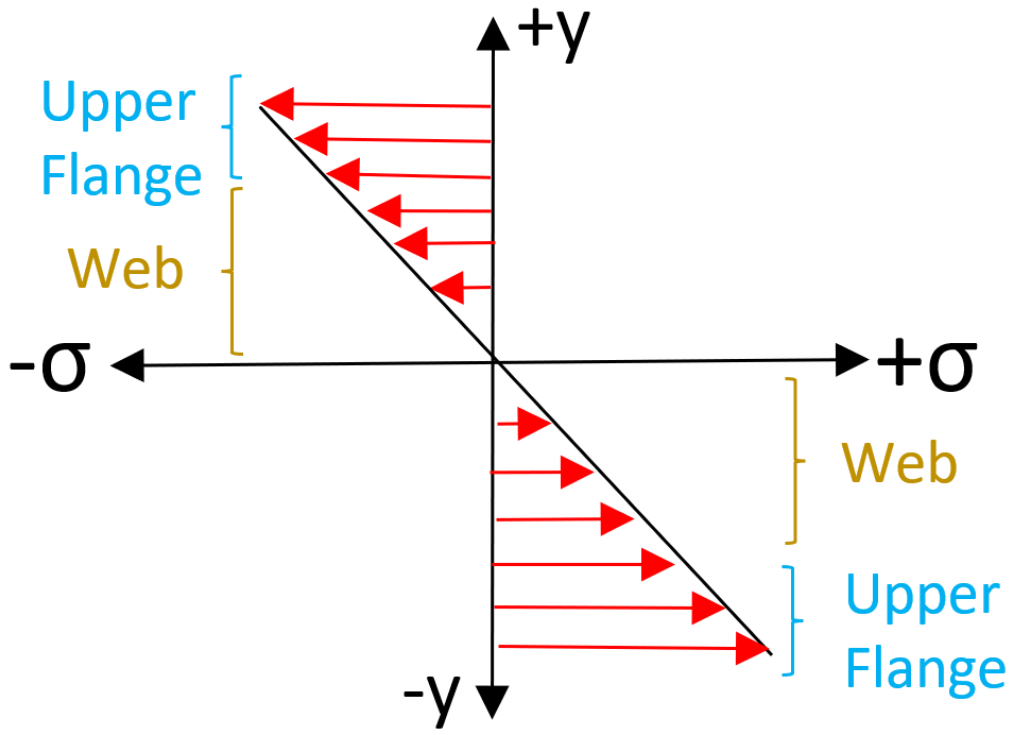

Figure 6.5 Bending stress graph over the cross section

In Figure 6.5, the main bending carrier region was at the top and bottom of the cross-section of the structure. The bending stress formula and its graphical representation seem to show that the bending acting on the body was carried primarily by flanges. Thus, would be logical to determine the thickness of upper and lower flanges according to the bending stress carried. The bending moment was increased from PIN1 to the PIN2, and from PIN4 to the PIN3, as shown in Figure 6.4. Hence, the flange thickness was increased from PIN1 to PIN2, and PIN4 to PIN3 linearly, as the bending moment increases linearly. This design can achieve the homogeneous stress distribution on flanges. Because the bending moment intensity increased from PIN1 to PIN2 linearly and the part that carries bending was flange, the flange thickness increased linearly from PIN1 to PIN2. The flange region that was under and above the lug region1 and 2 was kept at a certain thickness as this area was a force flowing area, which is shown in Figure 6.6.

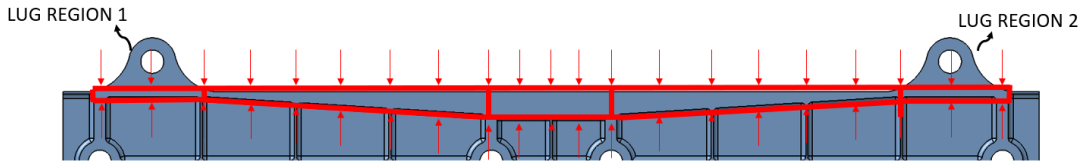

Figure 6.6 Flange thickness change over beam due to acting bending moment

Another important force is the shear force acting on the cross-section.

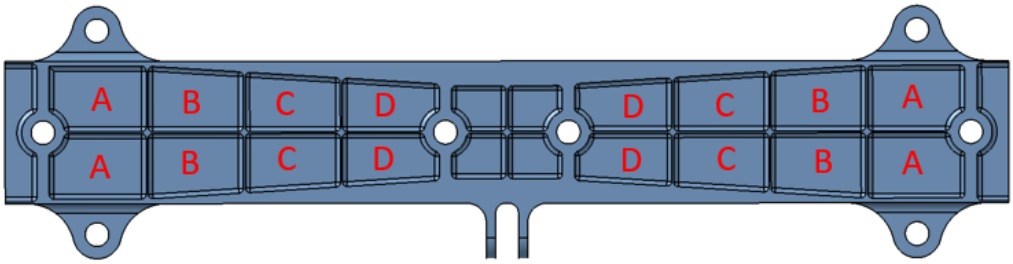

Figure 6.7 Beam web region divided design

The web region of beam was divided so that a small crack that occurred would not grow progressively. In other words, the divided web enables us to limit a potential crack propagation, thus prevent a catastrophe. The web regions that were limited with stiffeners are shown in Figure 6.7. The shear stress acting on the cross-sections can be explained in Equation (6.2) [30].

$$\boldsymbol{\tau} = \frac{VQ}{It} \qquad (6.2)$$

V: Internal shear force

Q: First moment of inertia

I: Moment of inertia

t: Thickness

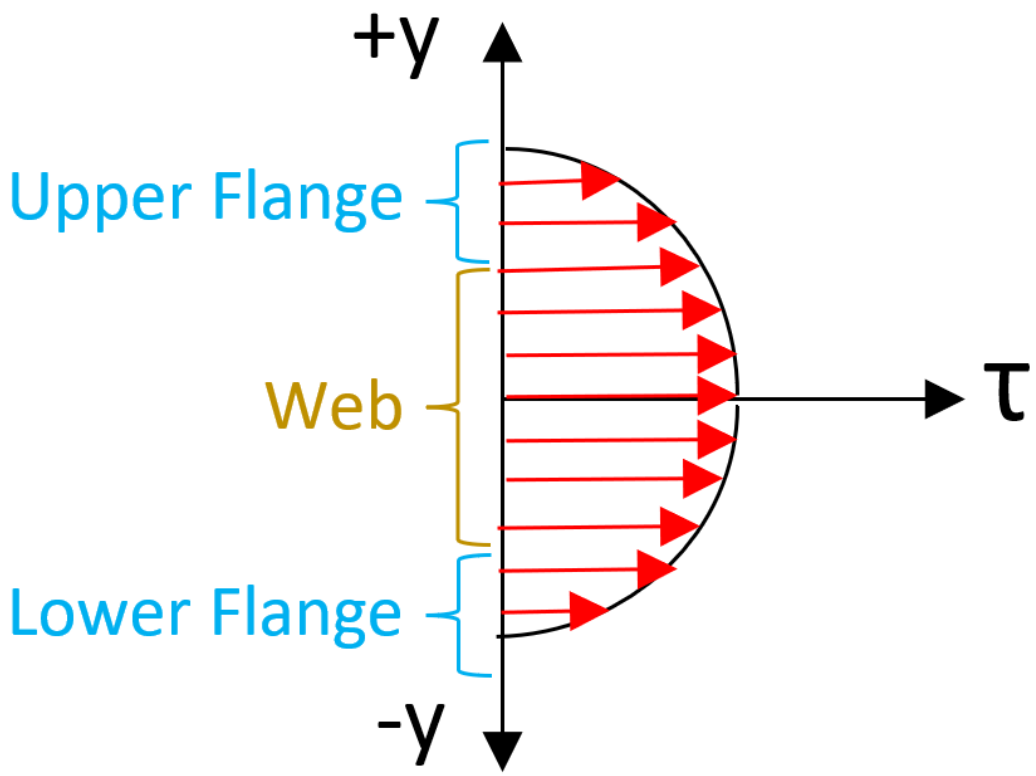

Figure 6.8 Shear stress graph over cross-section

Obviously, the shear stress was primarily carried by the webs of the section. Almost no shear stress exists on the flanges, in contrast to in the webs. From this point of view, it seems that this structure carried shear stress by its web region. Such regions, e.g. region A, B, C, or D, are represented in Figure 6.7. The thickness of the web can be defined as same without considering parameters other than the shear stress. When the shear and the bending stresses are considered together, the thickness of D should be greater than that of C, and in the same manner, C should be greater than B and, B greater than A. Indeed, the bending stress acting on the structure increases from A to the D, while shear stress does not change from A to D.

The main carrier beams were connected to adaptors to transmit the acting force on the main carrier beam to the fuselage frame. Adaptors were designed in a way that they would withstand the acting forces on the main carrier beam, turn around the aerodynamic center of the wing, and transmit the acting forces to the fuselage frame.

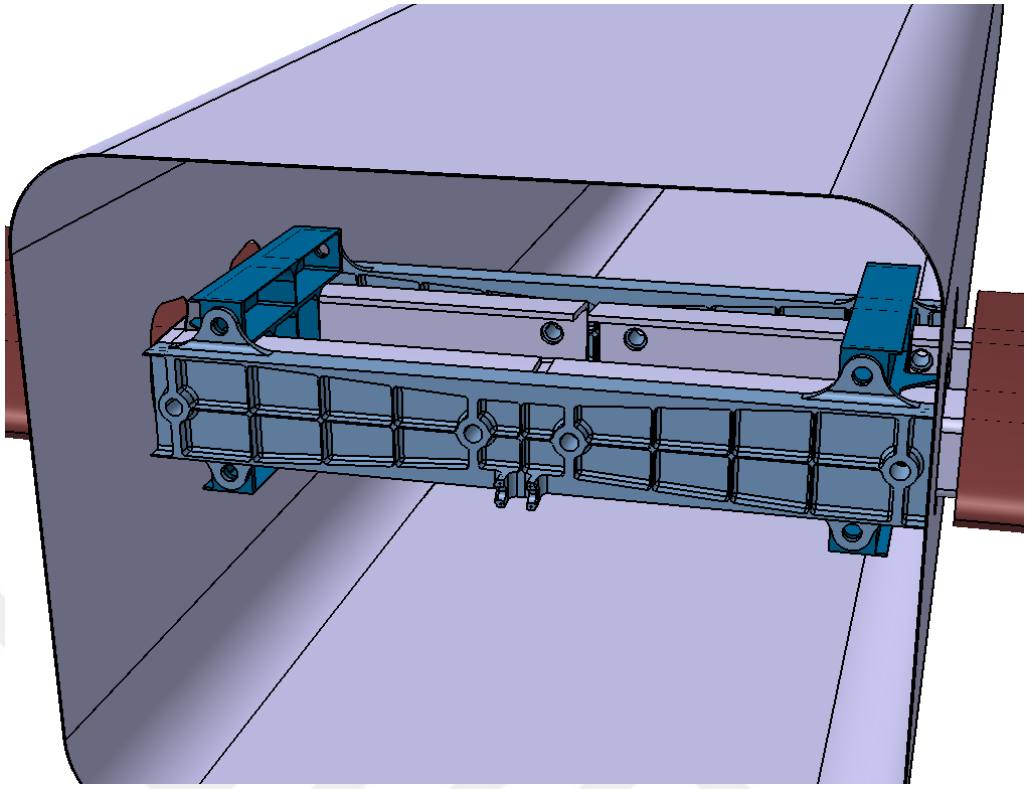

Figure 6.9 Carrier adaptor design

The adaptors were connected to the main carrier beam by the help of the four lugs as illustrated in Figure 6.9. With the addition of adaptors, the box structure design that would be turn around the aerodynamic center of wing was completed. Actually, this box structure was the core structure of the mechanism. It was connected to the fuselage frame by the bearing unit. The reason why bearing housing unit was preferred was that these systems allowed both force flow and rotation around the specified axis. That is how the rotational movement was took place. During the design of the fuselage frame, the frame was assembled to the fuselage by means of mechanical fasteners of rivets, as shown in Figure 6.10. The frame has certain hole patterns that allow stringers to pass through.

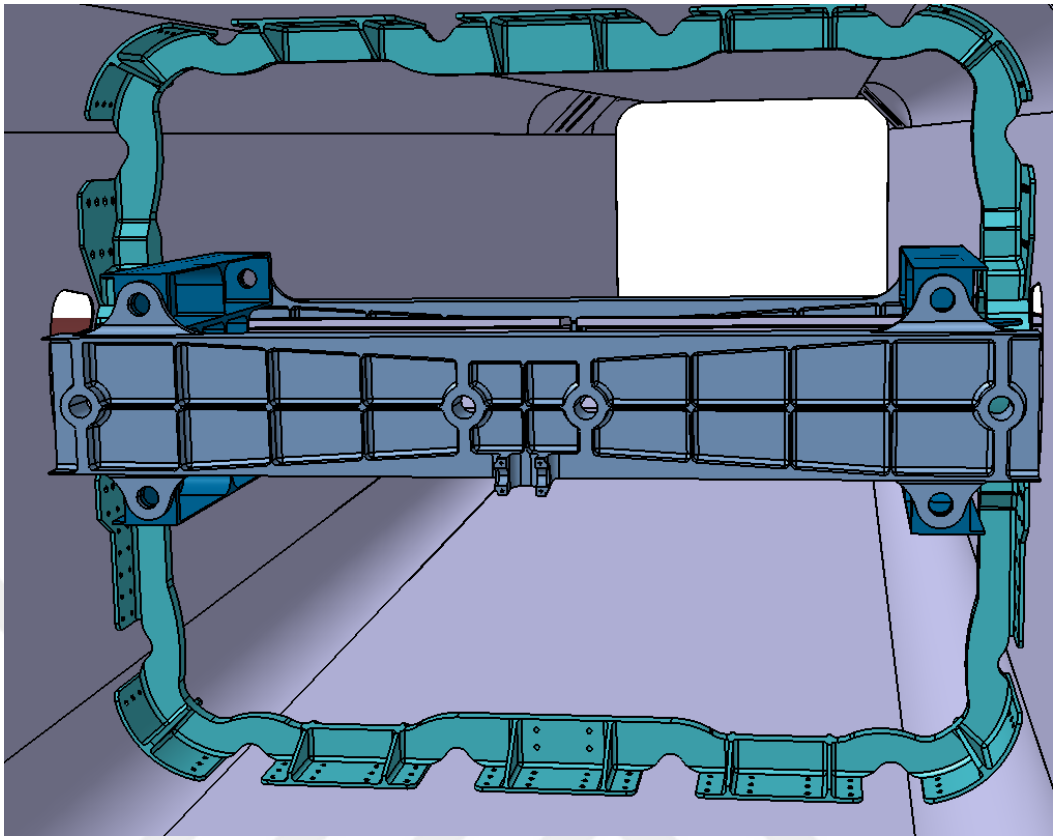

Figure 6.10 Fuselage frame design

The designed box structure can turn around the bearings. Figure 6.10 demonstrates the 0-degree position of the box structure, and Figure 6.11 demonstrates the 10-degree position of it. In this situation, the box structure can turn around the bearing axis without any controllable mechanism, which was not preferred in design phases. To both control the angular position of the box structure and limit the rotational movement when needed, at least one actuator had to be added into the system. This actuator system could be a hydraulic actuator, as well as an electromechanical one like servo motors. The selection of the actuator system depends on several parameters like the actuation force required and hydraulic system availability on aircraft. In this design, the servo motor actuator was preferred to control the position accurately and easily as the weight of an additional equipment has always been a safety issue.

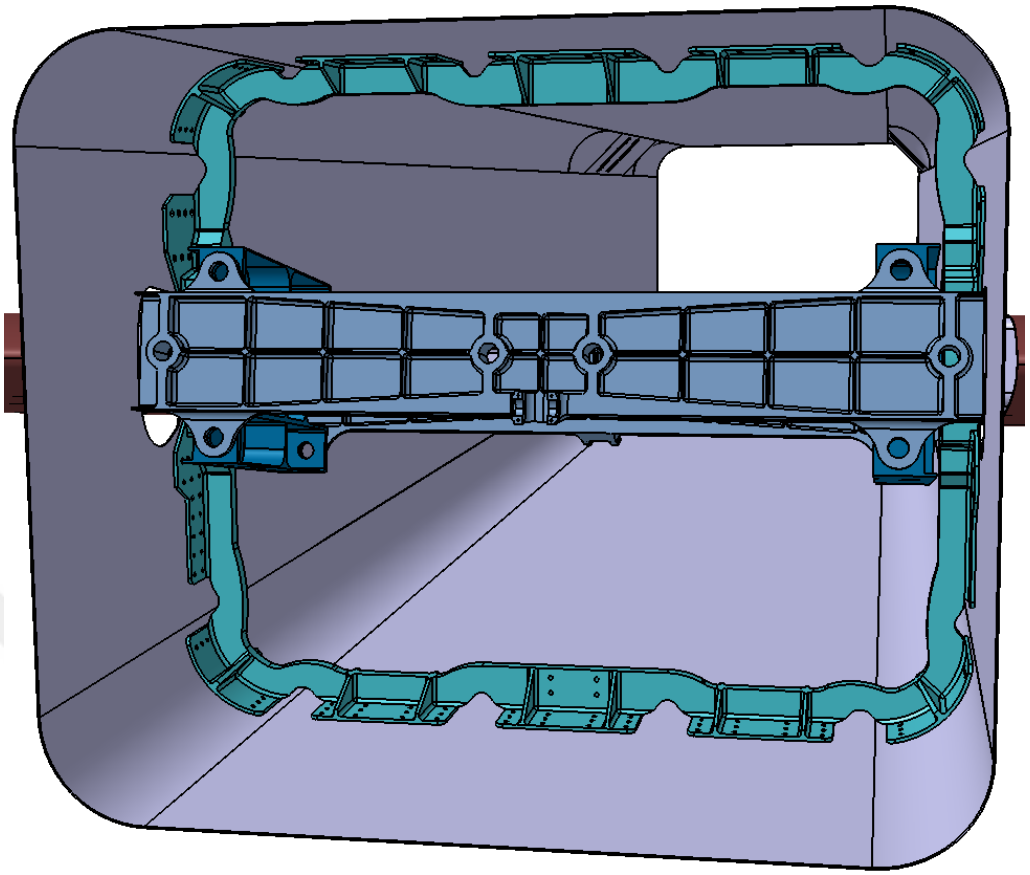

Figure 6.11 The 10-degree position of box structure

The actuator was designed as shown in Figure 6.12 by using this actuator, the angle of attack of the box structure, and hence the incidence angle of the wing, could be changed precisely. The pitch moments created by the wing were also reacted by these servos. In case the servo motor malfunctions, the second servo motor was added to the mechanism to ensure the flight safety as displayed in Figure 6.13 The redundant servo motor was attached to the back main carrier beam. The connection between the main carrier beam and the servo nut was a piston crank connection with two bolts. It was design as such to make the assembly easy. Functionality was also tested. The safety issues were considered in case of a failure of the servo.

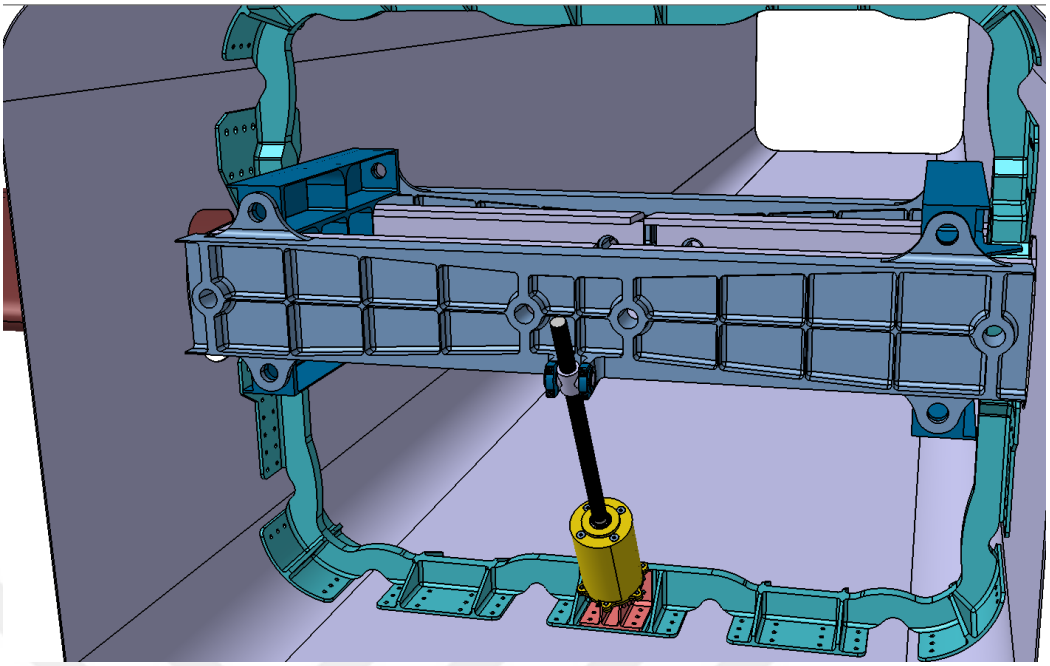

Figure 6.12 Actuator design

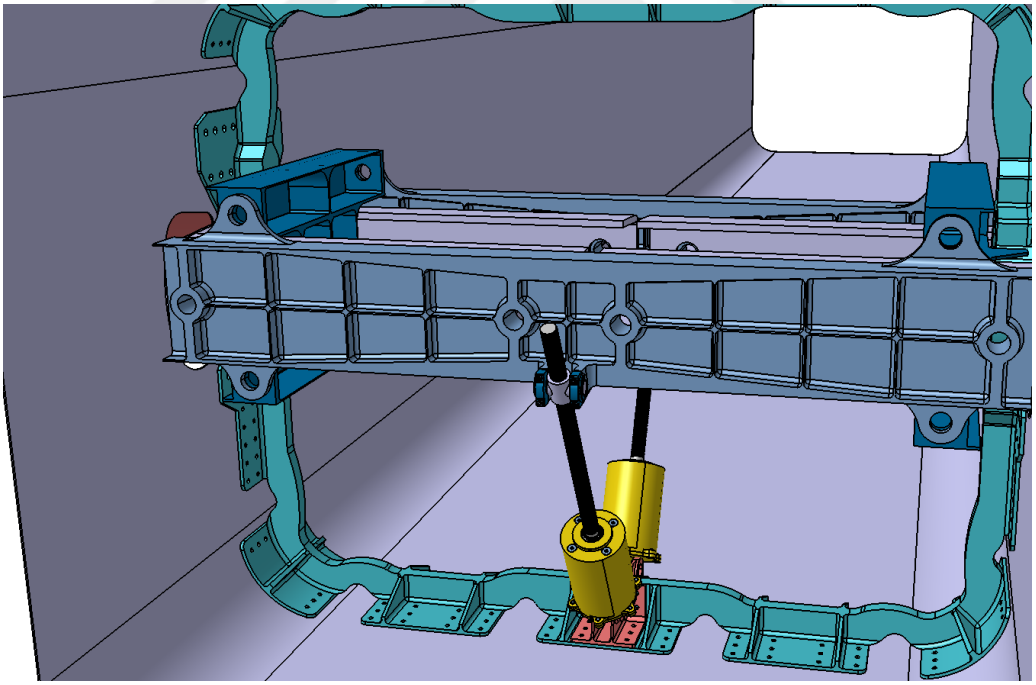

Figure 6.13 Redundant servo motor design

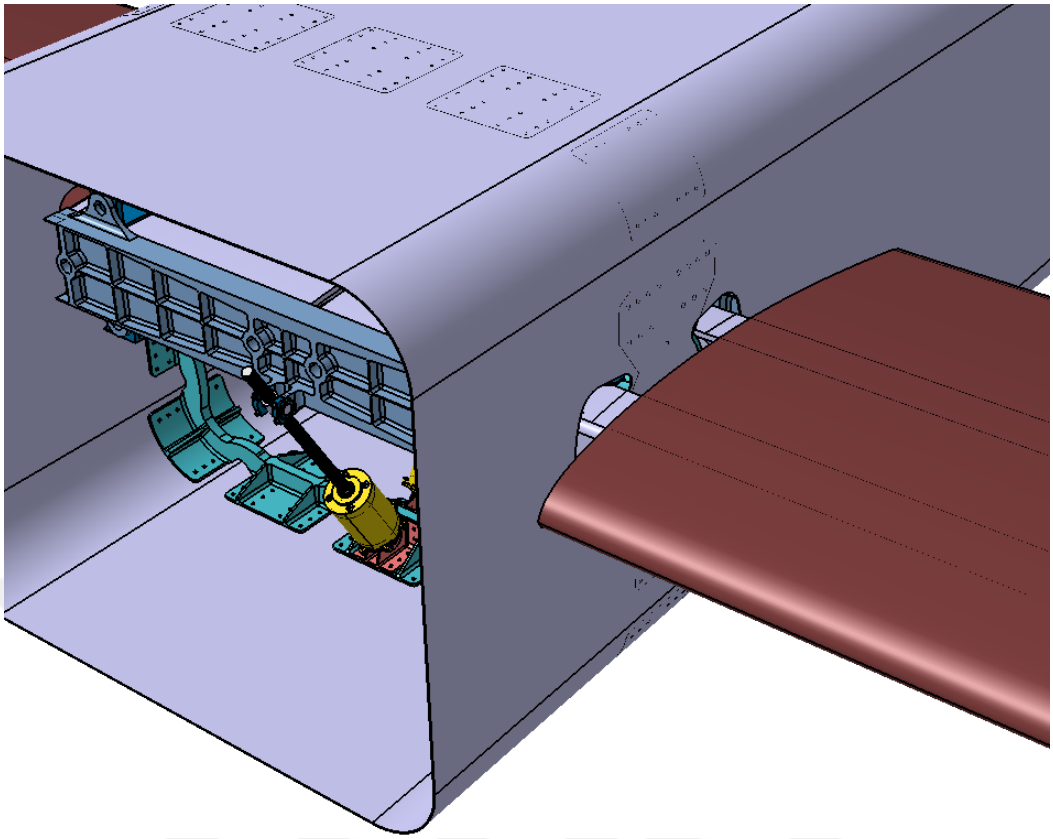

Figure 6.14 Fuselage slots

Although the mechanical design of the mechanism was completed, a serious problem about sealants persisted in the slotted holes, which was the main constraint (Figure 6.14). Because sealing is very important for the smooth operation of such structures, a very special design had to be made for this region. To solve this sealing problem, the sealing mechanism was adapted to the current design. The sealing system was integrated to the current design space, and it was made sure that it did not prevent the movement of the box structure. That is, a new and original sealing system was designed. This novel design was a completely new idea and improved the functionality and life of the product.

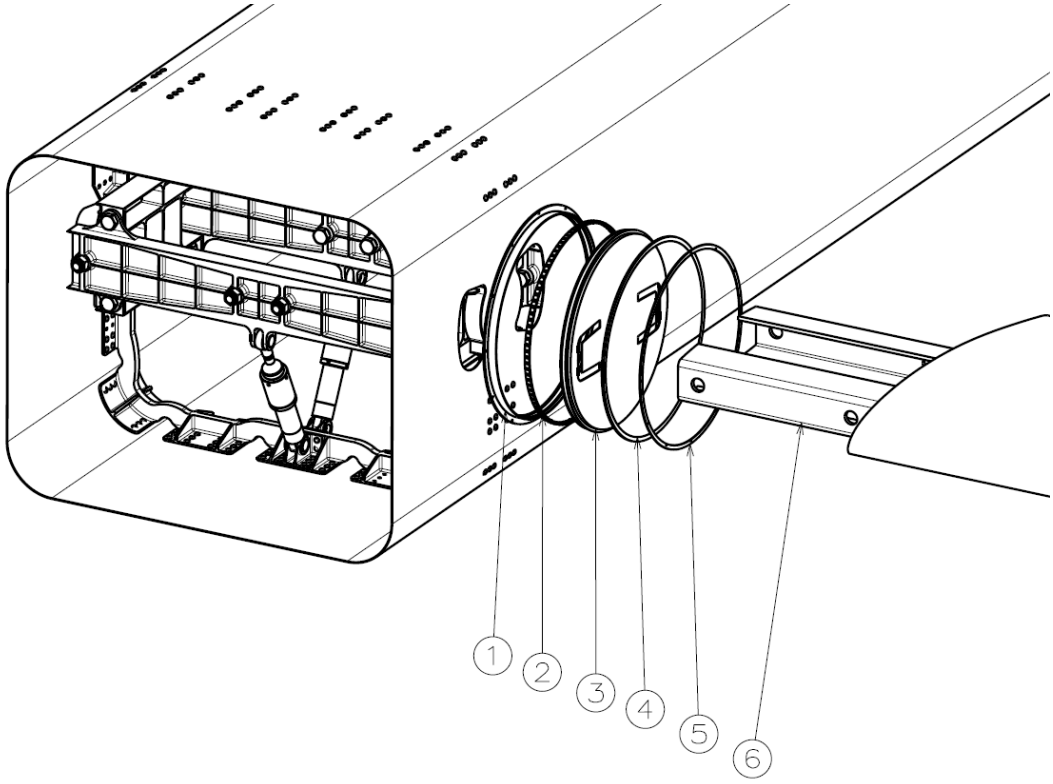

Figure 6.15 Sealing system components

The new sealing system consists of five components for both sides of the fuselage. These components are presented in Figure 6.15, are listed below:

1- Main bearing housing

2- Needle bearing

3- Entrance adaptor

4- Seal

5- Seal cap

6- Wing spar

The function of the main bearing housing was to provide a slot for needle bearing and act as an assemble component for other components. The aim of needle bearing was to allow the entrance adaptor rotation on the main bearing housing. The needle bearing was preferred in this design to other types of bearing, such as deep grow ball bearing

or cylindrical ball bearing, because in this region, far less radial forces acted. Hence, strength bearings were not needed. In this region, it was impossible to use heavy bearings because of weight problems. The entrance adaptor design has a special spar form big enough for both spars to pass through the entrance adaptor. These forms spar shape dependent so that if the shape of spar changes, then the shape of the entrance adaptor form could change accordingly.

The duty of the seal is to prevent the fluid and dust from passing from inside to outside and vice versa. The seal cap works as a stopper and stabilizer for the seal, keeping the seals unchanged mechanically. As to the order of assemble of these components, firstly the main bearing housing was riveted to the fuselage of aircraft, which can be seen in Figure 6.16

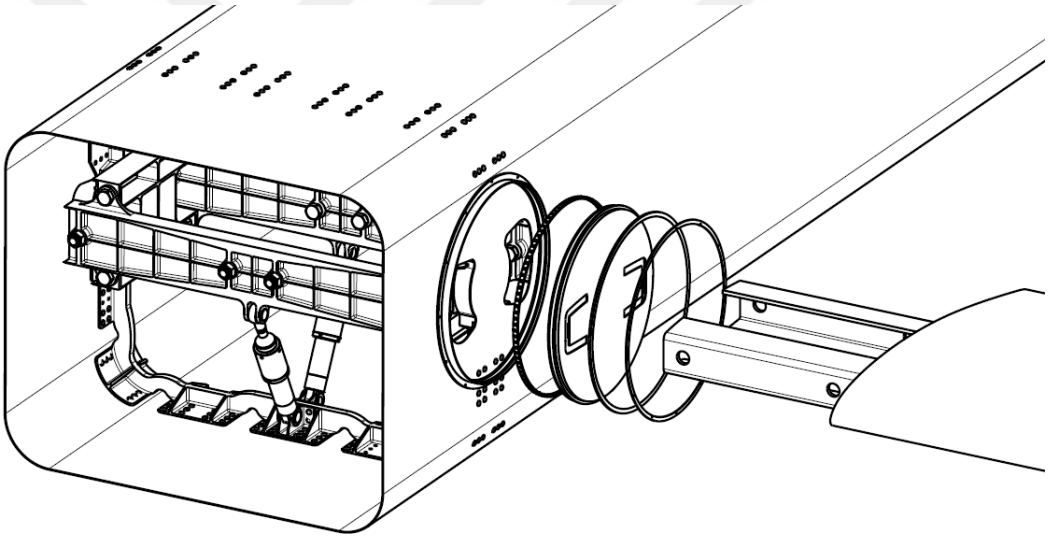

Figure 6.16 Main bearing housing assembly

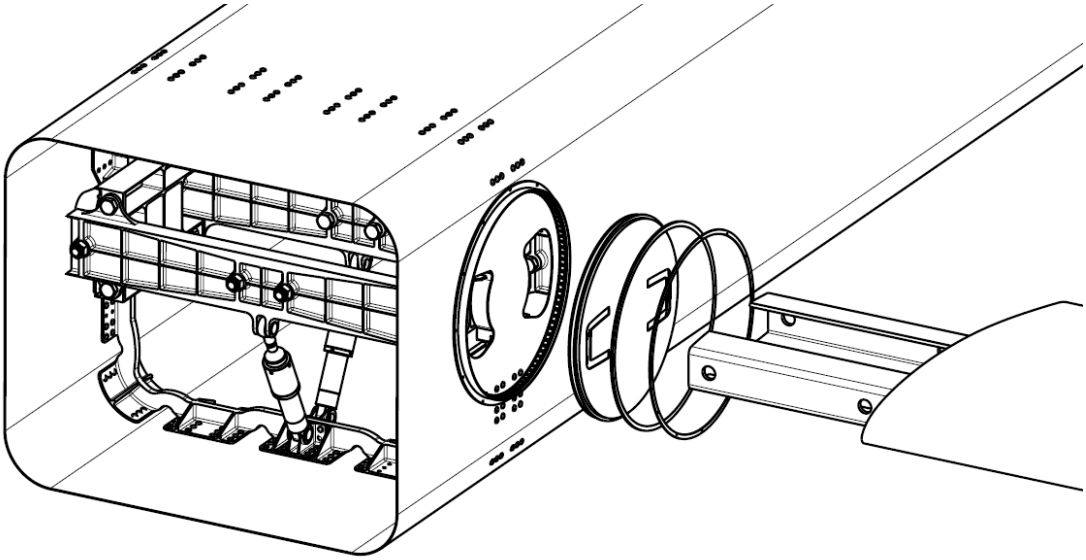

Figure 6.17 Needle bearing assembly stage

Clips were used at both the end and the back of needle bearing assemble stage to mechanically stabilize the position of needle bearing. After a certain diameter, there is no standard for needle bearing production [31] because special production may be necessary as in this case. A special needle bearing design which was short in both length and diameter was preferred to keep weight loss at minimum. The assembly stages for other parts are represented in Figure 6.18 - 20.

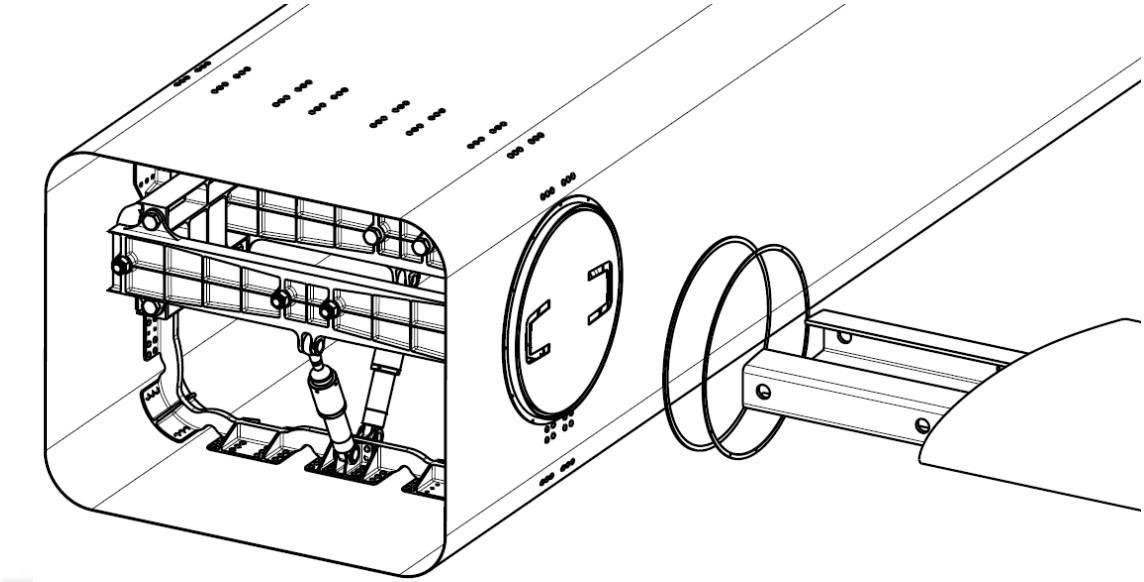

Figure 6.18 Entering adaptor assembly stage

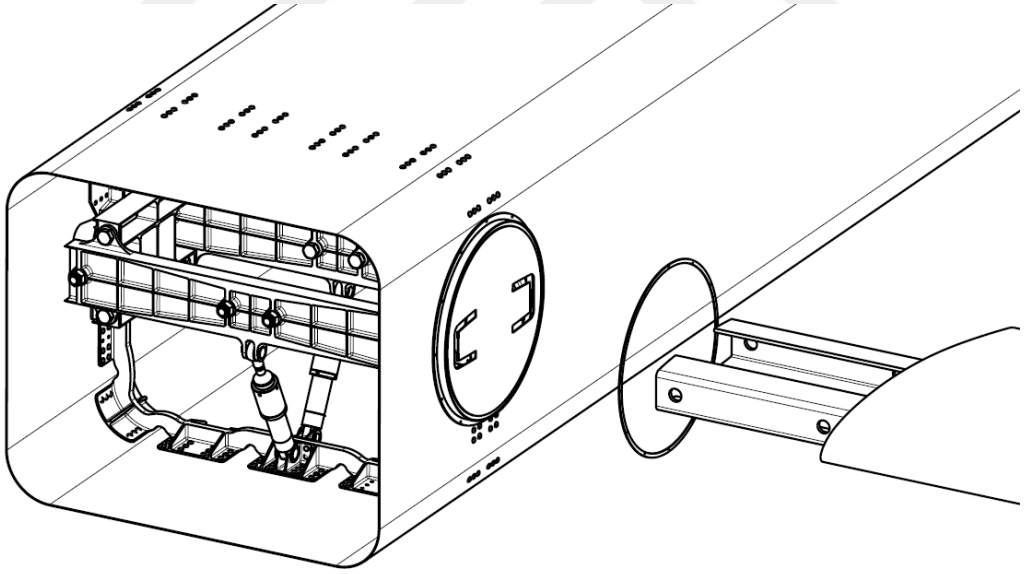

Figure 6.19 Radial shaft seal assembly stage

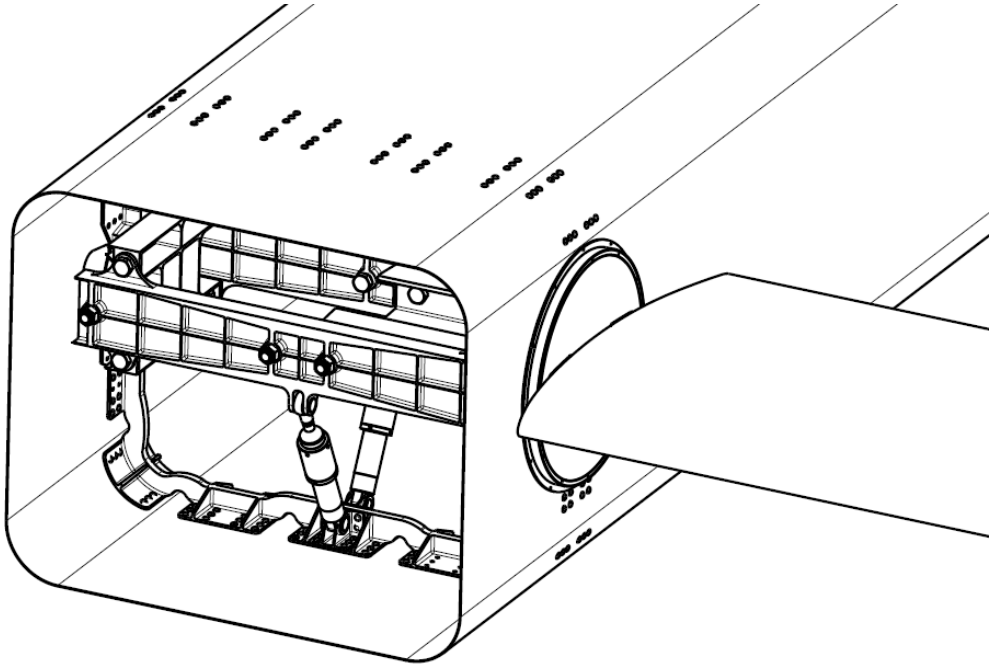

Figure 6.20 Wing assembly stage

An O-ring was assembled to the main bearing housing to enhance the sealing characteristics. After the assembly stages were performed, the sealing problem was solved.

CHAPTER 7

FINITE ELEMENT ANALYSIS

7.1 Finite Element Analysis of Box Structure

This this chapter focuses on a finite element model developed to study the proposed structure. The model was developed and meshed with a quadratic second order triangle elements due to the fact that the higher order elements give better accuracy [32]. Minimum 3 elements are set for radius regions as presented in Figure 7.1

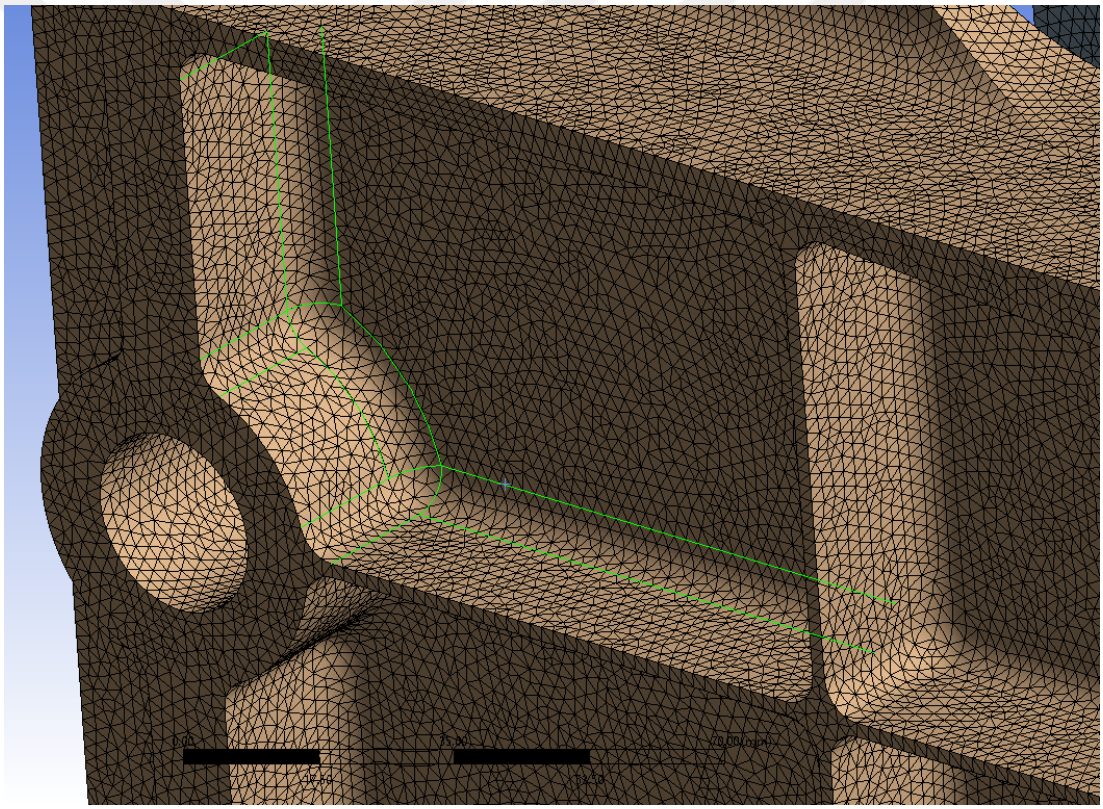

Figure 7.1 Element numbers at radius regions

Total nodes in finite element model was 5508450 while total elements in the model was 3135642.

Body to body revolute joint is implemented in 8 lug regions in the finite element model as showed in 2

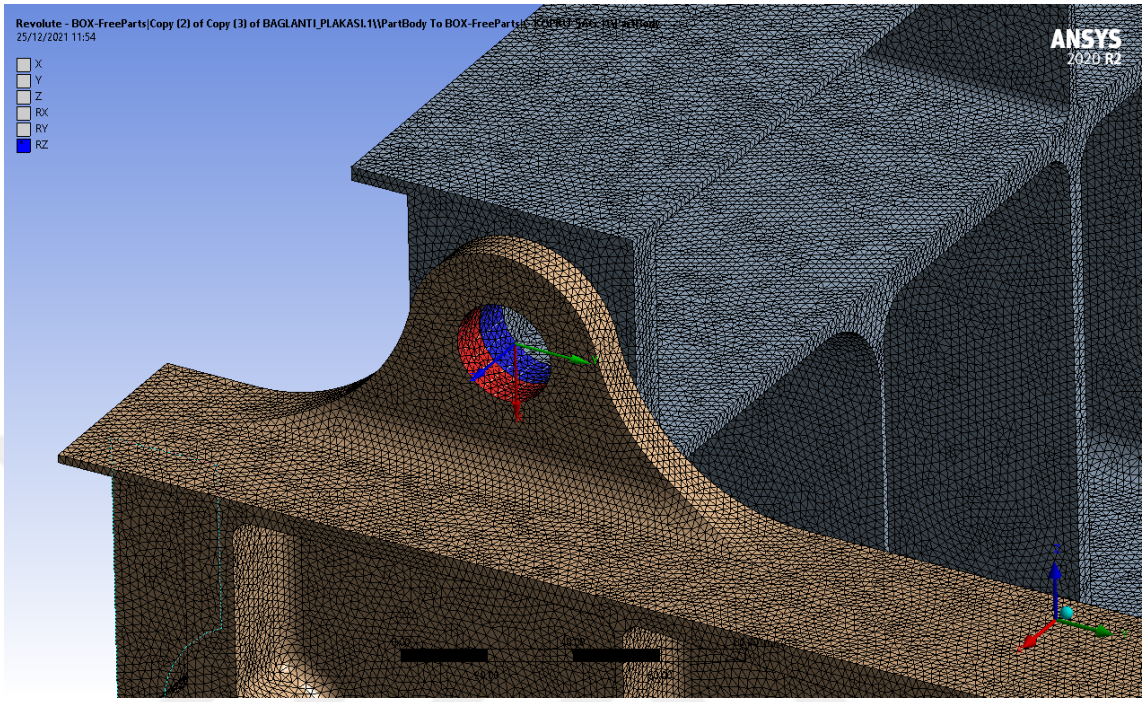

Figure 7.2 Body to body revolute joint

Body to ground fixed joint was implemented in 2 bearing location regions in the finite element model as showed in Figure 7.3

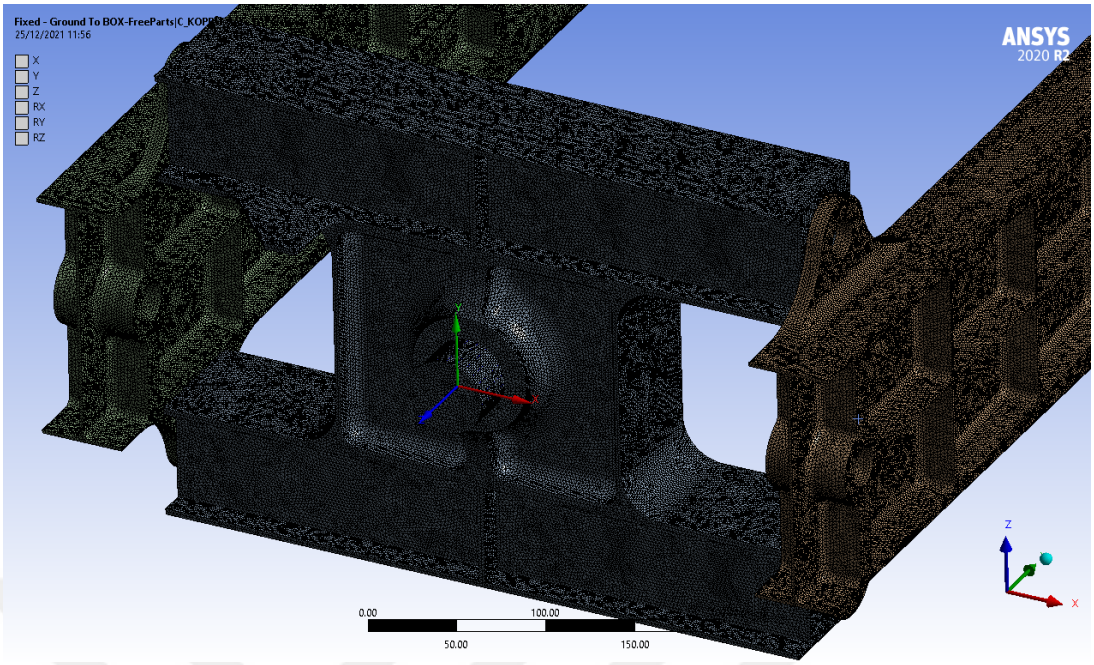

Figure 7.3 Body to ground fixed joint

The general overview of the meshed structure is presented in Figure 7.4

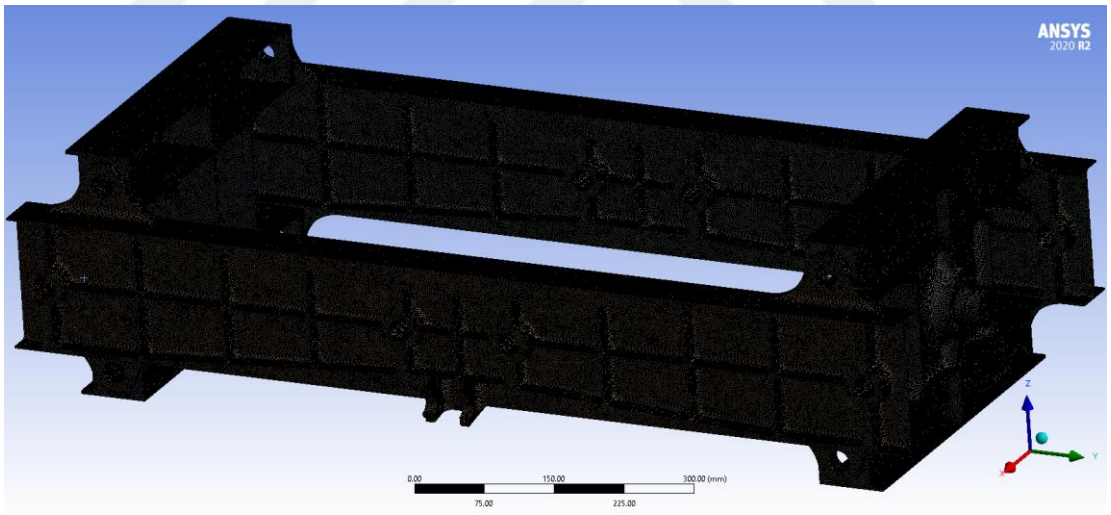

Figure 7.4 Finite element model

As it is seen in Figure 7.5, the model was fixed at bearing connection regions that showed by red triangles. In the proposed model, a 126000 N loads was applied at the outer pins of the model and a -112000 N load was applied to the inner pins of the

beams so the beams were loaded as the four-point bending situation. Basically, this study has exactly simulated the four-point bending case.

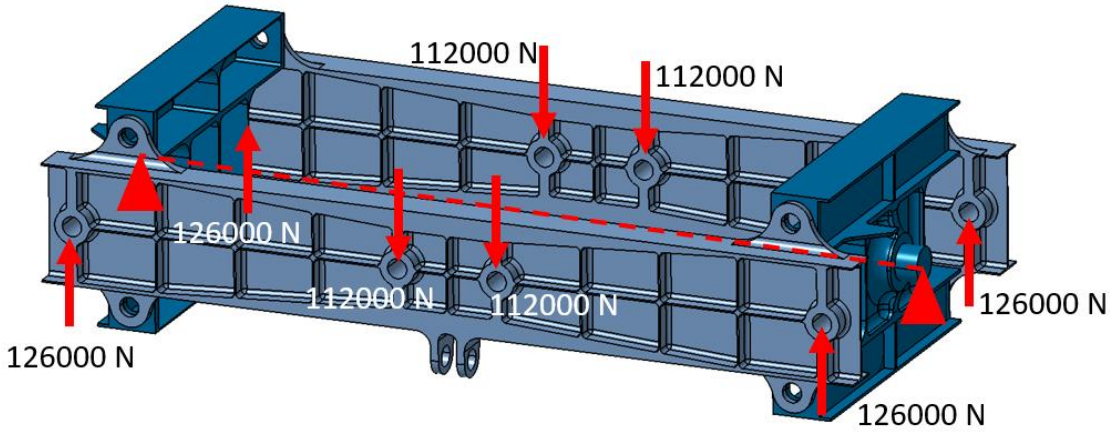

Figure 7.5 Application of boundary conditions

The equivalent von Misses stress results are shown in Figure 7.6 The results demonstrated that the structure was well-designed in terms of stress distribution. Indeed, nearly all the regions carry stress, an indicator of an effective and lightweight design. The selected material was Aluminum 7075 T6. If it were changed to a titanium, the total box structure weight could be reduced by around 50% percent, which can be studies in further research. By using different materials, the most suitable material can be selected. The important thing is that the safety coefficient is sufficient, as well as light.

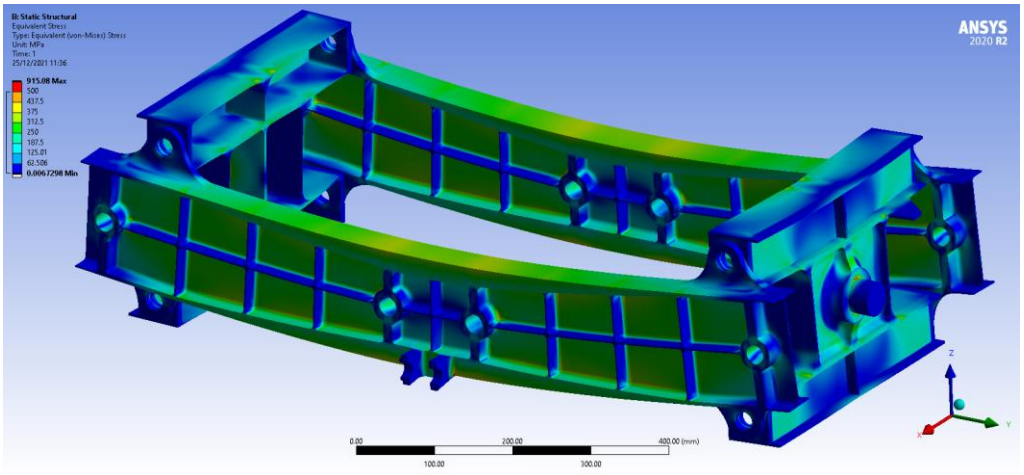

Figure 7.6 von Misses stress contour

The total deformation of the box structure was around 2.36 mm as presented in Figure 7.7.

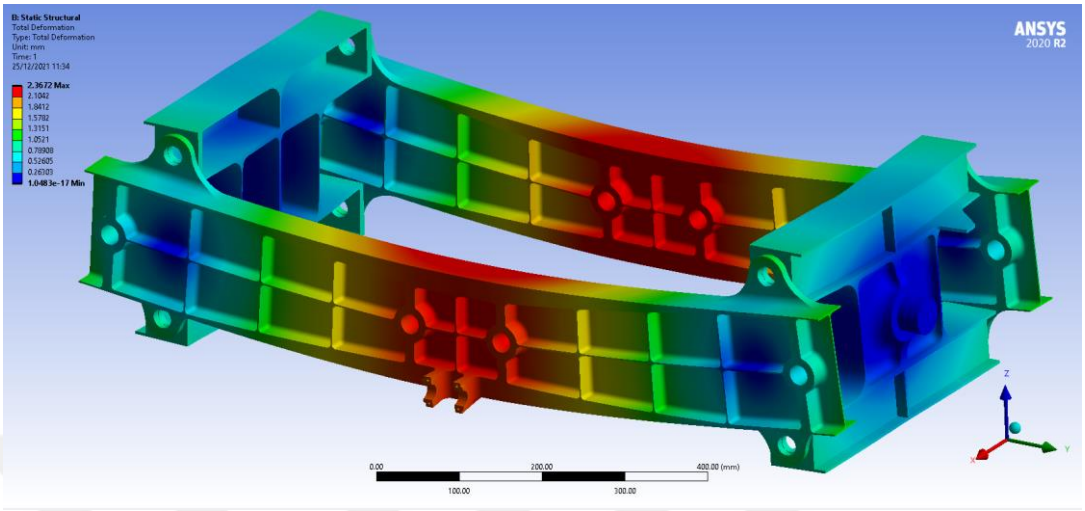

Figure 7.7 Total deformation of box structure

CHAPTER 8

DESIGN OF RUDDERVATOR MECHANISM

8.1 Design of Variable Incidence Ruddervator Mechanism

A variable incidence ruddervator was designed based on a similar idea with the previous designs as shown in Figure 8.1. The main difference between two mechanisms was that the variable incidence wing mechanism has only two main carrier beams while the variable incidence ruddervator mechanism has four main carrier beams. This is so because a 90-degree angle exists between the V tails, so a single main carrier beam cannot be used. The variable incidence mechanism can also be used to trim the aircraft. The same sealing system design was used for the variable incidence ruddervator mechanism. The sealing system design in this study can be applied onto flat surfaces. The wing connection to the fuselage had a flat surface, so there was not any problem with there, but the ruddervator connection surface to the fuselage was not flat, which made it essential to perform the special fairing design.

This way, a flat surface was obtained so that the same sealing system design could be used. The main idea was the same for both structures.

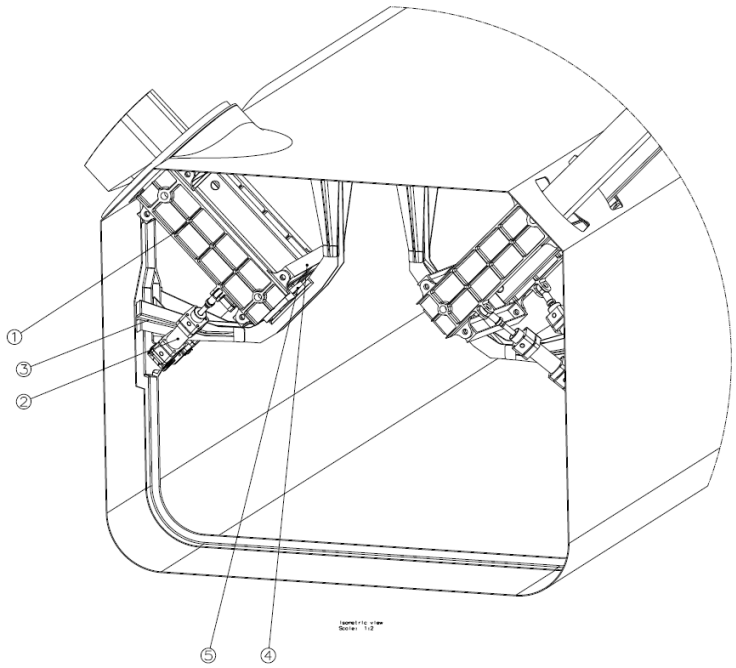

Figure 8.1 Variable incidence ruddervator mechanism

CHAPTER 9

CONCLUSION

This thesis proposed a new approach to UAV's take off and landing from a carrier. It intended to ensure that UAVs can easily take off at a short distance. The new approach or design, which proved applicable in various areas, was tested both numerically and experimentally using the developed mathematical models. The following conclusions were drawn.

- The findings were positive and challenging. The overall goal of short distance takes off and landing were achieved.
- A mathematical model was proposed to prove the concept.

- The mathematical models and flight experiment proved that a 1425 kg UAV can take off without using catapult system at 202 m and a 1200 kg UAV can land at 180 m without using any other external equipment like steel cables.
- A new adjustable system for the wing was designed and patented to adjust the angle of attack.
- A new adjustable ruddervator mechanism system was designed for the wing.
- Three important designs were patented.

REFERENCES

[1] Winter S. R., Rice S., Tamilselvan G. & Russell Tokarski "*Mission-Based Citizen Views on UAV Usage and Privacy: An Affective Perspective*", Journal of Unmanned Vehicle Systems, pp. 6, 05-Feb-2016

[2] Orfanus D., Pignaton E. F. & Eliassen F. "*Self-Organization as a Supporting Paradigm for Military UAV Relay Networks*", Vol.20, pp. 1, April 2016

[3] M. Hassanalian, A. Abdelkefi "*Classifications, applications, and design challenges of drones: A review*", Vol.91, pp. 1, May 2017

[4] Horowitz M. C., Kreps S. E.& Fuhrmann M. "*Separating Fact from Fiction in the Debate over Drone Proliferation*", Vol.41, pp. 15, Fall 2016

[5] Mahadevan, Prem "*The Military Utility of Drones*", No. 78, pp. 1, July 2010

[6] Biddle T. D., "*Unmanned Aerial Vehicles – Revolutionary Tools in War and Peace*", pp. 5, March 2007

[7] Shashidhara B.P., R. Chandrasekaran, Bhatia Y., G. Magesh, Bineshkumar K. & Hemanth K. V. "*Development of a Full Mission Simulator for Pilot Training of Fighter Aircraft*", Vol.68, No.5, pp. 426, September 2018

[8] Johnson C. L., "*Development of the Lockheed P-80A Jet Fighter Airplane*", Vol.14, No.12, pp. 678, December 1947

[9] Yang Z., Sheng h., Bin C. & Wen W., "*Adaptive constrained backstepping controller with prescribed performance methodology for carrier-based UAV*", Vol.92, pp. 55, September 2019

[10] Azeem S., "*Autonomous Unmanned Aerial Vehicles*", pp.12, 2/29/2012

[11] James D. P., "*Navy Unmanned Air Systems, 1915 – 2011*", pp.17, 21 - 22 September 2011, Virginia Beach, VA

[12] Erdinçler E. R., "*Current Security Policies in Turkey on the Perspective of Defence Industry Technologies: A Reactivity-Proactivity Analysis*", pp.12, Güvenlik Bilimleri Dergisi, Nisan 2019

[13] Aksan S., "*SİHA yüklü TCG Anadolu: Dönüşümün kilometre taşı",* 18 May 2021,https://www.trthaber.com/haber/gundem/siha-yuklu-tcg-anadolu-donusumun-kilometre-tasi-581457.html. 2021

[14] Seyhan Ö., *Türk Loydu "Donanmanın Gururu TCG Anadolu'yu Türk Loydu Klaslıyor"*, 18 Mar 2018, https://www.turkloydu.org/tr-tr/yayinlar/makaleler/donanmanin-gururu-tcg-anadolu-yu-turk-loydu-klasli.aspx. 2018

[15] Multhopp H., "*Methods Calculating the Lift Distribution of Wings*", pp.3, 1955

[16] Anderson J. D., "*Fundamentals of Aerodynamics*", pp.32, Sixth Edition

[17] Anderson J. D., "*Fundamentals of Aerodynamics*", pp.365, Sixth Edition

[18] Houghton E. L. & Carpenter P. W. "*Aerodynamics for Engineering Students*", pp.28, Fifth Edition

[19] Patent application of variable incidence wing system. Retreived from https://worldwide.espacenet.com/patent/search/family/001485019/publication/FR444010A?q=pn%3DFR444010

[20] United States Naval Institute Proceedings, pp. 136, January 1965

[21] Rodgers E. J., "*The Neutral Point in Stability and Control Analysis*", Vol.2, No.1, pp.1, Jan-Feb,1995s

[22] Rajamani R., Damrongrit N., Piyabong K., Jae Y. L., Kyongsu Y., and Gridsada P., "*Tire-Road Friction-Coefficient Estimation*", pp.54, IEEE Control Systems Magazine, August 2010

[23] Kordani A. A., Rahmani O., Saman A., Nasiri A., Boroomandrad S. M., "*Effect of Adverse Weather Conditions on Vehicle Braking Distance of Highways*" Vol. 4, No. 1, pp.50, January, 2018

[24] Leishman J. G., "*Aerodynamic Characteristics of a Helicopter Rotor Airfoil as affected by Simulated Ballistic Damage*" Army Research Labrotory, September 1993

[25] Viieru D., Lian Y., Shyy W., and Ifju P., "*Investigation of Tip Vortex on Aerodynamic Performance of a Micro Air Vehicle*", pp.7,33rd AIAA Fluid Dynamics Conference and Exhibit, 23-26 June 2003, Orlando, Florida

[26] Phillips W. F. and Hunsaker D. F., "*Estimating the Subsonic Aerodynamic Center and Moment Components for Swept Wings*", pp.1034, JOURNAL OF AIRCRAFT, Vol. 45, No. 3, May–June 2008

[27] Ugural A. C., Fenster S. K., "*Advanced Mechanics of Materials and Applied Elasticity*", pp.258, Fifth Edition

[28] Gherardi P. R., Brancheriau L., "*Comparison Between Three-Point and Four – Point Flexural Tests to Determine Wood Strength of Eucalyptus Specimens*", pp.338

[29] Ugural A. C. & Fenster S. K., "*Advanced Mechanics of Materials and Applied Elasticity*", pp.228, Fifth Edition

[30] Budynas R. G. and Nisbett J. K., "*Sigley's Mechanical Engineering Design*", pp.95, Ninth Edition

[31] SKF needle roller and cage assemblies. Retreived from https://www.skf.com/group/products/rolling-bearings/roller-bearings/needle-roller-bearings/needle-roller-and-cage-assemblies

[32] Z.C. He, G.R. Liu, Z.H. Zhong, S.C. Wub,d, G.Y. Zhang & A.G. Cheng, "*An edge-based smoothed finite element method (ES-FEM) for analyzing three-dimensional acoustic problems*", pp.20, 10 September 2009

[33] Rodgers E. J., "*The Neutral Point in Stability and Control Analysis*" Vol. 2, No. 1, pp.34, Jan - Feb, 1965

CURRICULUM VITAE

PERSONAL INFORMATION

Name Surname **:** Mustafa MURAT

EDUCATION

High School **:** Gebze Anatolian High School

Bachelor **:** Istanbul Technical University

Master Degree **:** Ankara Yıldırım Beyazıt University

WORK EXPERIENCE

Mechanical Design & Structural Analysis Engineer

Baykar Makina Inc., İtanbul.

Structural Analysis Engineer

Turkish Aerospace Industries, Inc., Ankara, Turkey.

TOPICS OF INTEREST

- Space Structures Design (Mechanical & Aeromechanical)
- Machine Design
- Structural Analysis
- Design Optimization

PUBLICATIONS

Igor Zhilyaev, Nitesh Anerao, Ajay Giri Prakash Kottapalli, Mahmut Cihat Yilmaz, **Mustafa Murat**, Mostafa Ranjbar and Anastasiia Krushynska, Fully-printed metamaterial-type flexible wings with controllable flight characteristics, Bioinspiration & Biomimetics, 17 (2), 1-15, 2022.

PATENTS

2021 “A fixed wing control mechanism”, Turkish Patent Institute (TPI), Application Number: 2021/015233 (with Fahrettin Öztürk)

2021 “A wing system”, Turkish Patent Institute (TPI), Application Number: 2021/015231 (with Fahrettin Öztürk)

2021 “A v-tail drivetrain”, Turkish Patent Institute (TPI), Application Number: 2021/015227 (with Fahrettin Öztürk)


YILDIRIM BEYAZIT
UNIVERSITY